



**Model aircraft dynamics determination and control  
system design through analysis of experimental data**

**Miguel Ángel Sobrino Pozuelo**

Thesis to obtain the Master Science Degree in:

**Aerospace Engineering**

Supervisors: Dr. Francisco Fernandes Castro Rego

Prof. Frederico José Prata Rente Reis Afonso

**Examination Committee**

Chairperson: Prof. José Fernando Alves da Silva

Supervisor: Dr. Francisco Fernandes Castro Rego

Member of the committee: Prof. Rita Maria Mendes de Almeida Correia da  
Cunha

**October, 2022**

## Acknowledgments

I would like to thank my parents and sister for have been supporting me during these hard years at university. Also, I want to thank my university friends but especially Alex and Alberto for being there since the beginning of this journey, and always willing to help. Special acknowledgments to Laia for always encouraging me in difficult moments. I would also like to thank and congratulate Instituto Superior Técnico and my thesis supervisors Dr. Francisco Fernandes Castro Rego, Prof. Frederico Afonso, and Prof. Fernando Lau for offering a great Erasmus experience full of knowledge and entertainment.

## Abstract

The commercial and military interest in Unmanned Aerial Vehicles is continuously increasing. In addition, small Unmanned Aerial Vehicles (UAVs) are a good option to evaluate the advantages of certain novel aircraft configurations. There is a particular interest in the aerospace industry, to develop commercial applications for flying wings type of aircraft. There is also interest in the UAV industry to design and optimize these kinds of tail-less aircraft for certain missions to achieve better results.

This study describes the history of flying wings type of aircraft and highlights their advantages and drawbacks from the point of view of aerodynamics and flight dynamics.

After the research part, a flying wing prototype, called CP50-V0 was built in the aerospace laboratory available at Instituto Superior Técnico. The prototype was built together with Alejandro Álvarez, author of the work [1]. The prototype's wingspan is 950mm, to fit inside the wind tunnel. It is built on foam with the materials available at the laboratory.

The prototype is tested in the aerospace laboratory's wind tunnel, with the purpose of comparing the results of the aerodynamic simulations with the experimental data. The wind tunnel tests are designed to be low-cost. All the items required for the experiments such as stands, load cells, sensors, etc., are provided by Técnico, manufactured, or bought. Two types of experiments are conducted: static experiments, to obtain Lift and Drag curves, and dynamic experiments, to determine the stability properties of the prototype.

Once the experimental data is processed and analyzed, the results are compared with the simulations done with the software *XFLR5*. Finally, a flight dynamics model is implemented in *MATLAB* with the final purpose of designing a control system in *SIMULINK*.

**Keywords:** Unmanned Aerial Vehicle, Flying Wing, Manufacturing, Prototyping, Wind tunnel, *XFLR5*, Stability, Control, Autopilot, *MATLAB*, *SIMULINK*.

## Resumo

O interesse comercial e militar em veículos aéreos não tripulados está continuamente a aumentar, bem como a investigação nestes tipos de aeronaves. Há também um interesse particular na indústria aeroespacial, para desenvolver aplicações comerciais de aeronaves do tipo asas voadoras.

Este estudo descreve a história das asas voadoras e destaca as suas vantagens e inconvenientes do ponto de vista da aerodinâmica e da dinâmica de voo.

Após a investigação, foi construído um protótipo, chamado CP50-V0, no laboratório de engenharia aeroespacial do Instituto Superior Técnico. O protótipo foi construído em conjunto com Alejandro Álvarez, autor da obra [1]. O protótipo tem 950mm de envergadura para caber no interior do túnel de vento. É construído em espuma com os materiais disponíveis no laboratório.

O protótipo foi testado no túnel de vento do laboratório aeroespacial, com o objectivo de comparar os resultados das simulações aerodinâmicas com os dados experimentais. Os testes em túnel de vento são concebidos para ser de baixo custo. Todos os itens necessários para as experiências, tais como: suportes, células de carga, sensores, etc., são fornecidos pelo Técnico, fabricados, ou comprados. São realizados dois tipos de experiências: as experiências estáticas, para obter curvas de sustentação e resistência aerodinâmica, e também as experiências dinâmicas, para determinar as propriedades de estabilidade do protótipo.

Uma vez processados e analisados os dados experimentais, os resultados são comparados com as simulações feitas com o software *XFLR5*. Finalmente, um modelo de dinâmica de voo é implementado em *MATLAB* com o objectivo final de conceber um sistema de controlo em *SIMULINK*.

**Palavras-chave:** Veículo Aéreo Não Tripulado, Asa Voadora, Fabrico, Prototipagem, Túnel de Vento, *XFLR5*, Estabilidade, Controlo, Piloto Automático, *MATLAB*, *SIMULINK*.

# Index

<b>Acknowledgments</b>	<b>i</b>
<b>Abstract</b>	<b>ii</b>
<b>Resumo</b>	<b>iii</b>
<b>List of Tables</b>	<b>vii</b>
<b>List of Figures</b>	<b>viii</b>
<b>Glossary</b>	<b>xi</b>
<b>Nomenclature</b>	<b>xi</b>
<b>1 Introduction</b>	<b>1</b>
1.1 Motivation and objectives . . . . .	1
1.2 Project's timeline . . . . .	1
1.3 Thesis outline . . . . .	2
<b>2 Research and State of Art</b>	<b>3</b>
2.1 The development of the flying wing . . . . .	3
2.2 Aerodynamics and flight dynamics of flying wings . . . . .	7
2.2.1 Airfoil and wing design . . . . .	7
2.2.2 Achieve positive $Cm_0$ . . . . .	8
2.3 Flight dynamics . . . . .	9
2.4 Introduction to flight control . . . . .	10
2.4.1 Level of autonomy and control system layers . . . . .	11
2.4.2 The classical control theory . . . . .	11
2.4.3 Linear an non-linear control theories . . . . .	13
2.4.4 Important concepts in control theory . . . . .	13
2.4.5 State observation and Kalman filters . . . . .	15
<b>3 Flying wing prototype and flight dynamics model</b>	<b>17</b>
3.1 Election of the prototype . . . . .	17
3.2 Aerodynamic study . . . . .	18
3.3 Equations for aircraft modelling . . . . .	21
3.4 Equations, implementation & testing . . . . .	28
3.5 Modal analysis and modifications impact . . . . .	30
3.6 Flight qualities of CP50-V0 . . . . .	31

3.7	Spiral mode improvement . . . . .	32
<b>4</b>	<b>Prototype manufacturing</b>	<b>33</b>
4.1	Components . . . . .	33
4.2	Manufacturing process . . . . .	33
4.3	Center of gravity estimation . . . . .	35
4.4	Inertia moment estimation . . . . .	37
<b>5</b>	<b>Wind tunnel experiments</b>	<b>39</b>
5.1	Static experiment description . . . . .	39
5.2	Static experiment implementation . . . . .	39
5.3	Static experiment results . . . . .	42
5.4	Stability derivatives estimation . . . . .	45
5.5	Flight dynamic equations (Control Oriented) . . . . .	47
5.6	Stability derivatives estimation - Wind tunnel . . . . .	48
5.7	Dynamic experiments description . . . . .	48
5.8	Dynamic experiments implementation . . . . .	50
5.9	Dynamic experiment results . . . . .	51
5.9.1	Lateral experiments . . . . .	51
5.9.2	Longitudinal experiments . . . . .	53
5.10	Additional data . . . . .	54
5.11	Conclusions, improvement and future work . . . . .	55
<b>6</b>	<b>Simulink model</b>	<b>57</b>
6.1	Simulink model description . . . . .	57
6.2	Simulink model linearization and validation . . . . .	60
<b>7</b>	<b>Flight control</b>	<b>62</b>
7.1	Lateral autopilot . . . . .	62
7.1.1	Inner loop design . . . . .	64
7.1.2	Outer loop design . . . . .	68
7.2	Longitudinal autopilot . . . . .	71
7.2.1	Altitude hold controller . . . . .	75
7.2.2	Airspeed hold controller . . . . .	78
<b>8</b>	<b>Conclusions</b>	<b>80</b>
	<b>Appendices</b>	<b>81</b>
<b>A</b>	<b>Wind tunnel test equipment</b>	<b>81</b>



## List of Tables

1	Airfoil details . . . . .	18
2	Wing properties . . . . .	18
3	XFRL5 panel distribution . . . . .	20
4	Comparison of Longitudinal Modes . . . . .	28
5	Comparison of Lateral Modes . . . . .	28
6	Dynamic modes comparison with other works . . . . .	30
7	Dynamic modes comparison . . . . .	30
8	Modal properties CP50-V0 (winglets) . . . . .	31
9	Dynamic modes comparison . . . . .	32
10	Center of gravity test results . . . . .	36
11	Mass component properties . . . . .	38
12	<i>CATIA</i> estimation . . . . .	38
13	Wind tunnel setup relations. . . . .	40
14	Lift slope estimation. . . . .	43
15	Approximated arm distances. . . . .	45
16	Response analysis to yaw perturbations $V = 7m/s$ . . . . .	53
17	Response analysis to yaw perturbations $V = 8m/s$ . . . . .	53
18	Response analysis to yaw perturbations $V = 9m/s$ . . . . .	53
19	Trim conditions. . . . .	54
20	Trim flight experiment envelope. . . . .	55
21	Test cell limits. . . . .	55
22	Constraints to states . . . . .	61
23	Constraints to inputs . . . . .	61
24	Trim condition . . . . .	61
25	Comparison of Longitudinal Modes . . . . .	61
26	Comparison of Lateral Modes . . . . .	61
27	Selected gains $\phi$ loop . . . . .	68
28	Selected gains $\chi$ loop. . . . .	69
29	Saturation constraints. . . . .	72
30	Selected gains $\theta$ loop for pitch hold mode. . . . .	74
31	Selected gains h loop . . . . .	77
32	Selected gains airspeed loop. . . . .	79
33	Model parameter . . . . .	83
34	<i>SIMULINK</i> model trim point . . . . .	83
35	Stability derivative values . . . . .	84



## List of Figures

1	Project's timeline . . . . .	2
2	Northrop No. 1. Source: Skytamer . . . . .	3
3	Horten's all-wing gliders Source: Fiddlersgreen . . . . .	4
4	Northrop N-1M aircraft Source: aire.org . . . . .	4
5	Horten Ho XI V-2, Source: warbirds . . . . .	5
6	Mel63, Source: mourningtheancient . . . . .	5
7	Northrop XB-35, Source: theaviationclub] . . . . .	6
8	Northrop YB-49, Source: avionslegendaires . . . . .	6
9	Northrop B-2 Stealth bomber Source: militarymachine . . . . .	6
10	Span-wise lift and weight distributions Source: Researchgate . . . . .	7
11	Pitch moment vs alpha (Longitudinal stability), Source: engineeringpilot . .	8
12	Ways to achieve $C_{m_0}$ Source:[4] . . . . .	9
13	Northrop B-2 Split-Ailerons Source: Quora . . . . .	10
14	List of autonomy levels (AL) with descriptions. Source: researchgate . . . .	11
15	closed-loop feedback (Block Diagram representation). Source: wikipedia . .	12
16	Closed-loop block diagram, Source: wikipedia . . . . .	12
17	Closed-loop math expressions Source: wikipedia . . . . .	12
18	PID controller Source: wikipedia . . . . .	13
19	System behaviour, Source: controlsystemengineer . . . . .	14
20	State estimator block diagram Source:[8] . . . . .	15
21	Zyklon planes (measures in millimeters), Source:[10]. . . . .	17
22	Eppler 186 airfoil Source:link. . . . .	18
23	Prototype geometry (side view). . . . .	18
24	Prototype panel distribution in <i>XFRL5</i> . . . . .	19
25	$C_L(\alpha)$ and $C_D(\alpha)$ curves for various airspeed (final version). . . . .	20
26	Efficiency and $C_m(\alpha)$ curves for various airspeed (final version). . . . .	21
27	Notation Source:[17]. . . . .	23
28	Control surfaces. . . . .	25
29	Reference magnitudes, Source:[17] . . . . .	26
30	Adimensional coefficients, Source:[17] . . . . .	26
31	Stability axis . . . . .	27
32	Reference magnitudes, Source:[17] . . . . .	27
33	Adimensional coefficients, Source:[17] . . . . .	27
34	Prototype simulated in <i>XFRL5</i> . . . . .	29
35	Longitudinal response comparison for $\Delta u = 0.5(m/s)$ perturbation . . . .	29
36	Lateral-directional response comparison for $\Delta v = 0.1(m/s)$ perturbation . .	29

37	CP50-V0 . . . . .	30
38	[4] . . . . .	30
39	[11] . . . . .	30
40	CP50-V0 without winglets. . . . .	30
41	CP50-V0 with winglets. . . . .	30
42	Scrap piece used to test . . . . .	34
43	First attempt . . . . .	34
44	Detail of electronics bay . . . . .	34
45	Completed prototype . . . . .	34
46	Test cell assembly . . . . .	35
47	Prototype over the test cell . . . . .	35
48	Center of gravity test distances . . . . .	36
49	Inertia test assembly . . . . .	37
50	Model placed for testing . . . . .	37
51	CP50-V0 prototype modeled in <i>CATIA</i> . . . . .	38
52	Test cell with the direction of force (lift in red and drag in blue) and torque (green) measures. . . . .	39
53	Wind tunnel static experiments force diagram. . . . .	40
54	Assembly parts and servo . . . . .	41
55	3D printed parts . . . . .	41
56	Static experiment configuration. . . . .	41
57	Model ready to be tested. . . . .	41
58	Experimental data and <i>XFLR5</i> estimations. . . . .	42
59	Experimental data and <i>XFLR5</i> estimations. . . . .	44
60	$M_{ac}$ estimation. . . . .	45
61	Longitudinal wind tunnel experiment source:[17]. . . . .	49
62	Lateral-directional experiment source:[17]. . . . .	49
63	Parts used for the dynamic experiments. . . . .	50
64	Prototype mounted. . . . .	50
65	Mounting plate to fit the bearing. . . . .	50
66	Prototype mounted. . . . .	50
67	IMU mounted under the prototype. . . . .	51
68	Response to yaw perturbation $V = 7$ m/s. . . . .	51
69	Response to yaw perturbation $V = 8$ m/s. . . . .	52
70	Exponential behavior in pitch angle. . . . .	54
71	Simulink block structure. . . . .	60
72	Lateral controller architecture. Source:[16]. . . . .	62

73	Simulink implementation. . . . .	63
74	Simulink structure. . . . .	63
75	Controller block. . . . .	64
76	$\phi$ step response for different $k_p$ values. . . . .	66
77	$\phi$ frequency response for different $k_p$ values. . . . .	66
78	$\phi$ step response for different $k_i$ values . . . . .	67
79	Root locus for various $k_i$ values ( $k_p = 0.5, k_d = 0.03$ ) . . . . .	67
80	Step response (final gains) ( <i>SIMULINK</i> ) . . . . .	68
81	Outer loop simplification Source:[16]. . . . .	69
82	Step response (final gains) ( <i>SIMULINK</i> ). . . . .	69
83	2D position of the UAV during course change maneuvers. . . . .	70
84	3D position of the UAV during course change maneuvers. . . . .	70
85	Longitudinal controller's modes. . . . .	71
86	$k_p$ influence on static gain . . . . .	72
87	$K_p$ influence on frequency response. . . . .	73
88	$k_d$ influence. . . . .	73
89	Pitch response with final design gains ( <i>SIMULINK</i> ). . . . .	74
90	Pitch hold controller <i>SIMULINK</i> implementation. . . . .	74
91	Altitude hold controller <i>SIMULINK</i> implementation. . . . .	75
92	outer loop for altitude control (inner loop dynamics simplified) [16]. . . . .	76
93	Step response for different $K_p$ gains. . . . .	76
94	Step response for different $k_i$ gains. . . . .	77
95	Final step response in altitude. . . . .	78
96	Airspeed hold controller <i>SIMULINK</i> implementation. . . . .	79
97	Final step response increasing airspeed . . . . .	79
98	Final step response decreasing airspeed . . . . .	79
99	Tyto Robotics Series 1580 Test stand, Source: Tyto Robotics. . . . .	81
100	RCbenchmark software Source:Tyto Robotics. . . . .	81
101	IMU back face Source:link. . . . .	82
102	IMU front face Source:link. . . . .	82
103	<i>RaspberryPi</i> connections IC2 port. . . . .	82
104	IMU connections. . . . .	82
105	Prototype drag polar . . . . .	85

## Glossary

**Ai** Artificial Intelligence.

**AoA** Angle Of Attack.

**BIBO** Bounded Input Bounded Output.

**BWB** Blended Wing Body.

**COG** Center Of Gravity.

**DE** Differential equation.

**EKF** Extended Kalman Filter.

**FW** Flying Wing.

**FWB** Flight By Wire.

**IMU** Inertial Measurement Unit.

**ISS** Input to State Stability.

**LTI** Linear Time Invariant.

**MIMO** Multiple Input Multiple Output.

**MTOW** Maximum Take Off Weight.

**PD** Proportional Derivative.

**PID** Proportional Integrative Derivative.

**SISO** Single Input Single Output.

**SLC** Successive Loop Closure.

**TF** Transfer Function.

**UAV** Unmanned Aerial Vehicle.

**WWI** World War I.

## Nomenclature

$\alpha$	Angle of attack
$\beta$	Angle of side-slip
$\Delta p, \Delta q, \Delta r$	Incremental angular velocities
$\Delta\alpha, \Delta\beta$	Incremental angle of attack and side-slip angle
$\Delta\phi, \Delta\theta, \Delta\psi$	Incremental Euler angles
$\delta_a$	Aileron input
$\delta_e$	Elevator input
$\delta_r$	Rudder input
$\delta_t$	Throttle input
$\Gamma$	Wing Dihedral angle
$\gamma_s$	Flight path angle (reference state)
$\hat{I}_y$	Adimensional Inertia momentum in Y body direction
$\hat{I}_z$	Adimensional Inertia momentum in Z body direction
$\hat{I}_x$	Adimensional Inertia momentum in X body direction
$\hat{J}_{xz}$	Adimensional Off-diagonal inertia momentum
$\wedge$	Dimensionless label
$\Lambda$	Wing Sweep angle
$\lambda$	Wing Taper ratio
$\omega_n$	Calculated natural frequency (rad/s)
$\bar{c}$	Mean aerodynamic chord
$\phi, \theta, \psi$	Euler angles
$\phi$	Roll Angle
$\psi$	Yaw angle
$\rho$	Density

$\sigma_u$	Turbulent intensity parameter for X body direction
$\sigma_v$	Turbulent intensity parameter for Y body direction
$\sigma_w$	Turbulent intensity parameter for Z body direction
$\theta$	Pitch angle
$\xi$	Damping ratio
$\xi$	Damping
$AR$	Aspect Ratio
$b$	Wingspan
$c$	Wing Central chord
$C_{ab}$	Force coefficient (a) derivative with respect to (b)
$C_{D\delta_e}$	Drag coefficient variation with respect to $\delta_e$
$C_{D_0}$	Drag coefficient for zero $\alpha$
$C_{Dq}$	Dreag coefficient variation with respect to q
$C_D$	Drag coefficient
$C_{L\alpha}$	Lift coefficient variation with $\alpha$
$C_{l\beta}$	Roll coefficient variation with respect to $\beta$
$C_{l\delta_a}$	Bank moment coefficient variation with respect to adimensional $\delta_a$
$C_{L\delta_e}$	Lift coefficient variation with respect to $\delta_e$
$C_{l\hat{\alpha}}$	Bank moment coefficient variation with respect to adimensional derivative of $\delta_a$
$C_{l\hat{r}}$	Bank moment coefficient variation with respect to $\delta_r$
$C_{lp}$	Bank moment coefficient variation with respect to adimensional p
$C_{l\hat{p}}$	Roll coefficient variation with respect to adimensional roll rate
$C_{l\hat{r}}$	Bank moment coefficient variation with respect to adimensional r
$C_{L_0}$	Lift coefficient for zero $\alpha$
$C_{L_{max}}$	Maximum Lift coefficient

$C_{Lq}$	Lift coefficient variation with respect to $q$
$C_L$	Lift coefficient
$C_{m\alpha}$	Pitch coefficient variation with respect to $\alpha$
$C_{m\delta_e}$	Pitch moment coefficient variation with respect to $\delta_e$
$C_{m\dot{\alpha}}$	Pitch moment coefficient variation with respect to adimensional derivative of $\alpha$
$C_{m\dot{\delta_e}}$	Pitch moment coefficient variation with respect to adimensional derivative of $\delta_e$
$C_{m\dot{q}}$	Pitch coefficient variation with respect to adimensional pitch rate
$C_{m\dot{u}}$	Pitch moment coefficient variation with respect to adimensional $u$
$C_{m_0}$	Pitch coefficient zero $\alpha$
$C_{n\delta_a}$	Yaw moment coefficient variation with respect to adimensional $\delta_a$
$C_{n\delta_r}$	Yaw moment coefficient variation with respect to adimensional $\delta_r$
$C_{n\dot{r}}$	Yaw moment coefficient variation with respect to adimensional derivative of $r$
$C_{n\dot{p}}$	Yaw moment coefficient variation with respect to adimensional $p$
$C_{n\dot{r}}$	Yaw coefficient variation with respect to adimensional yaw rate
$C_{n\beta}$	Yaw coefficient variation with respect to $\beta$
$C_{prop}$	Propeller efficiency parameter
$c_{root}$	Wing Root chord
$c_{tip}$	Wing Tip chord
$C_{X\alpha}$	X Force coefficient variation with respect to $\alpha$
$C_{X\delta_e}$	X Force coefficient variation with respect to $\delta_e$
$C_{X\dot{u}}$	X force coefficient variation with respect to adimensional $u$
$C_{Xs}$	Force coefficient in X body direction (reference state)
$C_{Y\beta}$	Y Force coefficient with respect to $\beta$
$C_{Y\delta_r}$	Y Force coefficient variation with respect to
$C_{Y\dot{p}}$	Y Force coefficient variation with respect to adimensional $p$

$C_{Y\hat{r}}$	Y Force coefficient variation with respect to adimensional r
$C_{Z\alpha}$	Z Force coefficient variation with respect to $\alpha$
$C_{Z\delta_e}$	Z force coefficient variation with respect to $\delta_e$
$C_{Z\hat{\alpha}}$	Z Force coefficient variation with respect to adimensional derivative of $\alpha$
$C_{Z\hat{q}}$	Z force coefficient variation with respect to adimensional q
$C_{Z\hat{u}}$	Z Force coefficient variation with respect to adimensional u
$C_{Zs}$	Force coefficient in Z body direction (reference state)
$D$	Dimensionless derivative
$D$	Drag
$F1, F2$	Forces measured in load cells
$f_d$	Measured frequency of the oscillations
$f_n$	Calculated natural frequency
$F_{Ax}$	Aerodynamic force in X body direction
$F_{Ay}$	Aerodynamic force in Y body direction
$F_{Az}$	Aerodynamic force in Z body direction
$F_{Tx}$	Propulsive force in X body direction
$F_{Ty}$	Propulsive force in Y body direction
$F_{Tz}$	Propulsive force in Z body direction
$F_{A/T_x}, F_{A/T_y}, F_{A/T_z}$	Aero-propulsive forces in X,Y, and Z body directions
$g$	Gravity
$H_u$	Dryden's transfer function for turbulence velocity in X body direction
$H_v$	Dryden's transfer function for turbulence velocity in Y body direction
$H_w$	Dryden's transfer function for turbulence velocity in Z body direction
$I_x, I_y, I_z, J_{xz}$	Inertia moments
$I_x$	Inertia momentum in X body direction



$I_y$	Inertia momentum in Y body direction
$I_z$	Inertia momentum in Z body direction
$J_{xz}$	Off-diagonal Inertia momentum
$k_d$	Derivative gain
$k_i$	Integral gain
$k_p$	Proportional gain
$K_\omega$	Engine throttle command to rpm experimental parameter
$k_{motor}$	Engine out-coming air stream velocity experimental parameter
$K_{Tp}$	Engine rpm to counter-torque experimental parameter
$L$	Lift
$L_u$	Turbulent scale parameter for X body direction
$L_v$	Turbulent scale parameter for Y body direction
$L_w$	Turbulent scale parameter for Z body direction
$L_A$	Aerodynamic moment in X body direction
$L_T$	Propulsive moment in X body direction
$L_{A/T}, M_{A/T}, N_{A/T}$	Aero-propulsive moments in X,Y, and Z body directions
$m$	Total mass
$M_A$	Aerodynamic moment in Y body direction
$M_T$	Propulsive moment in Y body direction
$N_A$	Aerodynamic moment in Z body direction
$N_T$	Propulsive moment in Z body direction
$p, q, r$	Angular velocities in X,Y, and Z body directions
$p$	Angular velocity in X body direction
$p_d$	Position in Z inertial direction
$p_e$	Position in Y inertial direction

$p_n$	Position in X inertial direction
$P_{downstream}$	Pressure downstream the propeller
$P_{upstream}$	Pressure upstream the propeller
$q$	Angular velocity in Y body direction
$r$	Angular velocity in Z body direction
$Re$	Reynolds number
$S$	Projected wing area
$S_{prop}$	Propeller swept surface
$T$	Measured period of the oscillations
$T_{1/2}$	Time to double
$u, v, w$	Inertial velocities in X,Y, and Z body directions
$u$	Inertial velocity in X body direction
$u_s$	Cruise velocity
$v$	Inertial velocity in Y body direction
$V_a$	Incoming airspeed
$V_{exit}$	Propeller exit stream velocity
$W$	Weight
$w$	Inertial velocity in Z body direction
$X_{CG}, Y_{CG}$	Center of gravity coordinates
$X_{NP}$	Neutral Point coordinate

# 1 Introduction

## 1.1 Motivation and objectives

Recently there has been a big development of small UAVs, facilitated by new manufacturing techniques such as 3D printing or automatic machining. In addition, electronic devices for navigation such as sensors, autopilots, transmitters, etc., have become smaller, more powerful, and more affordable. One important part in the design of manned and unmanned new concept aircraft is the determination of their stability properties, which helps in the design of flight control systems. Computational Fluid Dynamics (CFD) software is often used, however, complementary experimental tests are needed.

In the case of small UAVs, due to their low-cost nature, is usual to use rough methods when tuning the flight controllers. Performing wind tunnel experiments helps to estimate the dynamic response of the UAV model in order to design flight controllers.

The main objective of this study is, therefore, to find an efficient and comprehensive method to design flight controllers for small UAVs. Within this main goal, this work also intends to analyze what are the most important aerodynamic features from the point of view of control and design of low-cost wind tunnel experiments.

Moreover, as discussed in the abstract section, flying wings are a kind of aircraft with the potential to considerably reduce fuel consumption in commercial aviation. For this reason, it is interesting to study these types of aircraft so the selected configuration is the flying wing.

The objectives of this study are not only theoretical. The ideas are also implemented so a flying wing prototype is built and tested in a wind tunnel. The main objectives of the study are summarized below:

1. Understand the aerodynamics of flying wings type of aircraft and learn how this applies to flight dynamics and control.
2. Find the most important dynamic properties regarding control design.
3. Design low-cost wind tunnel experiments to determine these important properties.
4. Compare the experimental results with simulation results.
5. Find design solutions to improve stability.
6. Implement a control system and adjust it to obtain good performance.

## 1.2 Project's timeline

In figure 1, the temporal distribution of the different works is presented. This study involves manual activities to manufacture the prototype, as well as design activities. The

scheduling of the tasks is important to be able to perform the wind tunnel experiments when the tunnel is available.

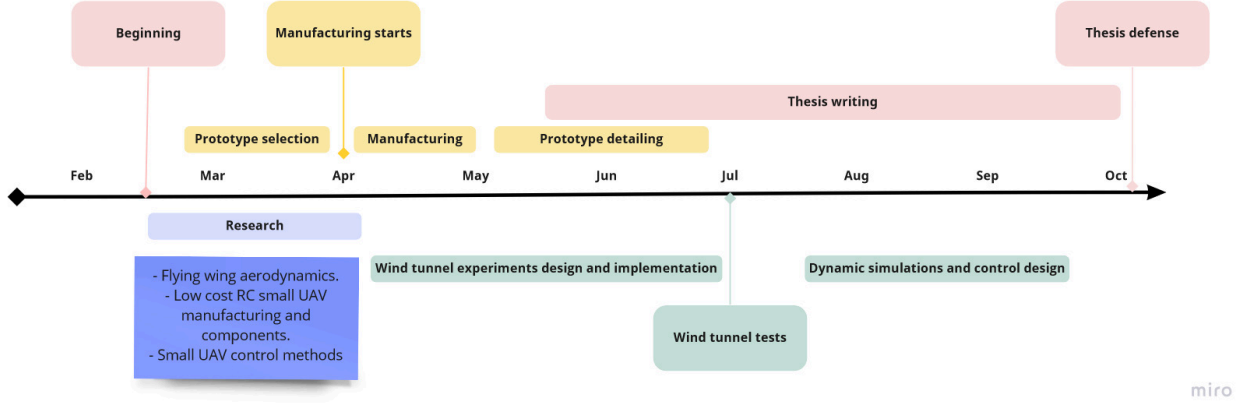


Figure 1: Project's timeline

### 1.3 Thesis outline

In the first chapter, the important aspects of flying wing design, flying wing aerodynamics, and flight dynamics and control design are introduced as well as some relevant books and articles.

In the second chapter, all the details about the built prototype are given, starting with the prototype selection criteria, followed by an aerodynamic study done with *XFLR5* software, and later the manufacturing process and the determination of the center of gravity and inertia moments. Geometrical, aerodynamic, and mass properties are described.

In the third chapter, the dynamic equations used are presented, linearized, and implemented in *MATLAB*, and the results are compared with the *XFLR5* modal estimation. Also, the stability properties of the built prototype are discussed, compared, and enhanced. The results are contrasted with the results of other similar works.

The fourth chapter explains in detail the wind tunnel experiment planning, execution, and results. The experimental results are compared with *XFLR5* and discussed. Static and dynamic experiments are carried out in the wind tunnel available at Instituto Superior Técnico.

The fifth chapter explains how the dynamic model is implemented in *SIMULINK*. The linearization process is described and its results are compared with *XFLR5* ones. The last chapter discusses the control system design process explaining. First, the structure of the control system is presented. Subsequently, the design process is qualitatively and quantitatively described. Finally, the final design and test simulations are shown.

## 2 Research and State of Art

As introduced in the previous chapter, small UAVs are a great way to assess the feasibility of new aircraft configurations. For this reason, it is interesting to design and build small UAVs to test novel aircraft configurations. The selected aircraft configuration, as said before, is the flying wing. When there is a need for extremely low drag, such as for the long endurance objectives one possible configuration is the flying wing. This advantage makes the flying wing also suitable for UAV surveillance missions.

The history of the development of the flying wing can be found in [12] of which a synopsis is given here.

### 2.1 The development of the flying wing

The following sub-section is a synopsis made from the article [2].

The first attempts to design a Flying Wing (FW) started in Europe in 1910, however, none of them was ever built, and the engineers could not solve the stability problems created by the lack of a tail. Germans engineers were pioneering in this kind of aircraft, during 1910 Hugo Junkers patented a Flying Wing (FW) model which was never built.

In 1929, Northrop company made the first successful design of a FW (figure 2), the model was called No.1. This model was not a pure FW because Northrop placed a small-sized tail with a little rudder and elevator control. The wing was powered by a 90 HP reciprocating engine, the aircraft proved to be stable and its aerodynamic performance was better than similar size aircraft.



Northrop "Experimental No. 1" Pusher (NX216H)

Figure 2: Northrop No. 1. Source: Skytamer

During the '30s, the Horten Brothers, from Germany, gain experience in the design and building of all-wing gliders (figure 3), however, due to peace treaties from WWI Germany was not allowed to build engine-powered aircraft.

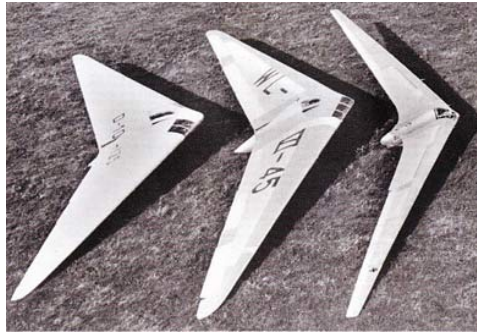


Figure 3: Horten's all-wing gliders Source: Fiddlersgreen

During the interwar period, Northrop grew considerably and continued pushing the FW to become a reality. Northrop recruited Dr. Von Karman, one of the greatest aerodynamic experts living in the US. After some scaled prototype wind tunnel and flight tests, Northrop engineers decided to build a full-scale model. One of the main concerns of the engineers was lateral stability, they thought that the aircraft could be unrecoverable after entering in a spin because of the lack of tail. Hopefully, it was proved that full-scale models were stable.

The aircraft depicted in figure 4, was called the N-1M. The N-1M was powered by two 65 HP Lycoming engines. This model was the first successful powered all-wing aircraft. Pitch and roll movements were commanded by the same control surfaces, that deflected in the same direction for pitch and in the opposite direction for roll maneuvers. For yaw control the design solution was a couple of split-flaps located at the wing tips, these flaps deflected upwards and downwards creating drag but not extra lift.

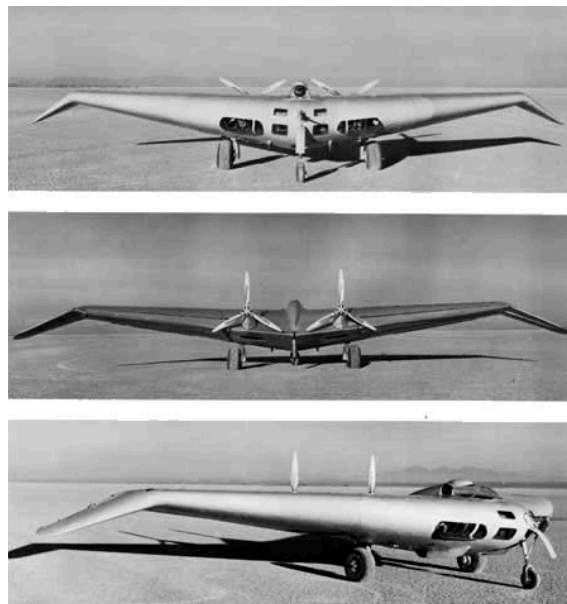


Figure 4: Northrop N-1M aircraft Source: aire.org

In the first flight test, several problems were detected. The negative dihedral given to the wings was found to be unstable, also it was noticed that the more wing sweep the more stable the aircraft was.

During WWII, the US army encouraged Northrop to continue with the design of FW. Northrop took the challenge of designing the XB-35 aircraft for the army, firstly developing the N9-M as a pre-design for the XB-35. Engineers were concerned about the lack of lateral stability, it was found to be a genuine problem of tail-less aircraft. One important problem was the stall behavior, the N9-M tends to stall first on wing tips losing both elevator and aileron control entering in unpredictable and dangerous stalls.

On the German side, Horten Brothers continue with the development of FW designing the first jet-powered all-wing aircraft, the Horten Ho XI V-2 in 1945 (see figure 5. Messerschmitt also designed the first fighter FW, (see 6). The jet-powered aircraft was called Me163, it was provided with a little vertical fin with rudder control.

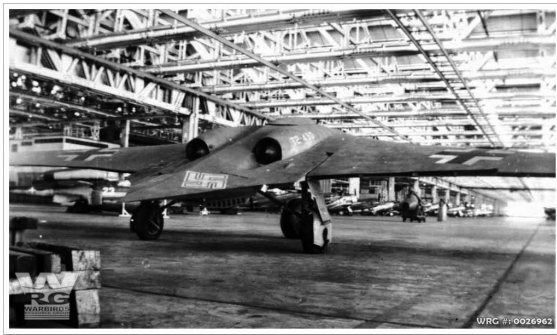


Figure 5: Horten Ho XI V-2, Source: warbirds



Figure 6: Me163, Source: mourningtheancient

The aircraft in figure 7 is Northrop's prototype XB-35. It was flown in 1946 by an Army pilot with neither incidents nor difficulties. The reciprocating engines were a source of problems due to vibrations and lack of reliability of the gearboxes, thus they were replaced by General Electric jet engines. It was known that the pusher propeller configuration at wing trailing edges helped lateral stability, to compensate the problem of removing the propellers the aircraft was provided with vertical fins. The name of this prototype, depicted in figure 8, changed to YB-49. YB-49 beat several velocities and endurance records. However, the poor lateral stability caused the YB-49 to yaw-oscillate during the bomb dropping. At this point Northrop designed and integrate a yaw damping system using new control technologies with successful results.



Figure 7: Northrop XB-35, Source: theaviationclub]

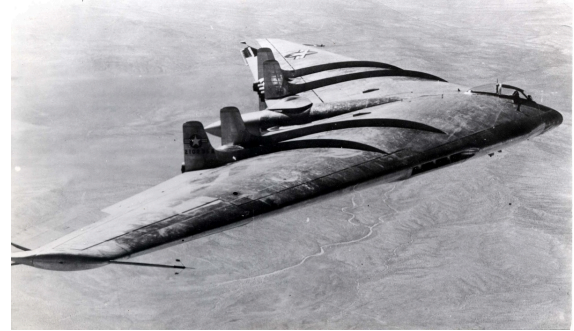


Figure 8: Northrop YB-49, Source: avionslegendaires

The YB-49 was discovered to have a small radar footprint because of the all-wing shape, the fact that would trigger the development of the most advanced FW aircraft ever built, the B-2 stealth bomber, presented in figure 9.



Figure 9: Northrop B-2 Stealth bomber Source: militarymachine

In 1988 the first Northrop B-2 was ready to fly. Unlike its predecessor, the B-2 has no vertical fins. The great advance in flight computers made possible this pure all-wing



aircraft, overcoming genuine stability issues.

## 2.2 Aerodynamics and flight dynamics of flying wings

One of the main advantages of FW and Blended-Wing-Body (BWB) is that lift to drag relation is higher. The cruise lift-to-drag ratio of BWB and FW usually increases compared to the conventional. The smooth integration of fuselage and wing in FW and BWB leads to better aerodynamic properties. Lift in conventional fuselages is small but greatly contributes to drag. Moreover, FW and BWB configurations have higher wing surfaces than conventional for the same MTOW, diminishing wing load. Lower wing load implies lower stall speed so there is no need for high-lift devices reducing complexity and increasing efficiency. For more information see [3].

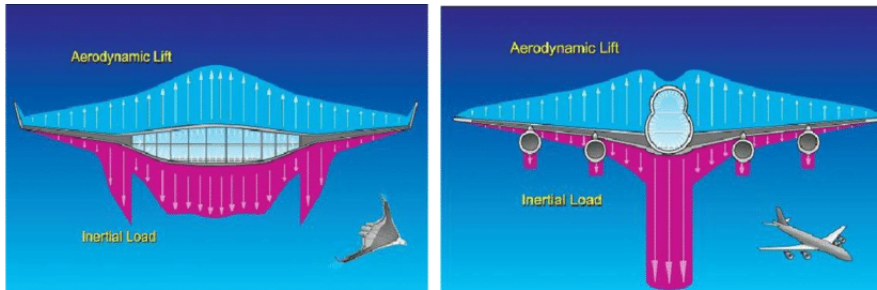


Figure 10: Span-wise lift and weight distributions Source: Researchgate

One advantage of BWB and FW aircraft is that the span-wise lift and weight distributions, (see figure 10), are more balanced than conventional aircraft, weight distribution spreads along the wing reducing structural loads and complexity.

### 2.2.1 Airfoil and wing design

According to [4], one of the main aspects when designing FW or BWB is the airfoil. The main problem is that the absence of the tail makes the longitudinal trim and longitudinal stability complex. Having a tail with a large arm makes it easier to compensate the pitch moment generated by the wing. In tailless configurations, the compensation is made by the elevators at the trailing edge of the wing, with a much shorter arm. Thus, airfoils must be designed not only for good aerodynamic performance but also for making easier the pitch moment trim. Furthermore, the sweep is essential for achieving acceptable lateral dynamic stability.

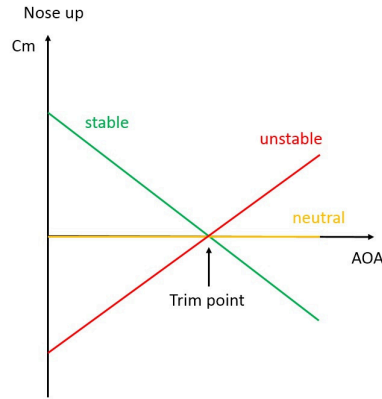


Figure 11: Pitch moment vs alpha (Longitudinal stability), Source: engineeringpilot

In the picture 11, it can be seen that  $Cm_\alpha$  must be negative in order to have longitudinal stability. However, the margin of stability cannot be high, (namely big down-slope in the graph), because the changes in trim condition greatly affect the pitch momentum so bigger elevator trimming is needed.

### 2.2.2 Achieve positive $Cm_0$

Wing and airfoil design must ensure positive  $Cm_0$  to achieve positive Angle of attack (AoA) of equilibrium, this can be noticed in figure 11 as well. According to [5] there are many methods to achieve this:

One way of designing the airfoil to get  $Cm_0 > 0$  is by introducing a reflex camber, as can be seen in figure 12. However, high values of reflex camber deteriorate aerodynamic properties, especially boundary layer separation and stall properties. The other way is giving sweep-back and twist to the wing. If the wing tips are twisted with negative incidence (tip washout) they create a local positive pitch moment. Enough twist values can achieve positive  $Cm_0$ . Furthermore, spanwise lift distribution is important, it results from the wing plan form and spanwise twist distribution. Sweep and tapered wings tend to have a higher loading near the wing tip, which causes the tip to stall first, twist also mitigates this problem. As can be seen, the solution is a trade-off between the wing and airfoil design.

In fact, it is possible to use any airfoil, longitudinal stability can always be achieved by selecting a suitable combination of sweep and twist, (see figure 12). However, the best performance is attained by airfoils with low moment coefficients (around zero). They need smaller amounts of twist, which results in a broader speed range without paying too many penalties out of the design point.

Twist distribution is especially important in FW, a common design feature in many

aircraft is a wing-tip washout, giving a negative twist (reduce incidence) at wing tips. Thus, achieving the elliptical lift distribution but also reducing load at wing tips, improving wing stall properties, and moreover increasing  $Cm_0$ .

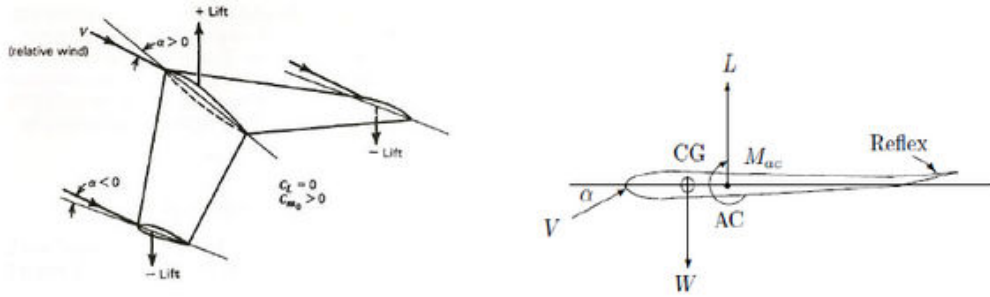


Figure 12: Ways to achieve  $Cm_0$  Source:[4]

Low moment coefficients and a small amount of twist can be achieved by airfoils with little, neutral, or slightly reflexed camber line. The drawbacks of reflex camber are that lift is reduced, so the maximum lift coefficient diminishes, leading to higher stall speed. For most tailless planes, airfoils with low moment coefficients yield the best performance.

Low moment coefficients and high lift coefficients can be achieved by using reflexed camber lines. However, the corresponding velocity distributions for moderated reflexed camber lines are sensitive to low Reynolds numbers and may result in problems with stall behavior. The best compromise for light, tailless airplanes seems to be a moderately reflexed camber line, combined with the maximum camber shifted towards the leading edge and a rather blunt nose. The rest of the work is made by wing design, carefully designing sweep twist and taper ratio.

To complete this information the reader is referred to the work [1] where the aerodynamic design of a flying wing is described and carried out.

## 2.3 Flight dynamics

From the works [4], [6] and the article [7] some relevant conclusions can be obtained.

The absence of a tail greatly affects all stability properties of the aircraft. Longitudinal and stability modes are usually less damped so the aircraft is harder to stabilize. Passive longitudinal stability improvements are difficult, and the absence of a horizontal stabilizer is hard to replace. Carefully setting the COG position improves stability. However, FW elevator power control is small compared with conventional aircraft, if the stability margin is increased by changing COG, any change in lift greatly affects pitch moment hence, it

makes harder the longitudinal trimming.

Lateral stability can be improved with passive methods including vertical fins at trailing edges and winglets that make the role of a vertical stabilizer. However, the effectiveness of vertical fins is small due to the short momentum arm. Hence, weight and drag penalties of including fins usually surpass the lateral stability advantages. The best solution is to include winglets at wing tips which also improve aerodynamics reducing wing-tip vortex drag. Wing design also improves lateral stability, the bigger the sweep-back the better stability. Another way is to crank the wing's last section giving a negative dihedral, and increasing the wing lateral area. Moreover, in the case of propeller-driven aircraft, pusher propeller configuration improves lateral stability.

Another issue of FW is directional control. Usually, the best solution for this issue is to have split-aileron, which can be observed in figure 13, near the wing tips. These ailerons deflect up and down the same way creating drag but no lift.

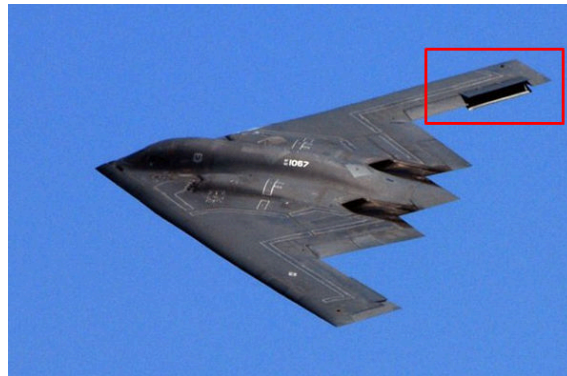


Figure 13: Northrop B-2 Split-Ailerons Source: Quora

Given their stability issues, FW needs powerful flight control systems to comply with flight dynamics specifications regarding airworthiness.

## 2.4 Introduction to flight control

This section gives an overview of flight control for small UAVs is mainly based on [7].

Firstly discusses the control system, the different levels of autonomous flight, and the different control layers for a UAV. Secondly, focusing on how to control the physical system, introduces the classical control theory, closed-loop feedback, transfer-function, and Proportional Integrative Derivative (PID) controllers. Also briefly explaining the different control theories, typical system analysis tools, and control strategies and approaches. Finally talking about state estimation and sensors.

This section is supposed to organize the ideas and give a structured overview of the control world applied to UAVs, the different concepts will not be explained in depth.

#### 2.4.1 Level of autonomy and control system layers

Depending on the level of autonomy the control system is more or less complicated. The different levels of autonomy for UAVs are shown in figure 14. For the first level of autonomy, only one layer of control is needed, it is only a basic controller that translates the pilot inputs to actions, for example achieving and holding the desired attitude against disturbances. The other levels involve extra control layers that must be able to take decisions, for example, which path to follow, how to follow the path, etc. These layers are usually called Flight Directors. In this case, the pilot does not need to command the UAV, he needs just to plan a mission. At the highest levels of autonomy, the UAV is able to design and execute a mission itself.

Autonomy Levels	
Level	Description
1	Remote Control
2	Automatic Flight Control
3	System Fault Adaptive
4	GPS Assisted Navigation
5	Path Planning & Execution
6	Real Time Path Planning
7	Dynamic Mission Planning
8	Real Time Collaborative Missing Planning
9	Swarm Group Decision Making
10	Full Atonomous

Figure 14: List of autonomy levels (AL) with descriptions. Source: researchgate

#### 2.4.2 The classical control theory

Control theory is a group of concepts, methods, and rules that analyses dynamic systems with the purpose of understanding their behavior and managing them according to certain necessities.

This theory was mainly developed in the XX century. Is the basis of modern control and is still widely used in many industrial applications, however certain systems, like aircraft, often require more complex control techniques.

It is based on open/closed-loop feedback, depicted in figure 15. The variable to control is measured with a sensor, the controller computes the error between the desired and current value and commands the actuator to diminish it.

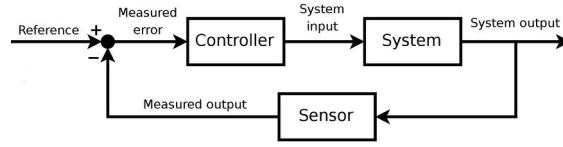


Figure 15: closed-loop feedback (Block Diagram representation). Source: wikipedia

Every control theory involves mathematics to model reality, usually, the best way to simulate physical systems is to model them using differential equations (DE). Classical control theories are based on DE linear systems which are an easy way to simulate, study, and understand the physical system. However, many physical systems are non-linear and they first need to be linearized.

The fathers of classical control theory developed many tools to study the behavior of linear systems like root-locus plots, Nyquist and bode diagrams, stability criteria, etc. Most of these tools use the frequency domain analysis technique, which consists in applying the Laplace transform to the DE system to convert DE into algebraic equations. All classical analysis tools are based on the transfer function (TF) of the system, which is the result of applying the Laplace Transform to the DE system.

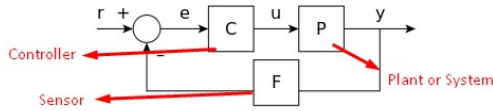


Figure 16: Closed-loop block diagram, Source: wikipedia

$$\begin{aligned} Y(s) &= P(s)U(s) \\ U(s) &= C(s)E(s) \\ E(s) &= R(s) - F(s)Y(s). \end{aligned}$$

$$\begin{aligned} Y(s) &= \left( \frac{P(s)C(s)}{1 + P(s)C(s)F(s)} \right) R(s) = H(s)R(s) \\ H(s) &= \frac{P(s)C(s)}{1 + F(s)P(s)C(s)} \end{aligned}$$

Figure 17: Closed-loop math expressions Source: wikipedia

In figure 16, the blocks C, P, and F represent the Laplace transform of each system. In figure 17, the closed-loop transfer function is deducted. Once the transfer function is known, designers can easily study the system, ensure that it is stable under closed-loop feedback, improve its stability, tune the controllers to achieve optimal performance, etc.

The Proportional Derivative Integrative (PID) controller, presented in figure 18, is the most cost-effective control technique, which even nowadays is widely used in many applications because of its robustness and lack of complexity. However it has limitations, for example, it can only control SISO systems, when trying to control multiple variables through multiple inputs other techniques must be used.

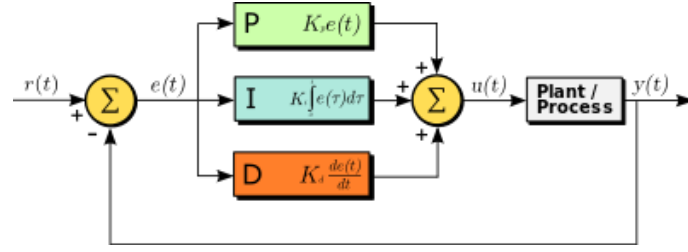


Figure 18: PID controller Source: wikipedia

PID controls the system in three ways: firstly proportional control, the bigger the error the bigger the control action. Secondly, derivative error, if the error is diminishing quickly it reduces action if the error diminishes slowly or raises the action increases. Finally, the integral control deals with the stationary errors and disturbances, if the error remains in time despite being small the integral control adds it up over time increasing the action of the controller.

#### 2.4.3 Linear an non-linear control theories

As said before, linear control theory applies to DE linear systems, if the coefficients of the DE system are constant in time is called Linear Time Invariant (LTI) system. LTI systems are very powerful representations and easy to study, they are usually analyzed in the frequency domain with different tools such as Bode plot, root locus, Nyquist stability criterion, etc. Also, LTI systems are described in terms of bandwidth, eigenvalues, eigenvectors, resonant frequencies, poles and zeros etc. All these tools and concepts to characterize LTI system provide the designer with all the necessary information to correctly built controllers that meet the requirements.

On the other hand, nonlinear control theory does not support any linearization of DE systems, it works with the nonlinearity of the equations keeping the whole information inside them. Nonlinear control is more complex but gets rid of the limitations inherent to linear systems. There are mathematical techniques that have been developed to handle these systems, tools such as limit cycle theory, Lyapunov stability theorem, etc. Nonlinear systems are usually analyzed using numerical methods on computers. In some cases, when controlling a complex system, the nonlinear approach might give some advantages, however in many other situations, the complexity overcomes the real advantages in terms of control, making linear control more suitable.

#### 2.4.4 Important concepts in control theory

**Stability** is the first objective of a control system, the controller must ensure system stability in all situations.

A linear system is called Bounded Input Bounded Output (BIBO) stable if its output is bounded for any bounded input, which means that the output of the system will not raise indefinitely in response to finite inputs, see figure 19. For nonlinear systems with input a similar concept is that of ISS, which combines Lyapunov stability and a concept similar to BIBO stability.

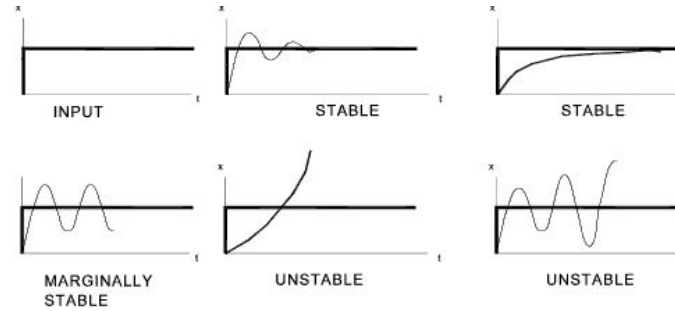


Figure 19: System behaviour, Source: controlsystemengineer

In terms of frequency domain analysis, stability means that all of the poles of a linear system's transfer function must have negative-real values. Thus, stability requires the complex poles to be located in the left part of the complex plane.

**Controllability and observability** are one of the first tasks a designer has to accomplish before deciding the best control strategy, or whether it is possible to control or stabilize the system. Controllability is the possibility to conduct a system to a certain state by using an appropriate control signal. If a state is not controllable, then no signal will ever be able to control the state. However, if a state is not controllable, but its non-controllable dynamics are naturally stable, the system is considered to be stabilizable. Observability is the possibility to determine states through output measuring. If a state is not observable, the controller is not able to measure the state nor control it. However, if a state cannot be observed it might still be detectable. These properties are studied by analyzing the system's eigenvalues.

### General control specs

A control problem usually has many specifications. Stability is always present. Sometimes it is necessary to obtain certain dynamics in the closed loop by using techniques such as pole placement, root-locus, etc. Another usual specification is the rejection of a constant disturbance; including an integrator in the open-loop chain. Furthermore, with techniques such as loop-shaping, noise rejection is achieved by modifying the frequency response of the system to reject certain frequencies acting as a filter. Other classical control



theory specifications regard the time-response of the closed-loop system. These include the system's properties such as the rise time, peak overshoot, settling time, quarter decay, etc.

**Robustness** means that the controlled system's properties do not change much if applied to a system slightly different from the mathematical model used for the design. A particular robustness issue is actuator saturation. In the physical world, every signal is limited, for example, UAV's control surfaces have certain limits, and if controller design overloads those limits the system's performance worsens.

The analysis of the robustness of a (Single Input Single Output) SISO control system can be done in the frequency domain, using the system's transfer function Nyquist and Bode diagrams. Topics include gain and phase margin and amplitude margin. For Multiple Inputs Multiple Outputs (MIMO) systems it is more complicated.

**The Control Strategies** are selected by the designers depending on the control needs and complexity. There are many different strategies such as Adaptive control, which uses real-time identification of the process parameters, modification of controller gains, Intelligent control, which uses AI methods, optimal control, where the control signal optimizes a certain "cost index", etc.

#### 2.4.5 State observation and Kalman filters

All control theories are based on measuring certain states and generating an error signal by closed-loop feedback. However not every state can be measured directly, for example, Euler angles in the case of UAVs. In Figure 20 it can be seen an example of how to determine these states and generate the error signal, it is called an estimator or state observer.

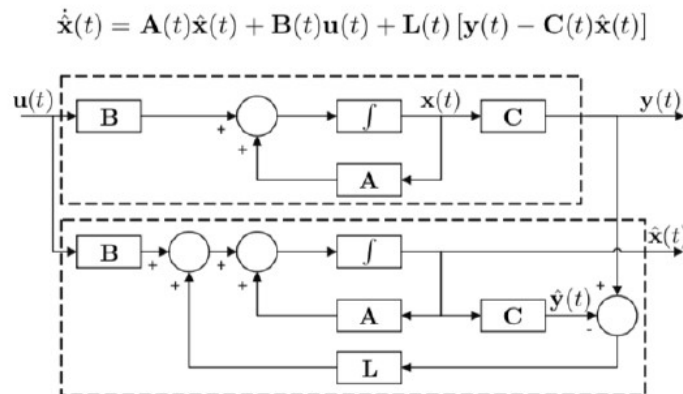


Figure 20: State estimator block diagram Source:[8]

To enhance the accuracy of the estimator usually two or more measurements are used. For example, to compute Euler angles, gyroscope and accelerometer data are used. Depending on UAV's dynamics and the quality and noise of the sensors, one of the magnitudes can be more reliable than the other. Kalman filters yield the optimal estimator accuracy given a-priori knowledge of the covariance of the disturbances acting on the system.

State estimators and Kalman filters are an important part of modern control techniques, usually applied to more complex systems with several sensors and states to control (MIMO systems).



The selected airfoil is the Eppler 186 (depicted in Figure 22), which is a good profile for flying wings as it has a slight reflex camber to give positive  $C_{m0}$ , which is important to ensure positive AoA of equilibrium, thus positive Lift. The airfoil details are given in table 1.

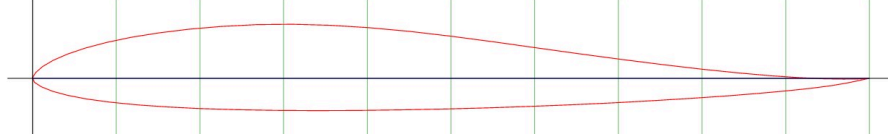


Figure 22: Eppler 186 airfoil Source:link.

Max thickness	position	Max camber	position	Root chord ( $c_{root}$ )	Tip chord ( $c_{tip}$ )
10.2%	29%	0.8%	29%	275mm	150mm

Table 1: Airfoil details

The prototype has the same airfoil along the wingspan. Winglets, (which can be seen in detail in figure 23) are completely flat, however, in *XFRL5*, airfoils *NACA 0010* are used to simulate the winglets. These airfoils are symmetric so no lift is generated for  $\beta = 0$ . Although, results will change when  $\beta \neq 0$ . All wing details can be checked in table 2.

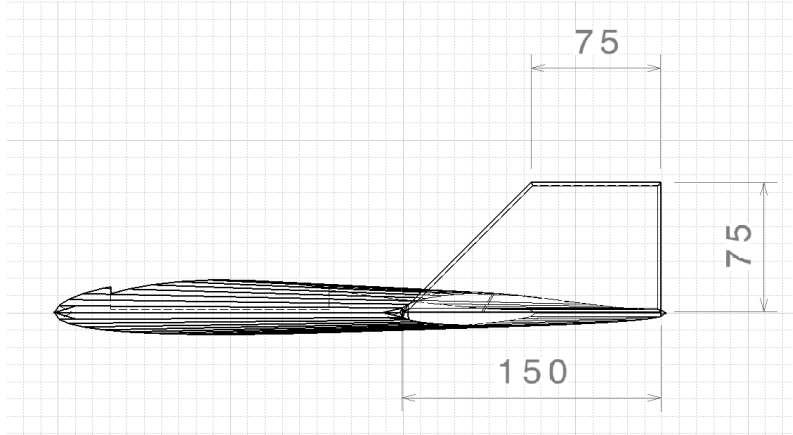


Figure 23: Prototype geometry (side view).

Wing surface (S)	Wingspan (b)	MAC ( $\bar{c}$ )	Tapper ratio ( $\lambda$ )	aspect ratio (A.R)	Sweep ( $\Lambda$ )	Dihedral ( $\Gamma$ )	Twist ( $\theta$ )
0.202m <sup>2</sup>	950mm	219mm	0.545	4.468	19.56°	0°	0°

Table 2: Wing properties

### 3.2 Aerodynamic study

Previous to the manufacturing step, a short study is done to determine the aerodynamic properties of the model and design the component placement to ensure longitudinal

stability. *XFRL5* is user-friendly, cost-effective simulation software. It is also commonly used in the design of small UAVs, as can be seen in [6],[11],[12],[13].

*XFRL5* is a software to study aerodynamic bodies, it is based on the aerodynamic potential theory. It implements several methods such as *Vortex Lattice*, *Doublet Lattice* or *Panels* to calculate lift and induced drag forces. This software is capable of performing 2D calculations, which are based on *XFOIL* software. *XFOIL* includes a good estimation of boundary layer physics and viscous drag estimations. Moreover, *XFRL5* is able to perform 3D analysis, but 3D viscous effects are interpolated from 2D results lowering the accuracy and underestimating viscous drag. For more information see [14].

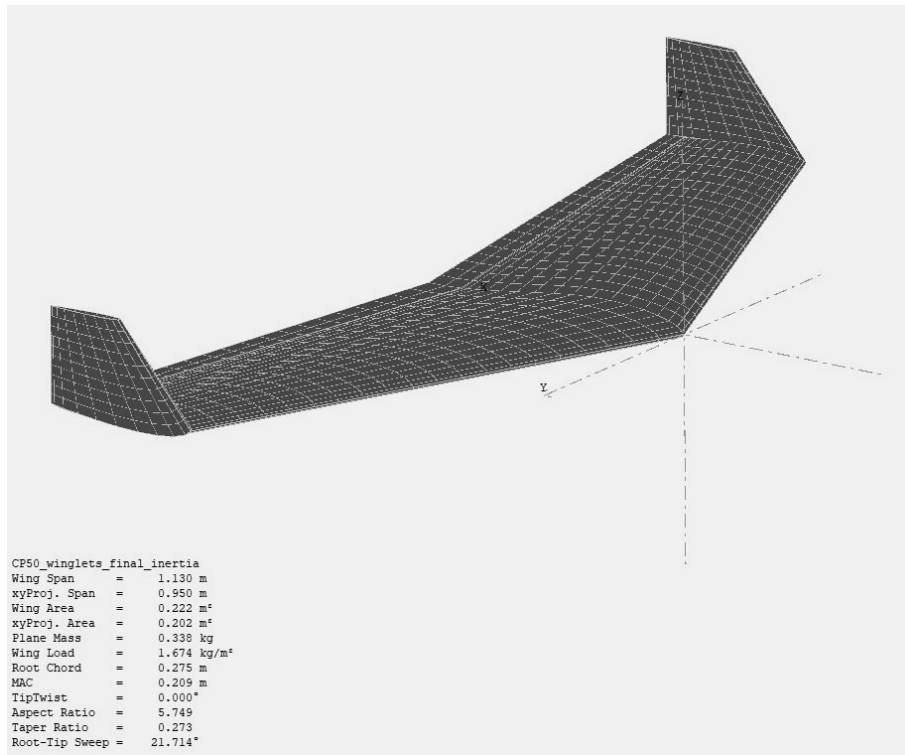


Figure 24: Prototype panel distribution in *XFRL5*.

The prototype is modelled in *XFRL5*, see Figure 24, the panel distribution can be seen in table 3. Some of the aerodynamic properties, such as the momentum coefficients depend on the center of gravity location. It is not possible to know the mass configuration ad-hoc. For the first studies, the mass properties were estimated with the mass of the components and *XFRL5* wing mass and inertia calculations. The following results are updated with the final center of gravity position obtained from experiments.

Part	X number	X distribution	Y number	Y distribution
Main wing	20	Cosine	20	Uniform
Winglets	10	Cosine	10	Uniform

Table 3: XFRL5 panel distribution

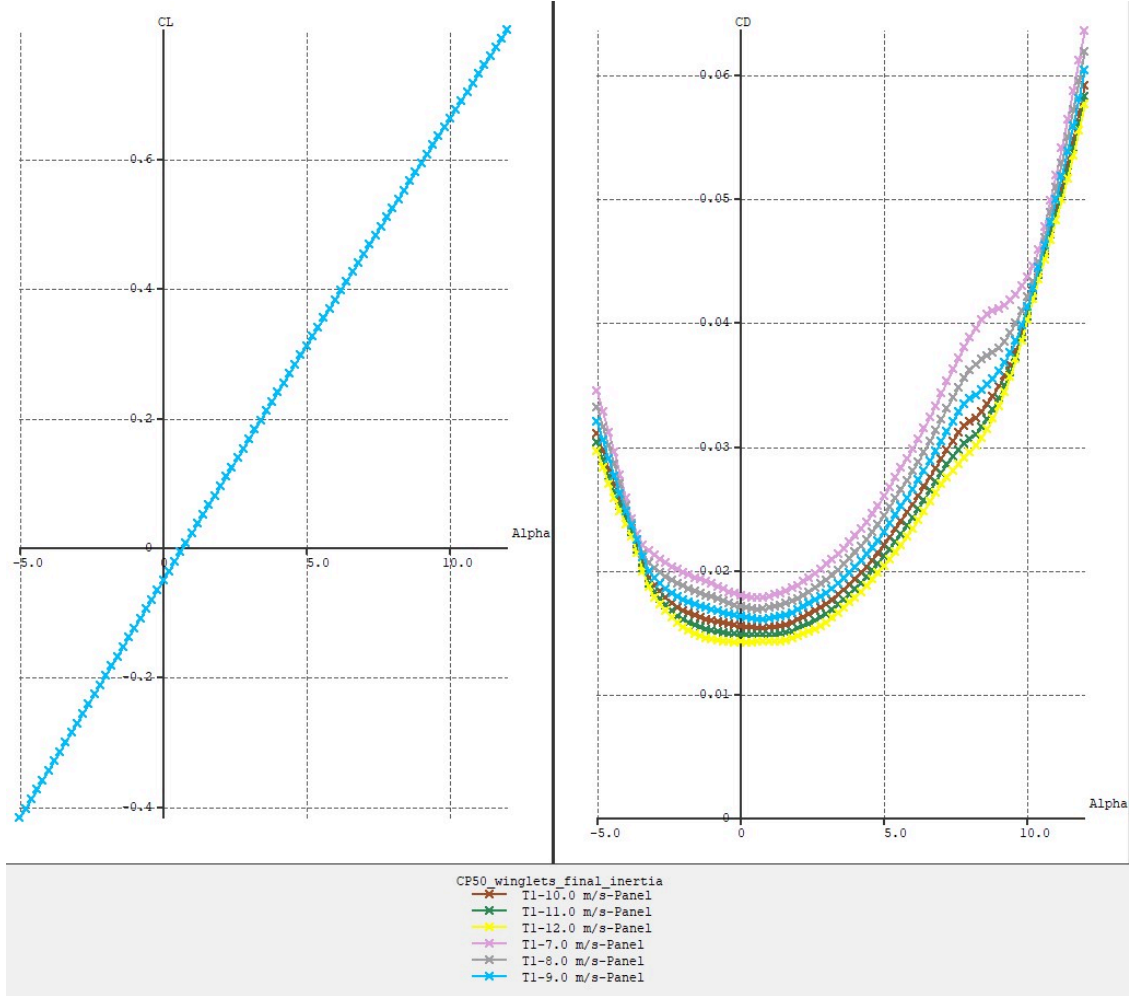


Figure 25:  $C_L(\alpha)$  and  $C_D(\alpha)$  curves for various airspeed (final version).

In figure 25 one can see that  $C_{L0}$  is negative because of the reflex camber effect.  $C_L$  curve is not affected by airspeed because no viscous physics are included in the potential theory (see [15]). In *XFRL*, the stall region cannot be interpolated to 3D (see technical documentation [14]). Regarding drag, it is affected by the airspeed through the Reynolds number. The drag coefficient is reduced as the Reynolds number increases.

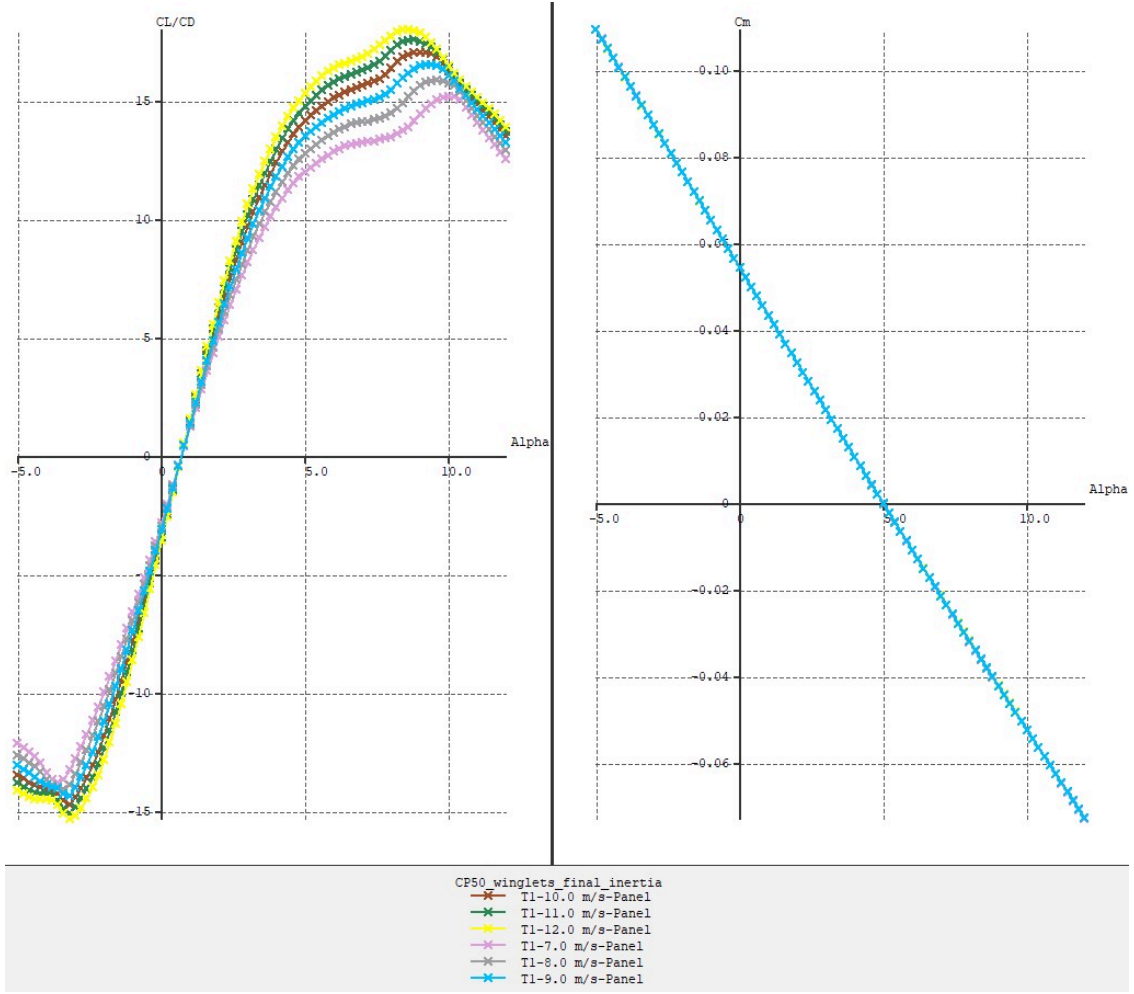


Figure 26: Efficiency and  $C_m(\alpha)$  curves for various airspeed (final version).

In figure 26, it can be seen that the AoA of equilibrium is close to  $5^\circ$ . Looking at the left graph, it seems that it is better to fly at high AoA to improve efficiency. The slope of the  $C_m$  graph depends on the mass distribution, which can be different in the real prototype so that the AoA of equilibrium.

As the final weight of the prototype is over  $3.31N$ , the stall speed is over  $7.5m/s$ . To achieve  $C_{Lmax}$  it is necessary to change the elevator position from neutral to a few degrees up. With elevators in neutral position, the cruise airspeed to achieve steady flight is  $9.4 m/s$ . In these conditions the minimum trust needed is  $0.242N$ .

### 3.3 Equations for aircraft modelling

In this section, the flight dynamic equations, and the linearization process are detailed. The reader can check in the nomenclature section the description of each variable or parameter that appears hereafter.

One of the most cost-effective control techniques is linear control. Linear control is easy to implement and analyze, and its results are very powerful.

The linear approach is usually used for aircraft flight stability analysis and control design, however, depending on aircraft flight properties, the linear analysis might not be sufficiently accurate. This work is oriented to small fixed-wing unmanned vehicles, so linear analysis is suitable for stability analysis and control tuning [16].

To build the dynamic aircraft model, first, the non-linear differential equations system is written. The equations presented in this chapter can be found in [17].

$$\begin{aligned} -mg \sin \theta + F_{Tx} + F_{Ax} &= m(\dot{u} - rv + qw) \\ mg \cos \theta \sin \phi + F_{Ty} + F_{Ay} &= m(\dot{v} + ru - pw) \\ mg \cos \theta \cos \phi + F_{Tz} + F_{Az} &= m(\dot{w} - qu + pv) \end{aligned} \quad (1)$$

$$\begin{aligned} L_T + L_A &= I_x \dot{p} - J_{xz} \dot{r} + (I_z - I_y)qr - J_{xz}pq \\ M_T + M_A &= I_y \dot{q} - (I_z - I_x)pr + J_{xz}(p^2 - r^2) \\ N_T + N_A &= I_z \dot{r} - J_{xz} \dot{p} - (I_x - I_y)pq + J_{xz}qr \end{aligned} \quad (2)$$

$$\begin{aligned} p &= \dot{\phi} - \dot{\psi} \sin \theta \\ q &= \dot{\theta} \cos \phi + \dot{\psi} \cos \theta \sin \phi \\ r &= -\dot{\theta} \sin \phi \cos \theta \cos \phi \end{aligned} \quad (3)$$

These equations are written in the body axis, the variable's names stand for the different angular, linear velocities, and forces. The absolute linear velocities are  $(u, v, w)$ , oriented in the direction of the body axes  $(x_b, y_b, z_b)$ . The Euler angles are  $(\phi, \theta, \psi)$ . The angular velocities along each body axis are  $(p, q, r)$ . Finally,  $F$  stands for linear force in the body axis and  $(L, M, N)$  are the momentum. The variables can be seen in Figure 27. The equations above (1,2 and 3) are respectively: linear momentum, angular momentum and cinematic angular relationship equation.



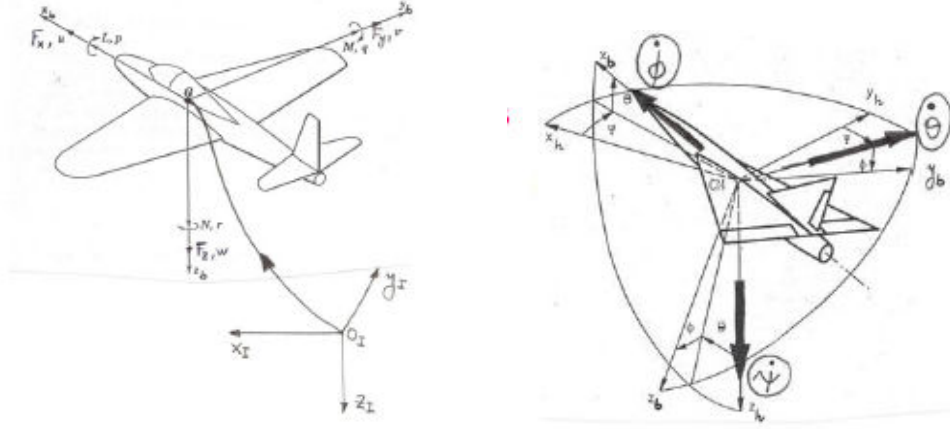


Figure 27: Notation Source:[17].

Subsequently, to linearize these equations, the variables are now a sum of a reference condition value plus a small variation (equations 4 and 5). These new variables are called incremental variables.

$$\begin{aligned}
 u &= u_s + \Delta u & p &= p_s + \Delta p & \psi &= \psi_s + \Delta \psi \\
 v &= v_s + \Delta v & q &= q_s + \Delta q & \theta &= \theta_s + \Delta \theta \\
 w &= w_s + \Delta w & r &= r_s + \Delta r & \phi &= \phi_s + \Delta \phi
 \end{aligned} \tag{4}$$

$$\begin{aligned}
 F_{Tx} &= F_{Tx_s} + \Delta F_{Tx} & F_{Ax} &= F_{Ax_s} + \Delta F_{Ax} & L_T &= L_{T_s} + \Delta L_T & L_A &= L_{A_s} + \Delta L_A \\
 F_{Ty} &= F_{Ty_s} + \Delta F_{Ty} & F_{Ay} &= F_{Ay_s} + \Delta F_{Ay} & M_T &= M_{T_s} + \Delta M_T & M_A &= M_{A_s} + \Delta M_A \\
 F_{Tz} &= F_{Tz_s} + \Delta F_{Tz} & F_{Az} &= F_{Az_s} + \Delta F_{Az} & N_T &= N_{T_s} + \Delta N_T & N_A &= N_{A_s} + \Delta N_A
 \end{aligned} \tag{5}$$

The equations are simplified by replacing the incremental variables in the equations (1,2 and 3). Small terms are also neglected and the following flight reference condition (equation 6) is applied. The simplified equations are (7,8 and 9).

$$\begin{aligned}
 p_s &= q_s = r_s = 0 \rightarrow \dot{\phi}_s = \dot{\theta}_s = \dot{\psi}_s = 0 \\
 v_s &= 0 \rightarrow \beta_s = 0 \\
 \phi_s &= 0
 \end{aligned} \tag{6}$$

The flight reference condition stands for steady, rectilinear and wing leveled flight. Steady reference condition means  $\dot{u}_s = 0$ ,  $\dot{v}_s = 0$ ,  $\dot{w}_s = 0$ ,  $\dot{p}_s = 0$ ,  $\dot{q}_s = 0$ ,  $\dot{r}_s = 0$ .

$$\begin{aligned}
 -mg \cos \theta_s \Delta \theta + \Delta F_{Tx} + \Delta F_{Ax} &= m(\Delta \dot{u} + w_s \Delta q) \\
 mg \cos \theta_s \Delta \phi + \Delta F_{Ty} + \Delta F_{Ay} &= m(\Delta \dot{v} + u_s \Delta r - w_s \Delta p) \\
 -mg \sin \theta_s \Delta \theta + \Delta F_{Tz} + \Delta F_{Az} &= m(\Delta \dot{w} - u_s \Delta q)
 \end{aligned} \tag{7}$$

$$\begin{aligned}
\Delta L_T + \Delta L_A &= I_x \Delta \dot{p} - J_{xz} \Delta \dot{r} \\
\Delta M_T + \Delta M_A &= I_y \Delta \dot{q} \\
\Delta N_T + \Delta N_A &= I_z \Delta \dot{r} - J_{xz} \Delta \dot{p}
\end{aligned} \tag{8}$$

$$\begin{aligned}
\Delta p &= \Delta \dot{\phi} - \Delta \dot{\psi} \sin \theta_s \\
\Delta q &= \Delta \dot{\theta} \\
\Delta r &= \cos \theta_s \Delta \dot{\psi}
\end{aligned} \tag{9}$$

The propulsive and aerodynamic forces must be linearized as well (equation 10). Following Bryan's work (see [17]), the non-steady nature of these forces can be modeled as follows:

$$\Delta X = X_u \Delta u + X_{\dot{u}} \Delta \dot{u} \quad \left\{ \begin{array}{l} X_u = \left( \frac{\partial X}{\partial u} \right)_s \\ X_{\dot{u}} = \left( \frac{\partial X}{\partial \dot{u}} \right)_s \end{array} \right. \tag{10}$$

In equation 10, for each aero-propulsive force, there are derivatives with respect to every single flight variable, these derivatives are called stability derivatives.

There are two segregated movements in aircraft flight dynamics: longitudinal and lateral-directional. Their flight variables are shown respectively in equations (11).

$$\begin{aligned}
\Delta X, \Delta Z, \Delta M &= f(\Delta u, \Delta w, \Delta q, \Delta \dot{u}, \Delta \dot{w}, \Delta \dot{q}, \Delta \delta_e, \Delta \dot{\delta}_e) \\
\Delta Y, \Delta L, \Delta N &= f(\Delta v, \Delta p, \Delta r, \Delta \dot{v}, \Delta \dot{p}, \Delta \dot{q}, \Delta \delta_a, \Delta \dot{\delta}_a, \Delta \delta_r, \Delta \dot{\delta}_r)
\end{aligned} \tag{11}$$

The effect of longitudinal variables is neglected on the lateral-directional movement and vice-versa. Thus, longitudinal forces derivatives with respect to lateral variables do not appear on the equations and the same for lateral forces with respect to longitudinal variables. The dynamic equations are split into two groups. In addition, the derivatives with respect to accelerations are in general neglected but  $\Delta \dot{w}$  and control derivatives (see [17] and [16]).

Finally, the following derivatives (see 12) are usually small and neglected:

$$X_q, X_{\dot{w}}, X_{\delta_e}, Y_{\delta_a}, Y_{\dot{\delta}_a}, Y_{\dot{\delta}_r}, Z_{\dot{\delta}_e}, L_{\dot{\delta}_r}, N_{\dot{\delta}_a} \tag{12}$$

Finally, the remaining stability derivatives, (presented in the equation 13) are included in the aero-propulsive forces and moments.

$$\begin{aligned}
\Delta X &= X_u \Delta u + X_w \Delta w + X_{\delta_e} \Delta \delta_e \\
\Delta Y &= Y_v \Delta v + Y_p \Delta p + Y_r \Delta r + Y_{\delta_r} \Delta \delta_r \\
\Delta Z &= Z_u \Delta u + Z_w \Delta w + Z_q \Delta q + Z_{\dot{w}} \Delta \dot{w} + Z_{\delta_e} \Delta \delta_e \\
\Delta L &= L_v \Delta v + L_p \Delta p + L_r \Delta r + L_{\delta_a} \Delta \delta_a + L_{\dot{\delta}_a} \Delta \dot{\delta}_a + L_{\delta_r} \Delta \delta_r \\
\Delta M &= M_u \Delta u + M_w \Delta w + M_q \Delta q + M_{\dot{w}} \Delta \dot{w} + M_{\delta_e} \Delta \delta_e + M_{\dot{\delta}_e} \Delta \dot{\delta}_e \\
\Delta N &= N_v \Delta v + N_p \Delta p + N_r \Delta r + N_{\delta_a} \Delta \delta_a + N_{\dot{\delta}_a} \Delta \dot{\delta}_a + N_{\delta_r} \Delta \delta_r
\end{aligned} \tag{13}$$

In equation 13 there are also stability derivatives with respect to control surfaces  $(\delta_e, \delta_a, \delta_r, \delta_t)$ . In the case of flying wings, there is no rudder control  $(\delta_r)$ . The flying wing control surfaces can be seen in Figure 28.

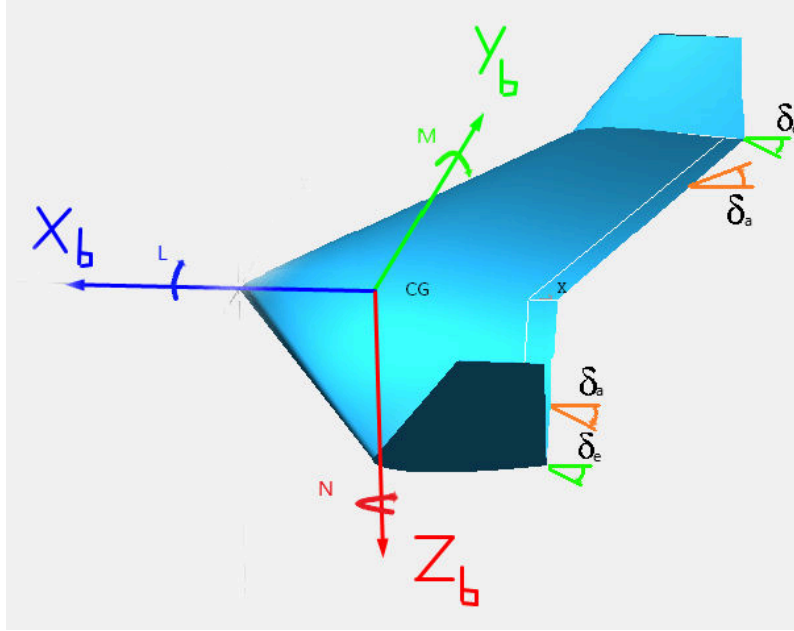


Figure 28: Control surfaces.

It is usual to use dimensionless notation because removing dimensions simplifies the analysis. The reference magnitudes are different for longitudinal and lateral equations (see figures 29 and 32). The adimensional forces are shown in the figure 30.

Dimensional Variable	Reference Magnitude	Dimensionless Variable
$X, Z$	$\frac{1}{2}\rho V^2 S$	$C_x = \frac{X}{\frac{1}{2}\rho V^2 S} \cdot C_z = \frac{Z}{\frac{1}{2}\rho V^2 S}$
$M$	$\frac{1}{2}\rho V^2 S c$	$C_m = \frac{M}{\frac{1}{2}\rho V^2 S c}$
$u, w$	$u_z$	$\hat{u} = \frac{u}{u_z}, \hat{w} = \frac{w}{u_z}$
$q$	$\frac{2u_z}{c}$	$\hat{q} = \frac{qc}{2u_z}$
$t$	$\frac{c}{2u_z}$	$\hat{t} = \frac{t2u_z}{c}$
$m$	$\rho S \frac{c}{2}$	$\mu = \frac{m}{\rho S c / 2}$
$I_y$	$\rho S \left(\frac{c}{2}\right)^3$	$\hat{I}_y = \frac{I_y}{\rho S (c/2)^3}$

Figure 29: Reference magnitudes, Source:[17]

	$X$	$Z$	$M$
$\frac{\partial}{\partial u}$	$\frac{\rho u_z S C_{x_z} + \frac{\rho u_z S}{2} C_{x\hat{u}}}{2}$	$\frac{\rho u_z S C_{z_z} + \frac{\rho u_z S}{2} C_{z\hat{u}}}{2}$	$\frac{\rho u_z S c}{2} C_{m\hat{u}}$
$\frac{\partial}{\partial w}$	$\frac{\rho u_z S}{2} C_{x\alpha}$	$\frac{\rho u_z S}{2} C_{z\alpha}$	$\frac{\rho u_z S c}{2} C_{m\alpha}$
$\frac{\partial}{\partial \dot{w}}$		$\frac{\rho S c}{4} C_{z\dot{\alpha}}$	$\frac{\rho S c^2}{4} C_{m\dot{\alpha}}$
$\frac{\partial}{\partial q}$		$\frac{\rho u_z S c}{4} C_{z\hat{q}}$	$\frac{\rho u_z S c^2}{4} C_{m\hat{q}}$
$\frac{\partial}{\partial \delta_e}$	$\frac{\rho u_z^2 S}{2} C_{x\delta_e}$	$\frac{\rho u_z^2 S}{2} C_{z\delta_e}$	$\frac{\rho u_z^2 S c}{2} C_{m\delta_e}$
$\frac{\partial}{\partial \dot{\delta}_e}$			$\frac{\rho u_z S c^2}{4} C_{m\dot{\delta}_e}$

Figure 30: Adimensional coefficients, Source:[17]

After replacing all the terms and removing dimensions the adimensional system of equations is obtained (equations 14 and 15):

$$\begin{aligned}
(2\mu D - C_{X\hat{u}} + 2C_{Zs} \tan \theta_s) \Delta \hat{u} - C_{X\alpha} \Delta \alpha - C_{Zs} \Delta \theta &= C_{X\delta_e} \Delta \delta_e \\
- (C_{Z\hat{u}} + 2C_{Zs}) \Delta \hat{u} + ((2\mu - C_{Z\hat{\alpha}}) D - C_{Z\alpha}) \Delta \alpha - ((2\mu + C_{Z\hat{q}}) D + C_{Zs} \tan \theta) \Delta \theta &= C_{Z\delta_e} \Delta \delta_e \\
- C_{m\hat{u}} \Delta \hat{u} - (C_{m\hat{\alpha}} D + C_{m\alpha}) \Delta \alpha + (\hat{I}_y D^2 - C_{m\hat{q}} D) \Delta \theta &= (C_{m\delta_e} D + C_{m\delta_e}) \Delta \delta_e \\
D \Delta \theta &= \Delta \hat{q}
\end{aligned} \tag{14}$$

$$\begin{aligned}
Z_s + mg \cos \theta_s = 0 &\rightarrow C_{Zs} = -\frac{mg \cos \theta_s}{1/2 \rho u_s^2 S} \\
X_s - mg \sin \theta_s = 0 &\rightarrow C_{Xs} = \frac{mg \sin \theta_s}{1/2 \rho u_s^2 S} = -C_{Zs} \tan \theta_s
\end{aligned} \tag{15}$$

The coordinate system used in equations 14 and 15 is a particular body coordinate system called stability axis (see Figure 31). These axis are useful for stability analysis because  $\gamma_s = \theta_s$  thus  $\alpha_s = 0$ .

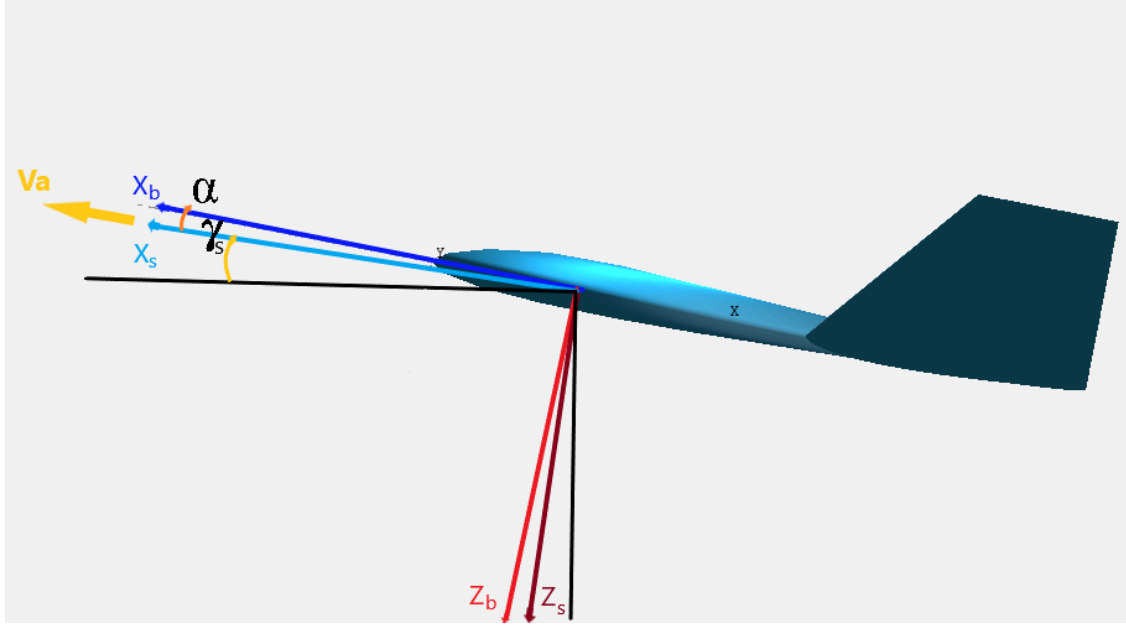


Figure 31: Stability axis

Now, moving to the lateral-directional movement, the convention magnitudes for dimensionless notation are shown in the figure 32. The adimensional forces are shown in 33.

Dimensional Variable	Reference Magnitude	Dimensionless Coefficient
$Y$	$\frac{1}{2} \rho V^2 S$	$C_Y = \frac{Y}{\frac{1}{2} \rho V^2 S}$
$L, N$	$\frac{1}{2} \rho V^2 S b$	$C_l = \frac{L}{\frac{1}{2} \rho V^2 S b}, C_n = \frac{N}{\frac{1}{2} \rho V^2 S b}$
$v$	$u_z$	$\hat{v} = \frac{v}{u_z} = \beta$
$p, r$	$\frac{2u_z}{b}$	$\hat{p} = \frac{pb}{2u_z}, \hat{r} = \frac{rb}{2u_z}$
$t$	$\frac{b}{2u_z}$	$\hat{t} = \frac{t2u_z}{b}$
$m$	$\rho S \frac{b}{2}$	$\mu = \frac{m}{\rho S b / 2}$
$I_x, I_z, J_{xz}$	$\rho S \left(\frac{b}{2}\right)^3$	$\hat{I}_x = \frac{I_x}{\rho S (b/2)^3}, \hat{I}_z = \frac{I_z}{\rho S (b/2)^3}, \hat{J}_{xz} = \frac{J_{xz}}{\rho S (b/2)^3}$

Figure 32: Reference magnitudes, Source:[17]

	$Y$	$L$	$N$
$\frac{\partial}{\partial v}$	$\frac{\rho u_z S}{2} C_{Y\beta}$	$\frac{\rho u_z S b}{2} C_{l\beta}$	$\frac{\rho u_z S b}{2} C_{n\beta}$
$\frac{\partial}{\partial p}$	$\frac{\rho u_z S b}{4} C_{Y\hat{p}}$	$\frac{\rho u_z S b^2}{4} C_{l\hat{p}}$	$\frac{\rho u_z S b^2}{4} C_{n\hat{p}}$
$\frac{\partial}{\partial r}$	$\frac{\rho u_z S b}{4} C_{Y\hat{r}}$	$\frac{\rho u_z S b^2}{4} C_{l\hat{r}}$	$\frac{\rho u_z S b^2}{4} C_{n\hat{r}}$
$\frac{\partial}{\partial \delta_a}$		$\frac{\rho u_z^2 S b}{2} C_{l\delta_a}$	$\frac{\rho u_z^2 S b}{2} C_{n\delta_a}$
$\frac{\partial}{\partial \delta_a}$		$\frac{\rho u_z^2 S b^2}{4} C_{l\delta_a}$	
$\frac{\partial}{\partial \delta_r}$	$\frac{\rho u_z^2 S}{2} C_{Y\delta_r}$	$\frac{\rho u_z^2 S b}{2} C_{l\delta_r}$	$\frac{\rho u_z^2 S b}{2} C_{n\delta_r}$
$\frac{\partial}{\partial \delta_r}$			$\frac{\rho u_z^2 S b^2}{4} C_{n\delta_r}$

Figure 33: Adimensional coefficients, Source:[17]

The adimensional system of equations for the lateral movement is described in the equation 16.

$$\begin{aligned}
(2\mu D - C_{Y\beta})\Delta\beta - C_{Y\hat{p}}\Delta\hat{p} + (2\mu - C_{Y\hat{r}})\Delta\hat{r} + C_{Zs}\Delta\phi &= C_{Y\delta_r}\Delta\delta_r \\
- C_{l\beta}\Delta\beta + (\hat{I}_x D - C_{l\hat{p}})\Delta\hat{p} - (\hat{J}_{xz} D + C_{l\hat{r}})\Delta\hat{r} &= (C_{l\delta_a} D + C_{l\delta_a})\Delta\delta_a + C_{l\delta_r}\Delta\delta_r \\
- C_{n\beta}\Delta\beta - (\hat{J}_{xz} D + C_{n\hat{p}})\Delta\hat{p} + (\hat{I}_z D - C_{n\hat{r}})\Delta\hat{r} &= C_{n\delta_a}\Delta\delta_a + (C_{n\delta_r} D + C_{n\delta_r})\Delta\delta_r \quad (16) \\
D\Delta\phi &= \Delta\hat{p} + \tan\theta_s\Delta\hat{r} \\
D\Delta\psi &= \sec\theta_s\Delta\hat{r}
\end{aligned}$$

### 3.4 Equations, implementation & testing

The equations are programmed in *MATLAB*. To validate, the data of two aircraft are used. Eigenvalues and the system's response are compared with [17].

In the first test, data from a subsonic airplane at the cruise phase is used. The results are compared with Ref [17]. The code works with no mistakes because the eigenvalues obtained are almost equal, as can be seen in tables 4 and 5.

		Mode 1 (Phugoid)	Mode 2 (Short Period)
Eigenvalues	Ref [17]	$\lambda_{1,2}(s^{-1}) = -0.00288 \pm 0.0519i$	$\lambda_{3,4}(s^{-1}) = -1.107 \pm 1.443i$
	<i>MATLAB</i>	$\lambda_{1,2}(s^{-1}) = -0.0029 \pm 0.0518i$	$\lambda_{3,4}(s^{-1}) = -1.109 \pm 1.445i$
Eigenvectors	Ref [17]	$\frac{\hat{u}_1}{\theta_1} = 0.841$ $\frac{\alpha_1}{\theta_1} = 0.0256$ $\phi_{\hat{u}_1} = 94.9$ $\phi_{\alpha_1} = -85.4$	$\frac{\hat{u}_3}{\theta_3} = 0.012$ $\frac{\alpha_3}{\theta_3} = 1.24$ $\phi_{\hat{u}_3} = 12.8$ $\phi_{\alpha_3} = 27.6$
	<i>MATLAB</i>	$\frac{\hat{u}_1}{\theta_1} = 0.842$ $\frac{\alpha_1}{\theta_1} = 0.0256$ $\phi_{\hat{u}_1} = 94.9$ $\phi_{\alpha_1} = -84.5$	$\frac{\hat{u}_3}{\theta_3} = 0.012$ $\frac{\alpha_3}{\theta_3} = 1.24$ $\phi_{\hat{u}_3} = 12.6$ $\phi_{\alpha_3} = 27.7$

Table 4: Comparison of Longitudinal Modes

		Mode 1 (Roll Mode)	Mode 2 (Spiral Mode)	Mode 3 (Dutch Roll)
Eigenvalues	Ref [17]	$\lambda_1(s^{-1}) = -1.601$	$\lambda_2(s^{-1}) = -0.006508$	$\lambda_{3,4}(s^{-1}) = -0.09823 \pm 0.9266i$
	<i>MATLAB</i>	$\lambda_1(s^{-1}) = -1.5933$	$\lambda_2(s^{-1}) = -0.0066$	$\lambda_{3,4}(s^{-1}) = -0.1010 \pm 0.9284i$
Eigenvectors	Ref [17]	$\frac{\beta_1}{\phi_1} = -0.0017$ $\frac{\hat{r}_1}{\phi_1} = 0.0036$ $\phi_\beta = 0$ $\phi_{\hat{r}_1} = 0$	$\frac{\beta_1}{\phi_1} = 0.0091$ $\frac{\hat{r}_1}{\phi_1} = 0.0032$ $\phi_\beta = 0$ $\phi_{\hat{r}_1} = 0$	$\frac{\beta_1}{\phi_1} = 0.681$ $\frac{\hat{r}_1}{\phi_1} = 0.0479$ $\phi_\beta = -58.5$ $\phi_{\hat{r}_1} = -135.3$
	<i>MATLAB</i>	$\frac{\beta_1}{\phi_1} = -0.0017$ $\frac{\hat{r}_1}{\phi_1} = 0.0034$ $\phi_\beta = 0$ $\phi_{\hat{r}_1} = 0$	$\frac{\beta_1}{\phi_1} = 0.0092$ $\frac{\hat{r}_1}{\phi_1} = 0.0032$ $\phi_\beta = 0$ $\phi_{\hat{r}_1} = 0$	$\frac{\beta_1}{\phi_1} = 0.675$ $\frac{\hat{r}_1}{\phi_1} = 0.0438$ $\phi_\beta = -57.6$ $\phi_{\hat{r}_1} = -140.6$

Table 5: Comparison of Lateral Modes

Furthermore, another test is made comparing the stability derivatives of the selected flying wing prototype (without winglets), see figure 34.

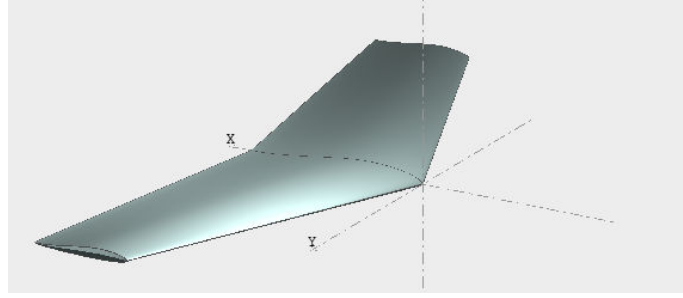


Figure 34: Prototype simulated in *XFRL5*.

The eigenvalues and eigenvectors, in this case, are also very similar. In the figures (35 and 36), the aircraft response is compared between *MATLAB* and *XFRL5*.

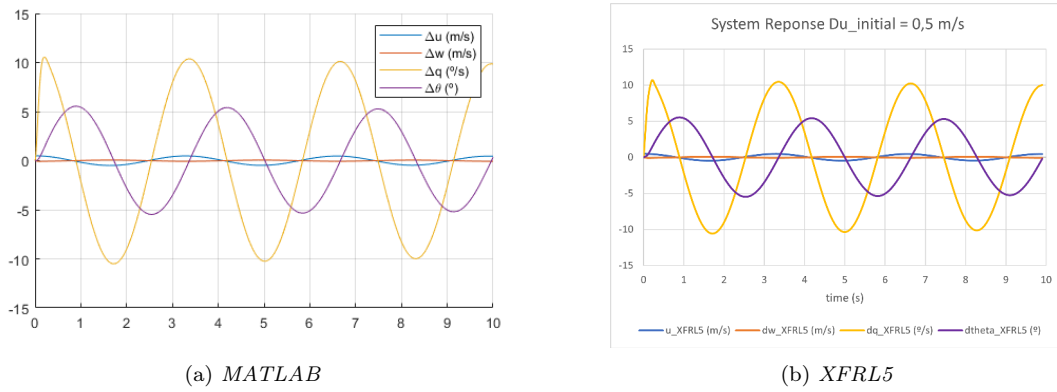


Figure 35: Longitudinal response comparison for  $\Delta u = 0.5(m/s)$  perturbation

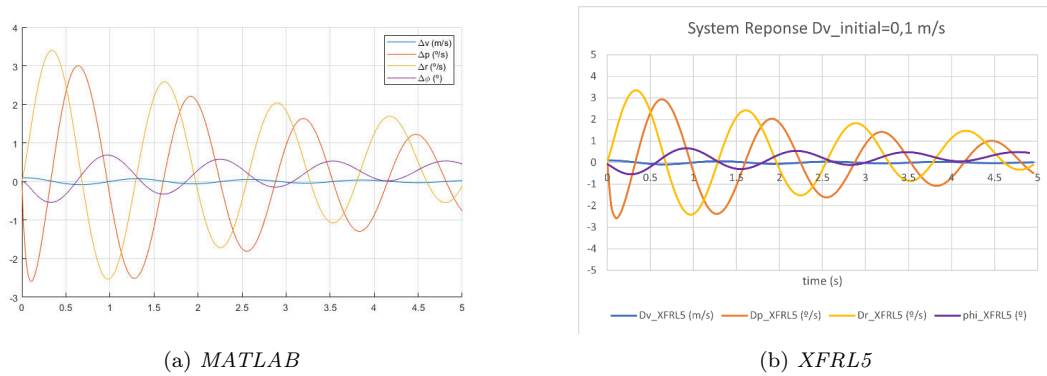


Figure 36: Lateral-directional response comparison for  $\Delta v = 0.1(m/s)$  perturbation

The code is considered to be free of mistakes and everything is ready to be used in the linear control implementation.

### 3.5 Modal analysis and modifications impact

In this section, the stability properties of the final versions of the prototype will be compared with other similar flying wings.

Model	Phugoid	Short Period	Dutch Roll	Roll	Spiral
CP50-V0	$-0.032 \pm 1.34i$	$-17.33 \pm 22.51$	$-0.445 \pm 5.73i$	$-23.77 \pm 0i$	$+0.084 \pm 0i$
[4]	$-0.03 \pm 0.38i$	$-27.6 \pm 58i$	$-0.6 \pm 8.2$	$-41 \pm 0i$	unstable
[11]	$-0.029 \pm 1.02i$	$-19.78 \pm 17.385i$	$-0.327 \pm 3.61i$	$-27.500 \pm 0i$	$+0.065 \pm 0i$

Table 6: Dynamic modes comparison with other works

Table 6 shows that the dynamic modes are very similar in the three models (Figures 37,38 and 39). The analysis suggests that the weight, inertia, wing shape, and wing dimensions are properly balanced compared to similar flying wings in its category. In general, the dynamic behavior is good, only the spiral mode is divergent but indeed it is usually unstable. The flight properties of the prototype are detailed in 3.6.



Figure 37: CP50-V0



Figure 38: [4]

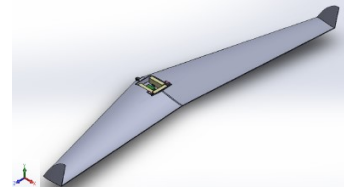


Figure 39: [11]

To close this section a comparison is done in XFRL5 with and without winglets (figures 41 and 40). The idea is to check and quantify the effects of winglets on lateral stability.

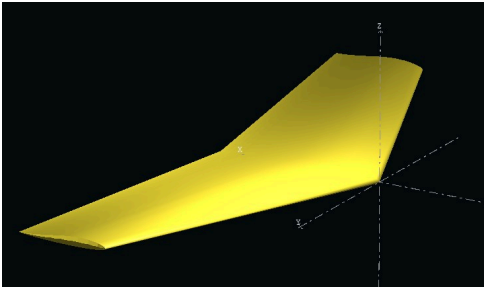


Figure 40: CP50-V0 without winglets.

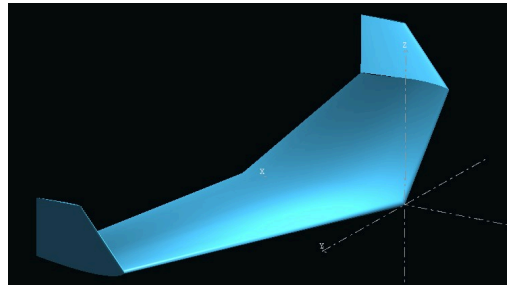


Figure 41: CP50-V0 with winglets.

Model	Phugoid	Short Period	Dutch Roll	Roll	Spiral
No Winglets	$-0.038 \pm 1.11i$	$-20.777 \pm 27.47i$	$+0.013 \pm 3.62i$	$-31.352 \pm 0i$	$+0.102 \pm 0i$
Winglets	$-0.032 \pm 1.34i$	$-17.33 \pm 22.51$	$-0.445 \pm 5.73i$	$-23.77 \pm 0i$	$+0.084 \pm 0i$

Table 7: Dynamic modes comparison

In Table 7, large differences can be observed regarding the lateral modes. Firstly, and



most importantly, the Dutch Roll mode is unstable in absence of winglets and its period is longer. Secondly, the spiral mode is more unstable as well. Longitudinal modes seem to be more damped without winglets.

Lateral stability greatly improves with winglets, the Dutch Roll mode becomes stable and correctly damped, also its frequency increases. The spiral mode improves as well but remains unstable. In conclusion, winglets are mandatory to assure minimum requirements in terms of lateral stability.

### 3.6 Flight qualities of CP50-V0

Finally, the dynamic response of the prototype is evaluated according to MIL-STD-1797A rules for flight quality evaluation. From table 6, modal natural frequencies and damping are calculated and presented in table 8. The rules can be easily found on the internet, however, a synopsis can be found in [17].

Mode	$\omega_n$ (rad/s)	$\xi$	time to double $t_2$ (s)
Phugoid	1.34	0.024	-
Short Period	28.41	0.610	-
Dutch Roll	5.75	0.077	-
Spiral	-	-	8.25

Table 8: Modal properties CP50-V0 (winglets)

In the rules, four aircraft categories are defined, in this case, the small UAV may fit in the first one, *CLASS I*, small light aircraft. However, this category refers to aircraft such as *Cessna* not to small UAVs. In addition, the flight requirements also influence the evaluation, the *CAT B* flight (Non-terminal flight phases with gradual maneuvers which do not need high accuracy tracking) will be used.

Finally, depending on the evaluated flight properties, three levels are defined:

- Level 1: Suitable flight capabilities for the mission.
- Level 2: Suitable flight capabilities but there is an increase in pilot or control system activity or exists a degradation in mission effectiveness.
- Level 3: The aircraft can be controlled safely but excessive pilot or control system activity is needed or there is severe degradation in mission efficiency.

According to the rules, the prototype CP50-V0 meets level 2 because its  $\xi_{phugoid} > 0$ .

In addition, the prototype CP50-V0 meets level 1 because  $\xi_{shortperiod} > 0.30$ .

Regarding Dutch Roll mode, prototype CP50-V0 meets level 2 because  $0.02 < \xi_{dutchroll} < 0.08$ ,  $\xi_{dutchroll}\omega_{n(dutchroll)} > 0.15$  and  $\omega_{n(dutchroll)} > 0.4$ . Finally, for the spiral mode the prototype CP50-V0 meets the minimum requirements, Level 3.

In conclusion, regarding MIL-STD-1797A rules, the prototype flight properties are good except for the spiral mode, which must be improved.

### 3.7 Spiral mode improvement

The easiest way to improve spiral mode is to increase cross-wind surface and stability derivatives with respect to  $\beta$ . To enlarge the cross-wind section,  $5^\circ$  dihedral angle is added. The effects of dihedral are: to move  $z_{cg}$  up, increase off-diagonal inertia term  $J_{xz}$ , increase cross-wind section, and thus,  $\beta$  stability derivatives.

Model	Phugoid	Short Period	Dutch Roll	Roll	Spiral
$0^\circ$ dihedral	$-0.032 \pm 1.34i$	$-17.33 \pm 22.51i$	$-0.445 \pm 5.73i$	$-23.77 \pm 0i$	$+0.084 \pm 0i$
$5^\circ$ dihedral	$-0.033 \pm 1.31i$	$-17.487 \pm 23.32i$	$-0.304 \pm 6.06i$	$-25.037 \pm 0i$	$+0.039 \pm 0i$

Table 9: Dynamic modes comparison

As can be seen in table 9 dihedral improves all modes except Dutch Roll, whose damping diminishes, nevertheless, the spiral mode divergent behavior is improved. The new  $\xi_{dutchroll} = 0.05$  thus, the Dutch Roll evaluation is still Level 2 while the Spiral mode parameter "time to double" increases,  $T_2 = 17.77s$  which meets requirements for Level 2.

## 4 Prototype manufacturing

This chapter describes the process to build the prototype CP50-V0. The Details about the materials, components, and mass properties are given hereafter.

### 4.1 Components

The technical specifications of the components are found on the internet and shown below. The component mass is relevant to ensure good stability properties to control the distance between the aerodynamic center and the center of gravity.

- Battery: GENS ACE 450mAh 7.4V, 32 g.
- Servo: TURNIGY TG9 Micro Servo 1.5kg, 0.10sec, 10.1g.
- Receiver: FrSky X8R 8/16Ch S.Bus ACCST, 16.8g.
- ESC: 3D robotics 20 A, 5V BEC, 31g.
- Engine: Turnigy 2822/14 1400kV, 50g.

### 4.2 Manufacturing process

Firstly, the wing shape is built. The wing is made of Styrofoam (XPS) (rigid high-density foam, usually blue colored and used for thermal isolation). Each semi-wing is manufactured separately and then, glued together. To build the semi-wing with the correct airfoil shape, wood templates are used. The templates have the shape of the Eppler168 airfoil, but different sizes, the bigger one is for the root airfoil while the other one is for the tip airfoil. The root chord is 275mm and tip chord is 150mm which gives a taper ratio of 1.83. The tip airfoil is offset 200mm from the nose of the aircraft so the sweep angle is  $19.56^\circ$ . Neither twist nor dihedral is given to the semi-wings.

The pieces of Styrofoam are more or less 1000 x 500 x 100mm, these blocks are cut to the semi-wingspan distance which is 475mm. Then the airfoil template's center line is placed in the middle of the foam block's thickness, and the tip template is correctly offset and then fixed. Subsequently, the semi-wing shape is obtained by hot-wire cutting, following the template's profile. For this step, two persons are needed.

Figures 42 and 43 show the first cuttings, multiple attempts until good results are obtained.. In these figures, the wood templates can be seen. It needs some practice and coordination to correctly follow the template's shape so wiggles in the final surface are minimized. The wiggles can be seen in figure 42.

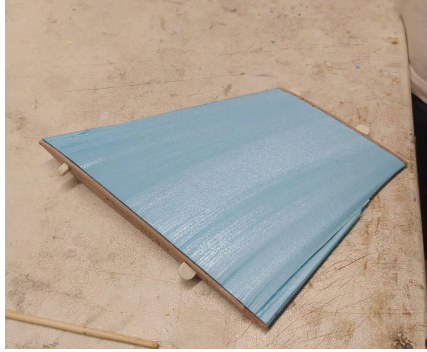


Figure 42: Scrap piece used to test



Figure 43: First attempt

Secondly, The wing's trailing edge is cut to detach the elevons of the semi-wings. Subsequently, the electronics bay is cut out using a cutter and then both semi-wings are glued with a plastic gun. After that, the holes for the servos are made by melting the foam with the heat of a welder for electronics. The next step is to attach the elevons to the semi-wings with two plastic hinges each. Once the elevons are placed, a bracket for the actuators is glued to each elevon to connect both parts and transmit the servo movement. Additionally, a plastic-glued wood spar is inserted to increase the stiffness of the wing. Some wing areas are covered with plastic tape to protect them and make the surface smoother. Additionally, a Velcro stripe is placed in the electronics bay to fix the components (see figure 44). Once the airframe is built, the electronic components are placed in the bay and covered. Finally, the winglets are cut from other foam blocks using a cutter, after that, the winglet's surface is sanded with sandpaper and finally, the winglets are plastic-glued to the wind tip airfoils. Figure 45 shows the final configuration of the prototype.

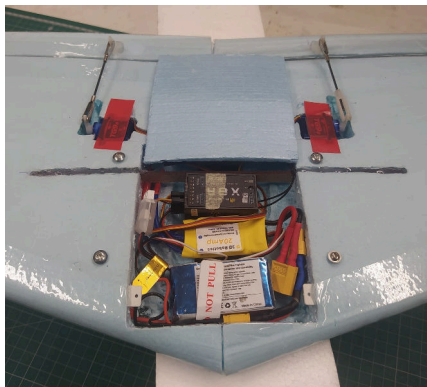


Figure 44: Detail of electronics bay

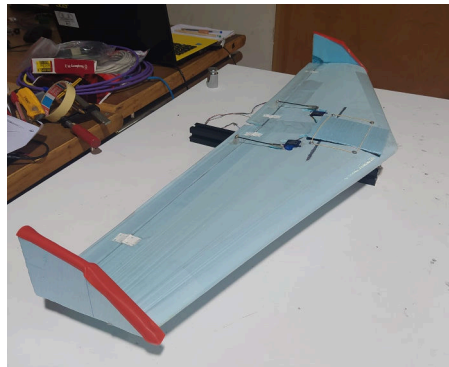


Figure 45: Completed prototype

Due to lack of time, it was not possible to mount the engine, to imitate the effect in regard to the dynamic experiments, a weight with the same mass as the engine is attached under the nose of the prototype. The weight can be seen in figure 66.

### 4.3 Center of gravity estimation

The center of gravity tests are conducted following the João's work [12], the equipment used is the same one. The test device consists of two load cells mounted over an aluminum beam, see figure 46. The load cells are connected to an Arduino that calculates the mass over each load cell after being calibrated with a 200g mass.

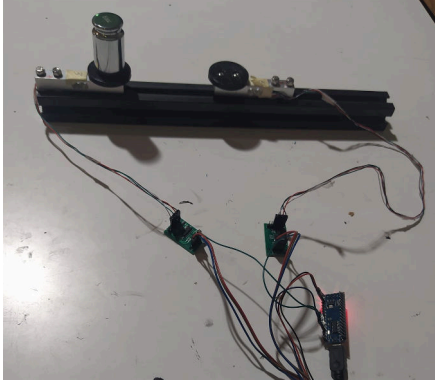


Figure 46: Test cell assembly

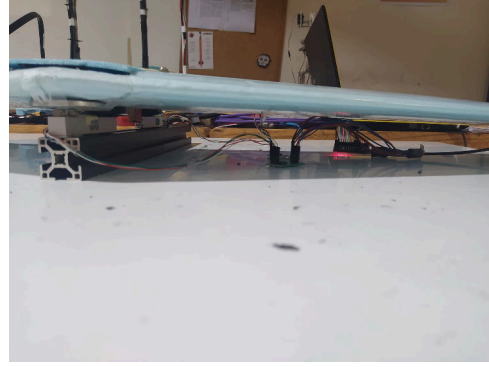


Figure 47: Prototype over the test cell

In figure 47 it can be seen model is ready to be tested. The steps to estimate the center of gravity longitudinal position ( $X_{cg}$ ) are:

1. The device is connected to the laptop via USB.
2. The communication with the *Arduino* is established using the software *Putty*.
3. After establishing communication, a script arises and guides the calibration process.
4. After calibration the prototype's symmetry axis is placed along the line created by the two load cells in a position where the model is correctly supported over the two cells.
5. The distances from the nose and the first load cell and between load cells are obtained.
6. The mass lectures of each cell are taken.
7. The formula is applied and  $X_{cg}$  is obtained.

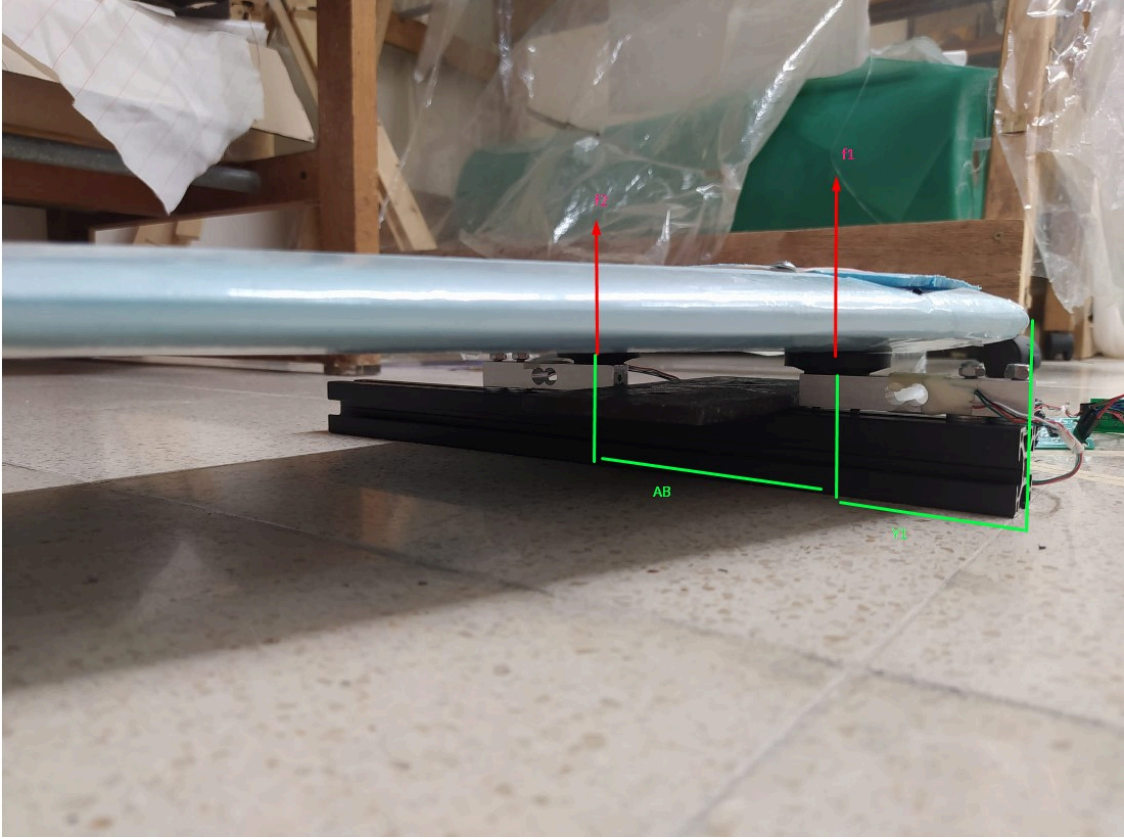


Figure 48: Center of gravity test distances

$$X_{CG} = \frac{F2(Y1 + AB) + F1(Y1)}{F1 + F2} \quad (17)$$

The test is carried out multiple times moving back and forward the prototype. The distances can be seen in Figure 48. "F1" and "F2" are the mass lectures of load cells 1 and 2. "Y1" is the distance between the prototype's nose and load cell 1. "A" is the distance between the two load cells.

F1 (g)	F2 (g)	Y1(mm)	A(mm)	$X_{CG}$ (mm)
266	63	91	112	112
251	84	86	112	114
298	35	99.5	112	111
250	84	85	112	113
278	58	94	112	113
143	190	51	112	115

Table 10: Center of gravity test results

The  $X_{CG}$  position is estimated at 113mm, the results in table 10 are with winglets

and nose balance weight for dynamic experiments. Tests are also done for  $Y_{CG}$ , and as expected the prototype is correctly balanced.

The total mass of the model is 333.8(g) calculated from the experiment.

#### 4.4 Inertia moment estimation

To correctly simulate UAV dynamics it is important to estimate inertia moments. First, an experiment is conducted. The UAV is placed over a metallic frame that is hanging from two ropes like a pendulum. Then, the setup is perturbed to induce oscillations. Measuring the period of oscillation with and without placing the UAV and after some mathematical operations, the inertia momentum is calculated. For more details see [12].



Figure 49: Inertia test assembly



Figure 50: Model placed for testing

However, due to the small weight of the UAV and the big difference in weight with the metallic structure, there is not enough precision to notice any change in the period of oscillations.

Provided that measuring the inertia moments with the tools available in the laboratory is not possible, the estimation of  $XFRL5$  will be considered valid. However, it is not possible to include the inertia of the electronic components in  $XFRL5$  so finally, the software *CATIA* is used to estimate the mass properties.



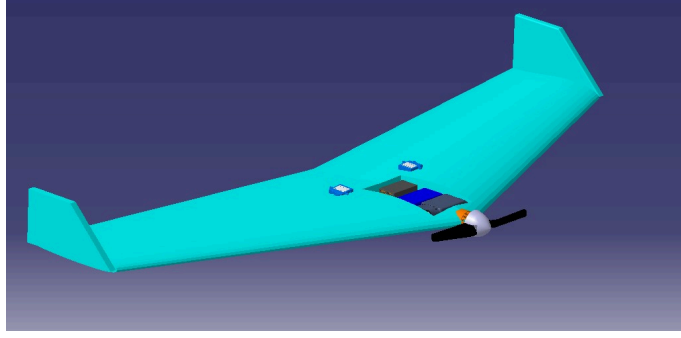


Figure 51: CP50-V0 prototype modeled in *CATIA*

The wing geometry is drafted in *CATIA* (see Figure 51), and the main electronic components are taken from open source CAD repositories or created. The mass properties of each component are measured in the laboratory and then included in *CATIA*.

Component	Mass (g)
Wing	137
Receiver	17
ESC	31
Battery	32
Servo	12
Engine + Prop	63
Total	306

Table 11: Mass component properties

mass	306 g
$x_{cg}$	120 mm
$y_{cg}$	0 mm
$z_{cg}$	4,2 mm
$I_{xx}$	0.009 kgm <sup>2</sup>
$I_{yy}$	0.002 kgm <sup>2</sup>
$I_{zz}$	0.012 kgm <sup>2</sup>
$I_{xz}$	3e-5 kgm <sup>2</sup>

Table 12: *CATIA* estimation

The estimated weight and  $x_{cg}$  in *CATIA* are different from the measured in the laboratory because there are many details that are not worthy to model in *CATIA*. The inertia momentums estimated by *CATIA* are used in *XFRL5* and Simulink to obtain the dynamic properties.

The mass of each component is shown in table 11, the estimations made by *CATIA* are presented in table 12. The majority of the prototype's inertia momentum is given by the wing, as foam density is very homogeneous, the estimations are accurate. The principal source of error is that the electronic components are supposed to be homogeneous in terms of density but they are not. However, the discrepancies are small because the contribution of these components to the total is two orders of magnitude less.



## 5 Wind tunnel experiments

### 5.1 Static experiment description

The model is completely fixed to the test cell. One load cell measures the vertical force, a second one measures pitch torque, and finally, a third one measures drag. Using the lift force data recorded,  $L(\alpha)$  is obtained. The airspeed and air conditions are also measured to calculate the lift coefficient. The same procedure is done for pitch moment coefficient,  $Cm(\alpha)$  and drag coefficient  $C_D(\alpha)$ .

$C_L(\alpha)$  is used together with  $Cm(\alpha)$  to calculate the trim conditions for the flight envelope. So it is important to cover the full range of possible angles of attack including the stall region. It is also relevant to cover a range of airspeeds inside the flight envelope, mainly because for low-speed UAVs, the aerodynamic properties strongly vary with Reynolds's number (see [5]).

### 5.2 Static experiment implementation

As can be seen in Figure 52, the test cell can measure lift (red), drag (blue), and torque (green). Unfortunately, the torque and drag measure direction are the same because the test cell was designed to test engines. To overcome this issue, the coupling with the UAV model is designed to fit in two positions: in the first one, the model is aligned with drag measure direction; while in the other one the UAV is placed perpendicular to be able to record pitch momentum.

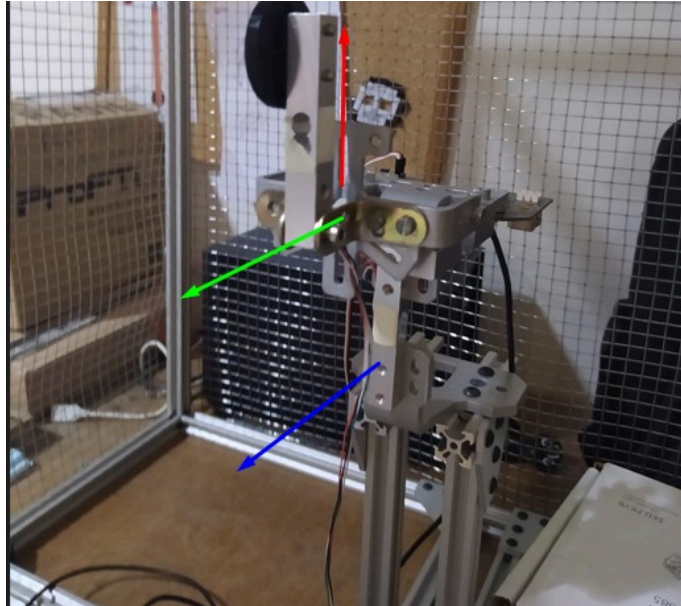


Figure 52: Test cell with the direction of force (lift in red and drag in blue) and torque (green) measures.

Previously, the test cell is calibrated following the manufacturer's instructions.

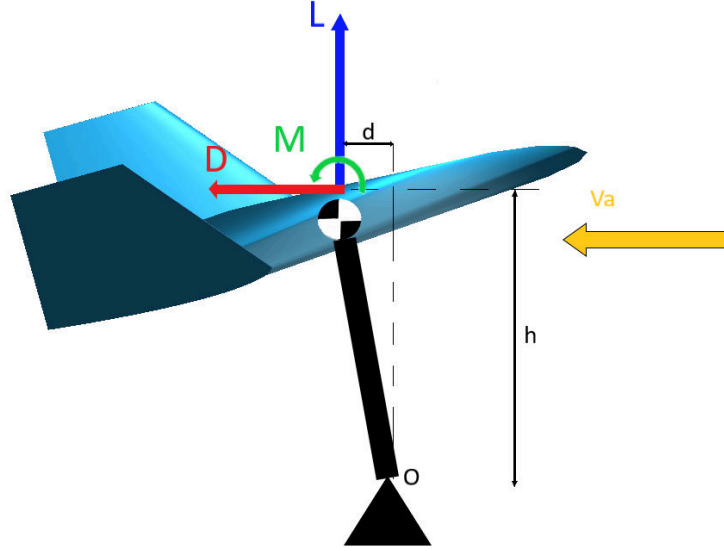


Figure 53: Wind tunnel static experiments force diagram.

The torque measure point is located at the bottom so according to the force configuration (depicted in Figure 53):

$$M_{measured} = M_{ac} - Ld + Dh \quad (18)$$

Since the torque measure point is not located aligned with the Y body axis Lift and Drag perturb the measurement.

The airspeed used in the experiments are 6.99, 8.00, 9.01, and 10.01 m/s. To achieve these airspeeds, the wind tunnel rpm parameter is set up according to the calibrated values (see table 13).

Airspeed	Display RPM
6.99	158
8.00	180
9.01	202
10.01	222

Table 13: Wind tunnel setup relations.

The angle of attack varies from 0 to 10 degrees in steps of 2 degrees. Due to severe

shaking near the stall region, caused by a lack of stiffness of the assembly, the upper limit is set at 10 degrees, below the stall point. To change the angle of attack without stopping the experiment a servo motor is used and attached to the prototype. In addition, an IMU sensor provides the pitch measure to adjust the angle of attack properly by commanding the servo.

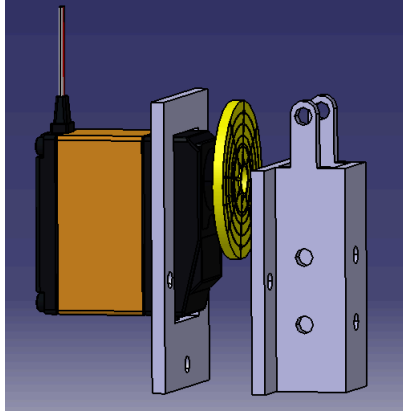


Figure 54: Assembly parts and servo

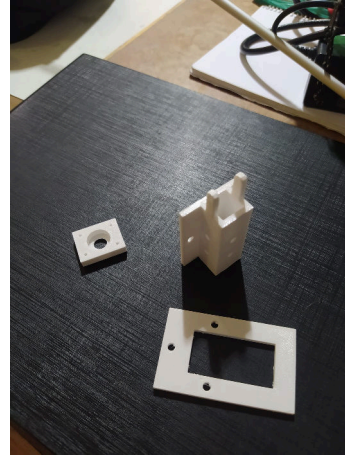


Figure 55: 3D printed parts

The parts in Figure 54 are designed in CATIA and 3D printed (figure 55). The servo fits in the plastic plate and it is tight with two screws. Likewise, the plate with the servo mounted on is fixed to the prismatic part by three bolts. Finally, the assembly fits on the top of the test cell and is secured with one bolt.

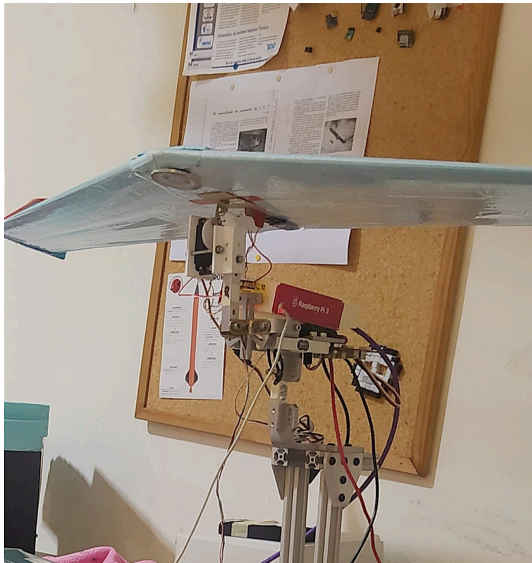


Figure 56: Static experiment configuration.



Figure 57: Model ready to be tested.

After the final assembly is completed (figure 56) the following steps are taken to perform the static wind tunnel tests (57):

1. Calibrate IMU and load cells
2. Place the model in 0 degrees of AoA.
3. Tare load cells.
4. Start the wind tunnel and set the correct airspeed.
5. Tare IMU to read 0 degrees of AoA.
6. Start recording data and increase 2 degrees the angle of attack every 30 seconds (it is not possible to reduce the step size because of the accuracy of the measures).

### 5.3 Static experiment results

In this section, the post-processed measurements are compared with *XFRL5*. The air conditions are obtained from the weather station inside the Humberto Delgado's Airport.

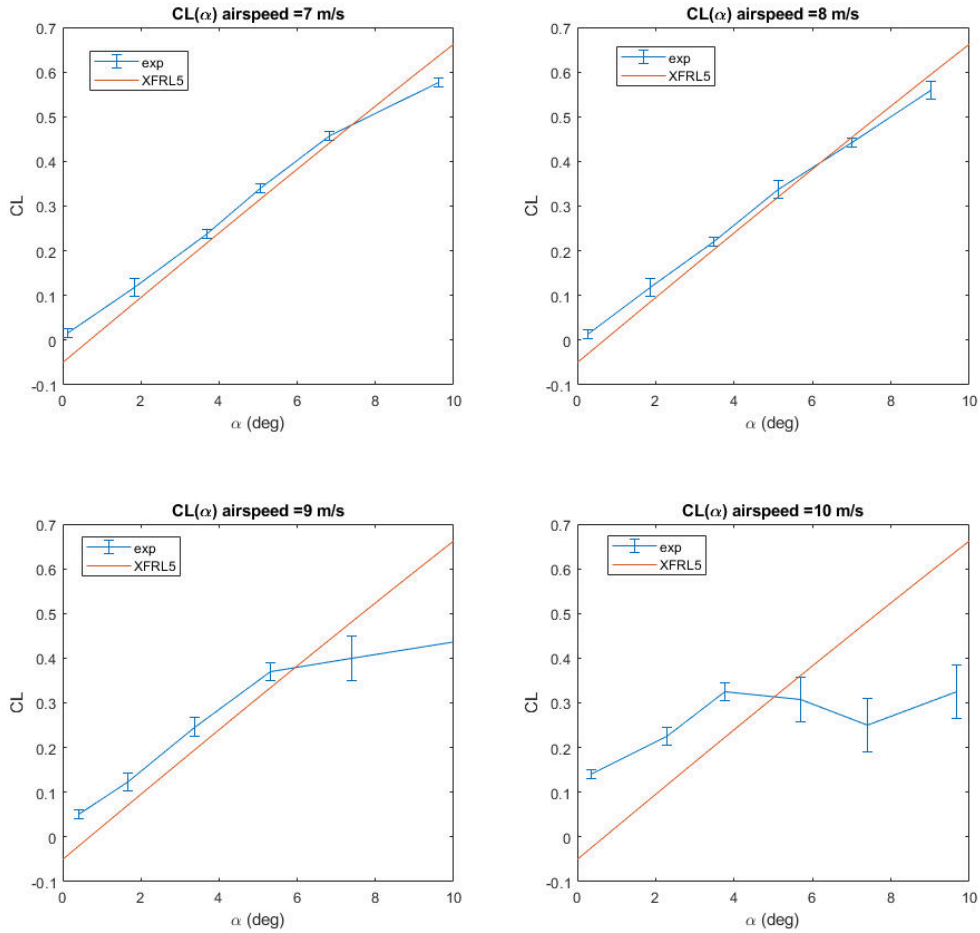


Figure 58: Experimental data and *XFRL5* estimations.

Regarding the lift coefficient, depicted in figure 58, the *XFLR5*'s estimation is really good for the airspeeds of 7 and 8 m/s. *XFLR5* underestimates the lift coefficient at low AoA, however, it overestimates the lift coefficient slope. Unlike *XFLR5*, the experiment results indicate positive  $CL_0$ . The most probable reason is manufacturing inaccuracies. In *XFLR5*, the elevon position is perfectly neutral, however, in the real model, the position is not perfectly neutral. If the position is slightly positive (down) of the trim position of elevators leads to positive  $CL_0$ . Another source of inaccuracy is the IMU, which has a certain bias error in AoA, that may cause the lift curve to move horizontally, varying  $CL_0$ . Another issue is that the model AoA slightly changes from the calibrated position when the forces over the assembly increase after starting the wind tunnel. Beforehand, this AoA increase is small, because the servo counteracts the forces holding the model in the initial position. As the IMU is tared with the wind tunnel in steady state, the AoA scale origin ( $0^\circ$ ) moves the lift curve left or right.

Regarding the experiments for the airspeeds of 9 and 10 m/s, the experimental results are not as expected and cannot be used to perform a critical analysis. At higher airspeed, the assembly tends to vibrate because of its poor stiffness, these vibrations are probably the cause of erroneous data. It is also possible that the vibrations induce partial stalls.

Airspeed	Experimental $CL_\alpha$	<i>XFLR5</i> $CL_\alpha$
7 m/s	3.49	4.11
8 m/s	3.58	4.11

Table 14: Lift slope estimation.

It is known that the Prandtl lifting-line theory (see [18]) estimates a linear dependency of Lift with AoA. As *XFLR5* uses this theory to calculate lift, the estimated lift curve is linear with AoA, which in fact can be observed in the real behavior of wings except in the stall region.

*XFLR5* lift slope estimation is close to the real value, in terms of lift forces, *XFLR5* is sufficiently accurate. Regarding the experimental values, the force data is taken every two degrees of AoA (0, 2, 4, 6, 8, 10) degrees. The lift, torque, and drag forces are recorded during 30s at each AoA. After that, the data is averaged and presented in these graphs (58 and 59). The error bar shows the standard deviation in the measures to quantify the uncertainties. The estimation of  $CL_\alpha$  can be improved using more points, the small difference between 7 and 8 m/s is mainly caused by the experiment inaccuracy, the mid value is considered a good estimation.

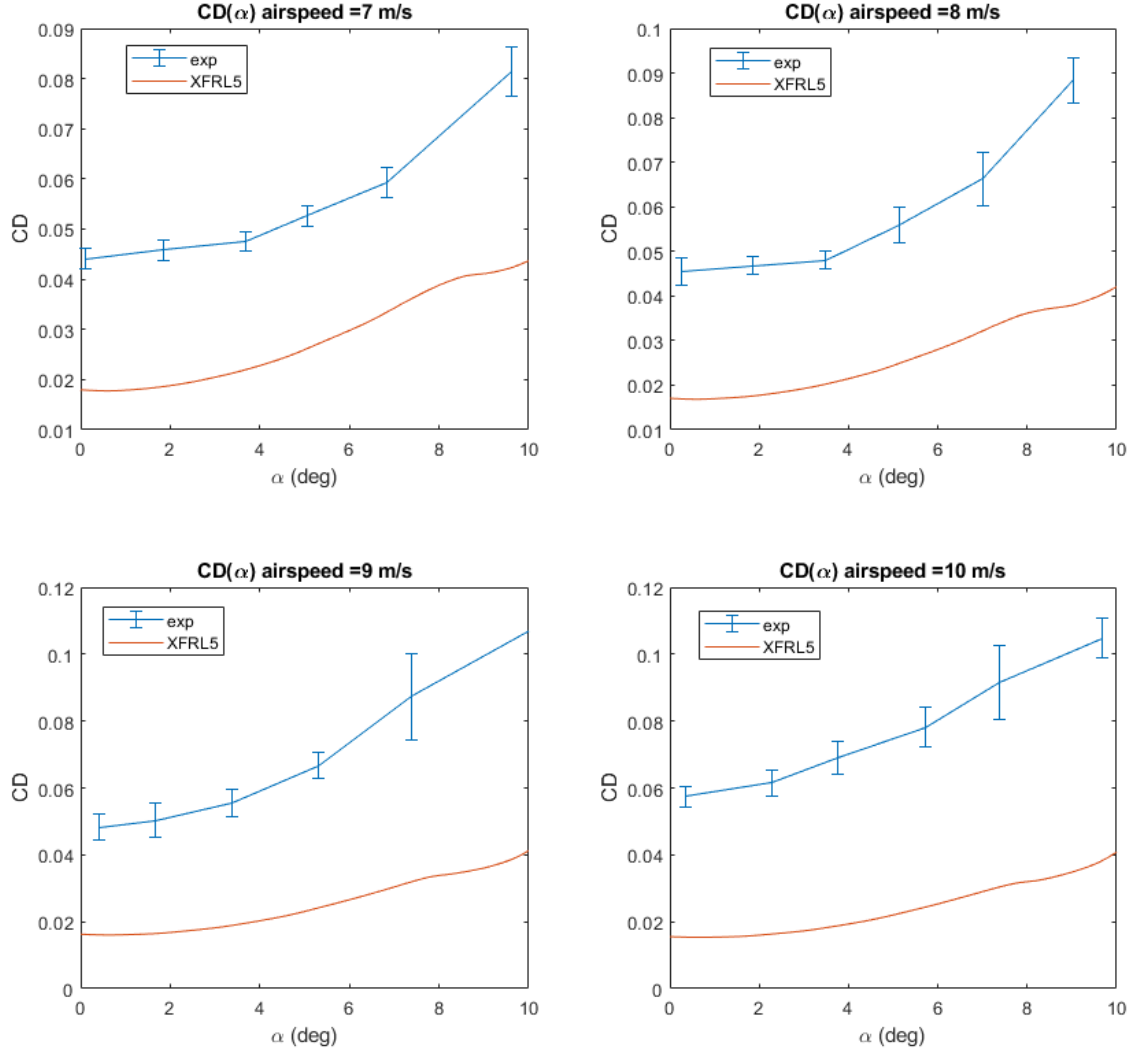


Figure 59: Experimental data and *XFLR5* estimations.

In figure 59 it can be seen that *XFLR5* underestimates drag. Real drag doubles *XFLR5* prediction. *XFLR5* interpolates the 2D drag calculated with XFOIL to the 3D case, this drastic approximation leads to underestimation of the drag force. However, the order of magnitude and the behavior with AoA are correctly predicted by *XFLR5*.

When airspeed changes, especially at low speeds, Reynolds number variations greatly affect boundary layer physics thus, the drag coefficient changes under these conditions, [5].

The pitch momentum estimation could not be done due to several reasons. First of all, the fact that the reference point is not aligned with the Y body axis makes the measurement difficult because drag and lift forces contribute. The perturbations can be removed, but the error increases. In addition, the exact momentum's arm of these forces (see table

15) is difficult to calculate with accuracy, enlarging the error. Last but not least, the perturbations generated by lift and drag are in the same order of magnitude as the pitch momentum, so the influence is strong.

Arm	magnitude (mm)
d	33
h	155

Table 15: Approximated arm distances.

The variable to estimate is  $Cm_{ac}$  (pitch momentum coefficient at the aerodynamic center). Thus, arm distances are measured between the torque cell and the aerodynamic center of the plane which is also unknown but XFLR5 estimates it at 145mm far from the leading edge. The joint between the plane and the servo is placed at the center of gravity, 112 mm far from the leading edge, according to the determination of the center of gravity. Despite these values are constant, AoA changes slightly modifying the distances.

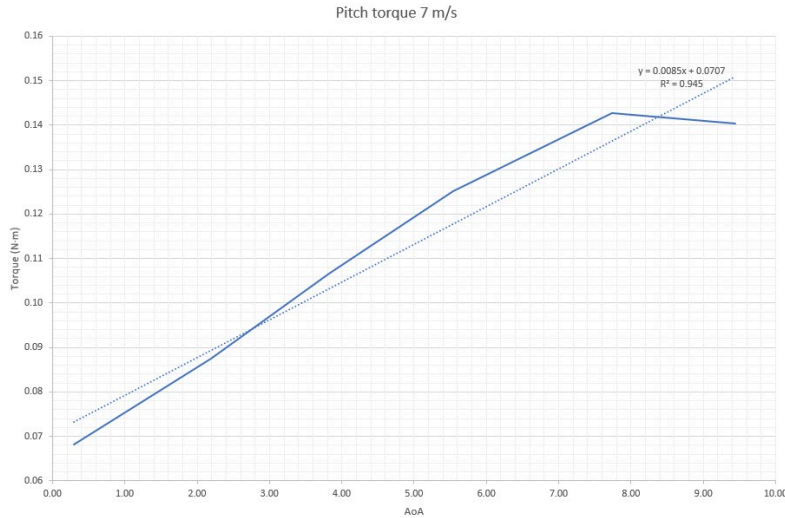


Figure 60:  $M_{ac}$  estimation.

As can be seen in Figure 60, the pitch momentum increases with AoA, this behavior is unstable, however, the prototype is designed and crafted to ensure static stability and that is proven in the dynamic experiments. Thus, these results are not valid, due to the big amount of uncertainties and the complexity of the measure.

## 5.4 Stability derivatives estimation

To model the aircraft in the computer, linearized dynamic equations are used. These equations linearize the dynamic response over a trim condition. The trim corresponds

to a level, symmetric, rectilinear, and stationary flight. Once the system of equations is linearized, the flight variable's time evolution can be calculated when small perturbations affect the flight condition or small control actions are taken. These equations can be seen in detail in chapter 3.3.

One hard task is to linearize aerodynamic forces, it is necessary to know how each force changes due to small changes in flight and control variables:  $(u, w, v, p, q, r)$ ,  $(\delta_e, \delta_a, \delta_r)$  and its derivatives.

Furthermore, the variation of these forces with acceleration perturbations should be included as well. These derivatives are related to the inertia of the air volume being displaced. In general, aircraft inertia is far larger than air inertia so in general, the contribution is small. These derivatives must be calculated with unsteady aerodynamics, so only the most relevant are taken into account. For example, the effect of vertical acceleration ( $\dot{w}$ ) is in general small, but the effect of the sudden changes of vertical velocity affects lift so a short moment later this effect is noticed downstream, in the tail. The phenomenon is called *downwash lag effect* and it is important to evaluate. However, in the case of a tailless plane does not apply. The rest of acceleration derivatives are in general neglected (see [16] and [17]).

Now, moving to control derivatives: these derivatives unlike previous ones are in general difficult to estimate, CFD or real experiments are needed.

As can be seen in these equations, the modeling and estimation of some derivatives are easier than the others. For example, derivatives with respect to  $u$  are not difficult to estimate. The derivatives of alpha ( $Cz_\alpha, Cx_\alpha, Cm_\alpha$ ) are harder because the stream at the tail is affected and the stream is deflected by the wing; this effect is usually modeled with the parameters  $\eta_t$  (tail efficiency) and  $d\epsilon/d\alpha$  (stream deflection) respectively. However, the estimation for tailless planes is easier. The acceleration derivatives with respect to alpha ( $Cz_{\dot{\alpha}}, Cx_{\dot{\alpha}}, Cm_{\dot{\alpha}}$ ) are difficult to calculate, but they are considered to be small in the case of a tailless plane, always depends on many factors as aircraft inertia. If aircraft inertia is small these derivatives with respect to accelerations may be important. The derivatives with respect to  $q$  are harder to calculate, in tail planes these are approximated by the extra lift generated in the tail but in case of a tailless aircraft it is not that easy. Finally, as said before control derivatives are complex to calculate and acceleration control derivatives even more, although they are small (see [16] and [17]).



In conclusion, some of the stability derivatives are well approximated with simple potential aerodynamic formulation while others estimations are not accurate enough, like control derivatives. For this reason, these estimations should be only used for checking: if the aircraft is stable or not, which are the derivatives that may need a large improvement, and the influence of changing aircraft geometry on the stability, among others. If some particular derivatives need to be estimated with higher accuracy it is better to use CFD software or perform flight or wind tunnel tests.

## 5.5 Flight dynamic equations (Control Oriented)

One important aircraft type of control is the stabilization control. The aim is to improve the stability characteristics of the aircraft to ensure easier and safer flight response. In this way, high-frequency modes such as Short Period mode, Roll mode, and Dutch roll must be correctly damped. In general, Roll mode is not oscillatory, there is no need for stabilization control. However, Short Period and Dutch Roll usually need some kind of stabilization control system to increase damping. The Short Period mode uses the Pitch damping system and for Dutch Roll mode, the yaw damping system is used, (see [17]).

Control corrections are fast compared with the modal response of the aircraft, especially compared with Phugoid and spiral mode. In this context, some simplifications in the equations (19), are usually done to simulate in an easier way the aircraft response a short moment after perturbation or control action. (see [17])

For longitudinal movement and short time response  $\Delta u \approx 0$ , so that, equations introduced in chapter 3.3 can be simplified:

$$\begin{aligned} ((2\mu - C_{Z\dot{\alpha}})D - C_{Z\alpha})\Delta\alpha - (2\mu + C_{Z\dot{q}})D\Delta\theta &= C_{Z\delta_e}\Delta\delta_e \\ -(C_{m\dot{\alpha}}D + C_{m\alpha})\Delta\alpha + (\hat{I}_y D^2 - C_{m\dot{q}}D)\Delta\theta &= (C_{m\delta_e}D + C_{m\delta_e})\Delta\delta_e \end{aligned} \quad (19)$$

One can see how the force balance along the X axis is no longer important together with variable  $\Delta u$ . This makes all  $Cx$  stability derivatives and  $Cz_u, Cm_u$  not really important for control design. Actually, the most important derivatives to correctly damp Short Period mode oscillations are those related with Pitch moment ( $Cm_\alpha, Cm_{\dot{\alpha}}, Cm_{\dot{q}}, Cm_{\delta_e}$ ).

For the design of lateral-directional stability control, the equations are also simplified (see 20). In this case, the balance moment equation is neglected, because yaw oscillations are critical and usually need extra damping.

$$\begin{aligned} (2\mu D - C_{Y\beta})\Delta\beta + (2\mu - C_{Y\hat{r}})\Delta\hat{r} &= 0 \\ -C_{n\beta}\Delta\beta + (\hat{I}_z D - C_{n\hat{r}})\Delta\hat{r} &= C_{n\delta_r}\Delta\delta_r \end{aligned} \quad (20)$$

The equations show that the main derivatives in this context are  $(C_{Y\beta}, C_{Y\hat{r}}, C_{n\beta}, C_{n\hat{r}}, C_{n\delta_r})$

## 5.6 Stability derivatives estimation - Wind tunnel

Now that the important stability derivatives are known, to estimate them correctly, it is mandatory to perform wind tunnel experiments.

The experiments for derivatives with respect to angular velocities (q, r) are dynamic experiments. An easy way to estimate these derivatives is to only allow the model to rotate along one axis. Measuring the frequency and oscillation damping and the final angle position, three stability derivatives can be calculated in each experiment.

## 5.7 Dynamic experiments description

As commented before,  $(C_{m_\alpha}, C_{m_{\dot{\alpha}}}, C_{m_q}, C_{m_{\delta_e}})$  are the most relevant stability derivatives for longitudinal flight control. The model is fixed only allowing pitch rotation (see figure 61). Firstly, the plane is trimmed, secondly, it is perturbed with elevator impulse input to record pitch angle, angular velocity, and angular acceleration. Subsequently, the same procedure is followed to estimate  $C_{m_{\delta_e}}$ , but now with an elevator step input. It is important to precisely quantify the elevator input introduced in degrees. Finally, from the recorded data the different stability derivatives are estimated.

The experiment measurements are done for 9 and 10 m/s; the experiment is conducted for all relevant longitudinal trim conditions regarding control design.

The dynamic equations are the following.

$$\begin{aligned} \Delta\theta &= \Delta\alpha \\ \hat{I}_y D^2 \Delta\theta - (C_{m\hat{q}} + C_{m\hat{\alpha}}) D \Delta\theta - C_{m\alpha} \Delta\theta &= C_{m\delta_e} \Delta\delta_e \quad (C_{m\dot{\delta}_e} = 0) \end{aligned} \quad (21)$$

The frequency response properties are deducted from 21 and calculates with the equation 22:

$$\begin{aligned} G_{\theta\delta_e} &= \frac{\Delta\theta(s)}{\Delta\delta_e(s)} = \frac{C_{m\delta_e}}{\hat{I}_y} \frac{1}{(s^2 + 2\xi\hat{\omega}_n s + \hat{\omega}_n^2)} & \hat{\omega}_n &= \sqrt{-\frac{C_{m\alpha}}{\hat{I}_y}} \\ K_{\theta\delta_e} &= A_{\theta\delta_e}(\infty) = \lim_{s \rightarrow \infty} s G_{\theta\delta_e} = \frac{C_{m\delta_e}}{\hat{I}_y \hat{\omega}_n^2} = -\frac{C_{m\delta_e}}{C_{m\alpha}} & \xi &= -\frac{C_{m\hat{q}} + C_{m\hat{\alpha}}}{2\sqrt{-C_{m\alpha}\hat{I}_y}} \end{aligned} \quad (22)$$

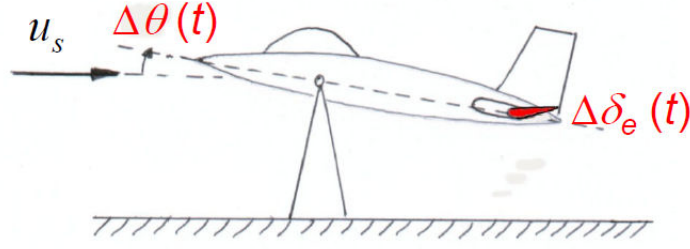


Figure 61: Longitudinal wind tunnel experiment source:[17].

As can be seen  $Cm_{\dot{\delta}_e}$  is neglected. Besides,  $Cm_{\dot{\alpha}}$  and  $Cm_q$  can not be estimated separately and from damping equation. Unlike an aircraft with a tail, for tailless aircraft, it is not trivial to guess beforehand whether  $Cm_{\dot{\alpha}}$  is much bigger than  $Cm_q$  or vice-versa. This experiment has this limitation.

The philosophy of the lateral experiment is similar but Yaw is the single DOF (see figure 62). In absence of rudder control, the yaw perturbation is introduced with the differential drag created by ailerons impulse input.

The simplified dynamic equations are shown in the equation 23.

$$\begin{aligned} \Delta\psi &= -\Delta\beta \\ (\hat{I}_z D^2 - C_{n\hat{r}} D + C_{n\beta}) \Delta\psi &= C_{n\delta_r} \Delta\delta_r \quad (C_{n\dot{\delta}_r} = 0) \end{aligned} \quad (23)$$

The frequency response properties are calculated with the equation 24.

$$\begin{aligned} G_{\psi\delta_r} &= \frac{\Delta\psi(s)}{\Delta\delta_r(s)} = \frac{C_{n\delta_r}}{\hat{I}_z} \frac{1}{(s^2 + 2\xi\hat{\omega}_n s + \hat{\omega}_n^2)} & \hat{\omega}_n &= \sqrt{\frac{C_{n\beta}}{\hat{I}_z}} \\ G_{\hat{r}\delta_r} &= \frac{\Delta\hat{r}(s)}{\Delta\delta_r(s)} = s G_{\psi\delta_r} = \frac{C_{n\delta_r}}{\hat{I}_z} \frac{s}{(s^2 + 2\xi\hat{\omega}_n s + \hat{\omega}_n^2)} & \xi &= -\frac{C_{n\hat{r}}}{2\sqrt{C_{n\beta}\hat{I}_z}} \end{aligned} \quad (24)$$

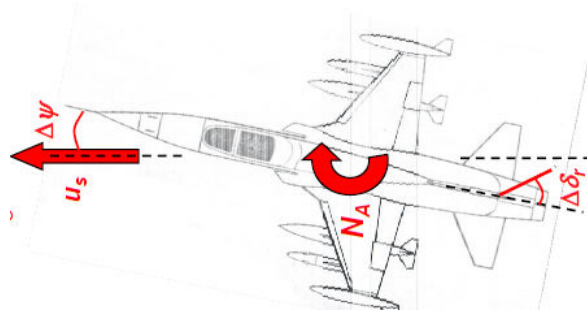


Figure 62: Lateral-directional experiment source:[17].

## 5.8 Dynamic experiments implementation

See annexes A for more information regarding the equipment used for the experiments.

To fix all degree of freedom except the target one, a few plastic parts are designed in *CATIA* (see figure 63 and 3D printed (figure 55). To allow pitch rotation, the model is attached by a shaft mounted through the part's flanges.

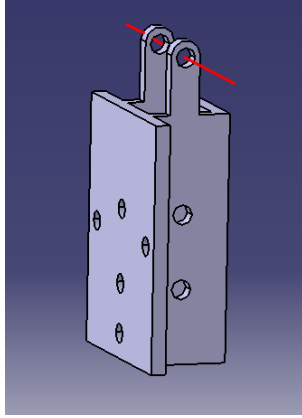


Figure 63: Parts used for the dynamic experiments.



Figure 64: Prototype mounted.

For the second dynamic experiment a bearing (Figure 65) is placed in a manufactured mounting plate that is attached to the model (Figure 66). The bearing rotates together with the mounting plate and the model around an aluminum tube that fits inside the bearing and is also fixed to the load cell.

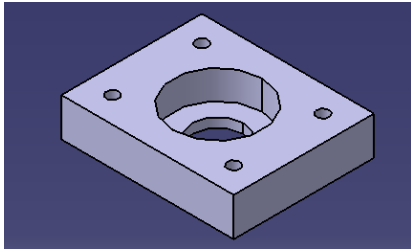


Figure 65: Mounting plate to fit the bearing.



Figure 66: Prototype mounted.

The valuable data is the angular velocity and the angular evolution over time. To record the data, an IMU sensor is attached to the aircraft's belly (figure 67). The data from the IMU is processed by a *RaspberryPi*. There is no direct measure of Euler angles. To solve this issue, a python script is loaded into the *RaspberryPi* to implement a state observer (see chapter 2.4.5) together with an (EKF) Extended Kalman Filter. These two mathematical solutions yield a good estimation of Euler angles.

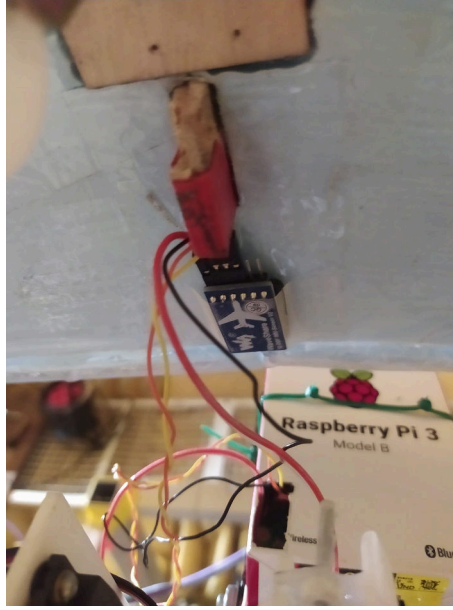


Figure 67: IMU mounted under the prototype.

## 5.9 Dynamic experiment results

### 5.9.1 Lateral experiments

Starting with the lateral experiments, the model is mounted such as only yaw is allowed. During the experiments, the prototype is perturbed and the yaw angle, measured by the IMU, is recorded.

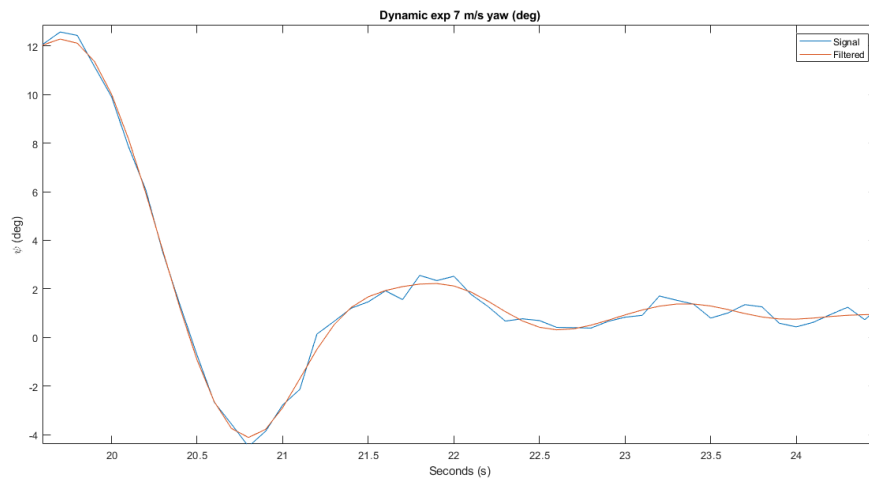


Figure 68: Response to yaw perturbation  $V = 7$  m/s.

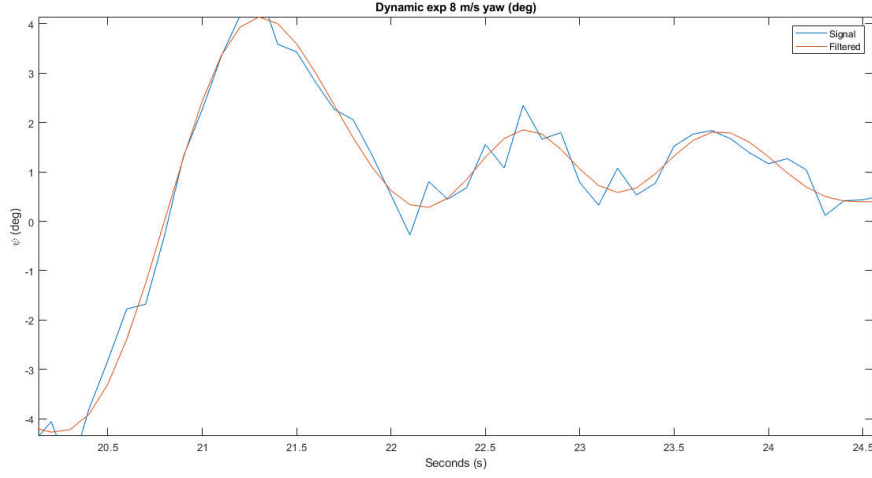


Figure 69: Response to yaw perturbation  $V = 8$  m/s.

One can notice from Figures 68 and 69 that the response is oscillatory and under-damped. These figures are just an example of the different tests performed. The data processed by the EKF contain noise. To remove the noise, and get the real *yaw* angle evolution, a low pass filter is applied to remove noise above 1Hz of bandwidth. Afterward, it is possible to estimate some stability derivatives by measuring the period and amplitude of the oscillations. Applying the following formulas (25 and 26).

$$\begin{aligned}
 f_d &= \frac{1}{T} \\
 \sigma &= \frac{1}{n} \log \frac{x(t)}{x(t+nT)} \\
 \xi &= \frac{1}{\sqrt{1 + \left(\frac{2\pi}{\sigma}\right)^2}} \\
 f_n &= \frac{f_d}{\sqrt{1 - \xi^2}} \\
 \omega_n &= f_n 2\pi
 \end{aligned} \tag{25}$$

Once the natural frequency and damping are obtained, applying the dynamic formulas for a single DOF presented in section 5.7 the stability derivatives are obtained.

$$\begin{aligned}
 \hat{\omega}_n &= \frac{\omega_n b}{2V_a} \\
 \hat{I}_z &= \frac{I_z}{\rho S \left(\frac{b}{2}\right)^3} \\
 \xi &= -\frac{C_{n\dot{r}}}{2\sqrt{\hat{I}_z C_{n\beta}}} \\
 \hat{\omega}_n &= \sqrt{\frac{C_{n\beta}}{\hat{I}_z}}
 \end{aligned} \tag{26}$$

Test	$\omega_n$ rad/s	$\xi$	$C_{n\beta}$	$C_{n\hat{r}}$
1	3.35	0.227	0.0211	-0.0646
2	4.59	0.217	0.0398	-0.0554

Table 16: Response analysis to yaw perturbations  $V = 7m/s$ .

Test	$\omega_n$ rad/s	$\xi$	$C_{n\beta}$	$C_{n\hat{r}}$
1	4.80	0.238	0.0357	-0.0575
2	4.59	0.210	0.0304	-0.0469
3	4.99	0.246	0.0358	-0.0595

Table 17: Response analysis to yaw perturbations  $V = 8m/s$ .

Test	$\omega_n$ rad/s	$\xi$	$C_{n\beta}$	$C_{n\beta}$ XFLR5	$C_{n\hat{r}}$	$C_{n\hat{r}}$ XFLR5
1	4.91	0.176	0.0275	0.0234	-0.0373	-0.01140
2	4.82	0.264	0.0265	0.0234	-0.0550	-0.01140

Table 18: Response analysis to yaw perturbations  $V = 9m/s$ .

As *XFLR5*'s stability derivatives are calculated in the trim condition, at an airspeed of 9 m/s, the comparison is done with the data recorded in experiments at the same velocity. Firstly, looking at both results, and equations, it seems that at a higher airspeed,  $C_{n\beta}$  tends to decrease because it is dependent on the adimensional natural frequency, while the tendency of  $C_{n\hat{r}}$  is not that clear.

In general, the estimations of the stability derivatives are in the same order of magnitude as the *XFLR5* approximation. In particular,  $C_{n\beta}$  is close in both test, however, the experiment suggests a value of  $C_{n\hat{r}}$  three to four times higher than *XFLR5* predictions. This makes sense, as discussed before since angular velocity derivatives are harder to predict.

Nevertheless, *XFLR5* predictions are good and perfectly useful to perform controller design in Simulink.

### 5.9.2 Longitudinal experiments

The longitudinal experiments prove that the model is static stable, i.e the neutral point is located behind the center of gravity. When airspeed raises, the prototype reaches an AoA of equilibrium. The model is tested in 3 different trim conditions (see table 19) moving

the elevators as far as the remote controller trim and actuators let. From this data, it is possible to estimate  $C_{m\delta_e}$ , but only if  $C_{m\alpha}$  is known.

Elevator position	AoA equilibrium (degrees)
down	-1
neutral	7
up	10

Table 19: Trim conditions.

The longitudinal experiment results are not easy to analyze, against all expectations the dynamic behavior is exponential, and no oscillations are observed. When, looking at the equations this exponential response is probably due to the effect of  $C_{m\dot{\alpha}}$  which influence can be important because the prototype inertia is in the same order of magnitude as the surrounding air inertia. It seems that the short period mode is highly damped so is difficult to identify oscillations in the noisy measures. In addition, if  $C_{m\dot{\alpha}}$  is not negligible, the experiment is not useful because one single DOF can not provide all the information to estimate the derivatives see equation 21.

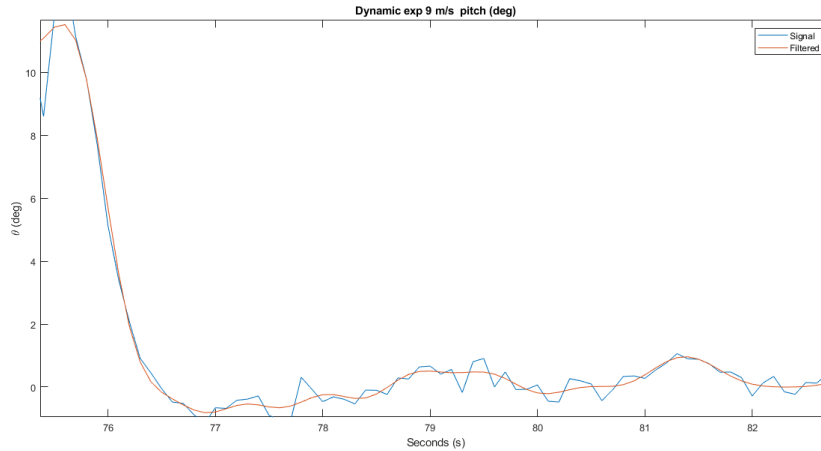


Figure 70: Exponential behavior in pitch angle.

In figure 70 there is no oscillation after the perturbation, the small waves after the perturbations are the effects of noise and vibrations.

## 5.10 Additional data

The FW model is analyzed in *XFLR5* software,  $C_L$ ,  $C_D$ , and  $C_m$  plots are obtained for different velocities and elevator positions. The main outputs of the study are:



- The trimming is complicated and highly depends on COG position.
- The range of possible trim conditions is narrow, there is only one speed of steady flight for each elevator trim position. Below 5 deg down of elevator trim is not possible since no positive lift is achieved.
- Trimming is only possible with neutral and slightly down elevator positions, elevator up trim positions are risky and seem to cause stalls due to a high equilibrium AoA.
- Unlike conventional aircraft, FW elevator inputs greatly affect total lift.

The most relevant conditions to perform the static test are velocities between 6 to 10 m/s with 0 degrees elevator trim.

It is also important not to overload the test cell, especially torque. To avoid this, using *XFRL5*, the order of magnitude of aerodynamic forces and moments is obtained. Also, the maximum load factor ( $n_{max}$ ) is set at 2.5 to avoid damage to the model. Regarding these two structural limits, the limitations are presented in table 20 according to the test cell limits (table 21).

Experiment	limit $n_{max}$	limit test cell
6 m/s, elev 0 (degrees)	-	-
8 m/s, elev 0 (degrees)	-	-
10 m/s, elev 0 (degrees)	9 (degrees) AoA	-

Table 20: Trim flight experiment envelope.

Limit	Quantity
$F_z$	39.2 N
$F_y$	49 N
$M$	2 Nm

Table 21: Test cell limits.

## 5.11 Conclusions, improvement and future work

The experiment results are partially successful. The outcomes help to do a basic aerodynamic characterization of the model but are not enough to develop a full model to simulate the prototype in *SIMULINK*. Thus, for the next sections of this work, the

*XFLR5*'s predictions are used, since experimental data suggest that *XFLR5*'s estimations are correct.

Nevertheless, it is remarkable how it is possible to obtain the most relevant dynamic properties of small UAVs with low-cost experiments. By improving the test cell design and data acquisition equipment it is possible to obtain better results in order to perform safe and accurate dynamic characterization.

Finally, to close the section, a few aspects should be considered in future work.

1. Changing the AoA in the same experiment using a servo allows to do experiments very fast but increases complexity. First, it is not easy to accurately know the AoA that the model reaches when commanding the servo. The origin depends on how IMU is tared. Moreover, when adjusting the servo to change the angle of attack, the IMU introduces noise so measures vary continuously so the elected AoA is inside a range of  $\pm 1^\circ$ .
2. The election of the servo must be done carefully to be able to hold the plane at each velocity. Because of servo limitation, the limit speed is 10 m/s. The servo may limit the experiment's capabilities.
3. The servo introduces vibrations that greatly affect the measures.
4. The coupling between the prototype and test cell must be redesigned in order to be more rigid so the issue of test cell vibrations may be solved.
5. The IMU and force measures were taken by different software because the test cell, which is a commercial product, has its own software. This situation leads to timing problems, making difficult the synchronization of data, and increasing the time spent during post-processing.

The proposed solutions to improve future wind tunnel experiments are the following:

1. Remove the servo and replace the pitch change system with a fixed one, increasing accuracy and reducing vibrations. Instead of changing AoA during the experiment, change velocity.
2. When designing and crafting the prototype carefully design a robust coupling device.
3. Centralize the data recording in one software/script.

## 6 Simulink model

### 6.1 Simulink model description

In the previous chapter, the dynamic equations are simplified to a perturbation linear model. However, that model is only valid for small perturbations in flight conditions. To simulate a wide range of flight conditions and test the designed controllers, a slightly more complex model is needed.

The Simulink model accurately simulates the UAV dynamics since it is a non-linear model. Check the nomenclature section at the beginning of the document for clarity. All the equations in this chapter can be found in [16]. However, the symbol ( $\hat{\cdot}$ ) is used to denote the adimensional variables, being consistent with the nomenclatures used in chapter 3.3.

$$\begin{pmatrix} f_x \\ f_y \\ f_z \end{pmatrix} = \begin{pmatrix} -mg \sin(\theta) \\ mg \cos(\theta) \sin(\phi) \\ mg \cos(\theta) \cos(\phi) \end{pmatrix} + \frac{1}{2} \rho V_a^2 S \begin{pmatrix} C_X(\alpha) + C_{X\dot{q}}(\alpha) \frac{c}{2V_a} q + C_{X\delta_e}(\alpha) \delta_e \\ C_{Y0} + C_{Y\beta} \beta + C_{Y\dot{p}} \frac{b}{2V_a} p + C_{Y\dot{r}} \frac{b}{2V_a} r + C_{Y\delta_a} \delta_a + C_{Y\delta_r} \delta_r \\ C_Z(\alpha) + C_{Z\dot{q}}(\alpha) \frac{c}{2V_a} q + C_{Z\delta_e} \delta_e \end{pmatrix} + \frac{1}{2} \rho S_{prop} C_{prop} \begin{pmatrix} (k_{motor} \delta_t)^2 - V_a^2 \\ 0 \\ 0 \end{pmatrix} \quad (27)$$

Equation 27 and 28 shows the aero-propulsive forces and moments including gravity. The model is quasi-linear, the stability derivatives obtained from *XFLR5* are constant, and they only depend on the trim condition. However, there are non-linear terms such as  $C_D$ , which is quadratic on  $\alpha$ , or thrust which is quadratic on  $\delta_t$ . The force dependency on  $\dot{\alpha}, \dot{q}, \dot{\delta}_e, \dot{\delta}_a, \dot{\delta}_r$  is not included. In addition, forces are decoupled in longitudinal and lateral modes as well as in 3.3.

$$\begin{pmatrix} l \\ m \\ n \end{pmatrix} = \frac{1}{2} \rho V_a^2 S \begin{pmatrix} b[C_{l0} + C_{l\beta} \beta + C_{l\dot{p}} \frac{b}{2V_a} p + C_{l\dot{r}} \frac{b}{2V_a} r + C_{l\delta_a} \delta_a + C_{l\delta_r} \delta_r] \\ c[C_{m0} + C_{m\alpha} \alpha + C_{m\dot{q}} \frac{c}{2V_a} q + C_{m\delta_e} \delta_e] \\ b[C_{n0} + C_{n\beta} \beta + C_{n\dot{p}} \frac{b}{2V_a} p + C_{n\dot{r}} \frac{b}{2V_a} r + C_{n\delta_a} \delta_a + C_{n\delta_r} \delta_r] \end{pmatrix} + \begin{pmatrix} -k_{Tp} (k_{\Omega} \delta_t)^2 \\ 0 \\ 0 \end{pmatrix} \quad (28)$$

All the stability derivatives are calculated in the stability axis, so they must be projected

to the main body axis as follows, (29):

$$\begin{aligned}
C_X(\alpha) &= -C_D(\alpha)\cos(\alpha) + C_L(\alpha)\sin(\alpha) \\
C_{X\hat{q}}(\alpha) &= -C_{D\hat{q}}\cos(\alpha) + C_{L\hat{q}}\sin(\alpha) \\
C_{X\delta_e}(\alpha) &= -C_{D\delta_e}\cos(\alpha) + C_{L\delta_e}\sin(\alpha) \\
C_{Z\hat{q}}(\alpha) &= -C_{D\hat{q}}(\alpha)\sin(\alpha) - C_{L\hat{q}}(\alpha)\cos(\alpha) \\
C_{Z\delta_e}(\alpha) &= -C_{D\delta_e}\sin(\alpha) - C_{L\delta_e}\cos(\alpha)
\end{aligned} \tag{29}$$

The propulsive model, described in the equation 30, is based on Bernoulli's principle. Downstream pressure is calculated with Bernoulli's equation which is only true for a perfect efficient propeller. Then, thrust is calculated with the pressure difference and propeller swept area ( $S_{prop}$ ). (see [16])

$$\begin{aligned}
F_{x_p} &= S_{prop}C_{prop}(P_{downstream} - P_{upstream}) = \\
&\quad \frac{1}{2}\rho S_{prop}C_{prop}(V_{exit}^2 - V_a^2)
\end{aligned} \tag{30}$$

It is known from experimental data, that the exit velocity response to throttle input is linear for the current UAV brush-less engines (see [16]). Thus, thrust is quadratic with throttle command.

$$V_{exit} = k_{motor}\delta_t \tag{31}$$

Due to Newton's third principle, a torque is created in the opposite propeller spin direction. This torque can be modeled as follows:

$$T_p = -k_{T_p}(k_{\Omega}\delta_t)^2 \tag{32}$$

This propulsion model is quadratic with throttle command. It has also two parameters ( $k_{motor}, k_{T_p}$ ) that must be obtained from experimental data. To see the values used in the model check table 33.

The force model implemented in Simulink has been explained. Subsequently, this force model interacts with the dynamic and kinematics blocks. The equations implemented in these blocks can be found in chapter 3.3, previous to the linearization.

Finally, a turbulence wind model, equation 33, based on the Dryden transfer functions, is implemented (see [16]). White noise is passed through the Dryden transfer functions to get the instantaneous wind velocity vector.

$$\begin{aligned}
H_u(s) &= \sigma_u \sqrt{\frac{2V_a}{L_u}} \frac{1}{s + \frac{V_a}{L_u}} \\
H_v(s) &= \sigma_v \sqrt{\frac{3V_a}{L_v}} \frac{(s + \frac{V_a}{\sqrt{3}L_v})}{(s + \frac{V_a}{L_v})^2} \\
H_w(s) &= \sigma_w \sqrt{\frac{3V_a}{L_w}} \frac{(s + \frac{V_a}{\sqrt{3}L_w})}{(s + \frac{V_a}{L_w})^2}
\end{aligned} \tag{33}$$

The Simulink block architecture (see figure 71) is composed of three interconnected block functions. One block computes all external forces and moments, based on the instantaneous states, wind data, elevator, aileron, rudder (if applicable), and throttle commands. Another block computes the wind velocity depending on altitude and airspeed. Finally, the dynamics block is provided with force, moment, and wind data to compute the state's derivative vector, and finally the state vector (equation 34) is integrated in time using the standard *SIMULINK* explicit integration schemes. +

$$x = \{p_n, p_e, p_d, u, v, w, \phi, \theta, \psi, p, q, r\} \tag{34}$$

1: State vector

$(p_{north}, p_{east}, p_{down})$  is the spacial position in the inertial axis (z pointing down),  $(u, v, w)$  are the inertial velocities components expressed in body axis,  $(\phi, \theta, \psi)$  are the Euler angles and finally  $(p, q, r)$  are the angular velocity components in body axis.

$$\delta = \{\delta_e, \delta_a, \delta_r, \delta_t\} \tag{35}$$

2: Input vector

The delta vector's elements (equation 35) are elevator, aileron, rudder (if applicable) and throttle inputs.

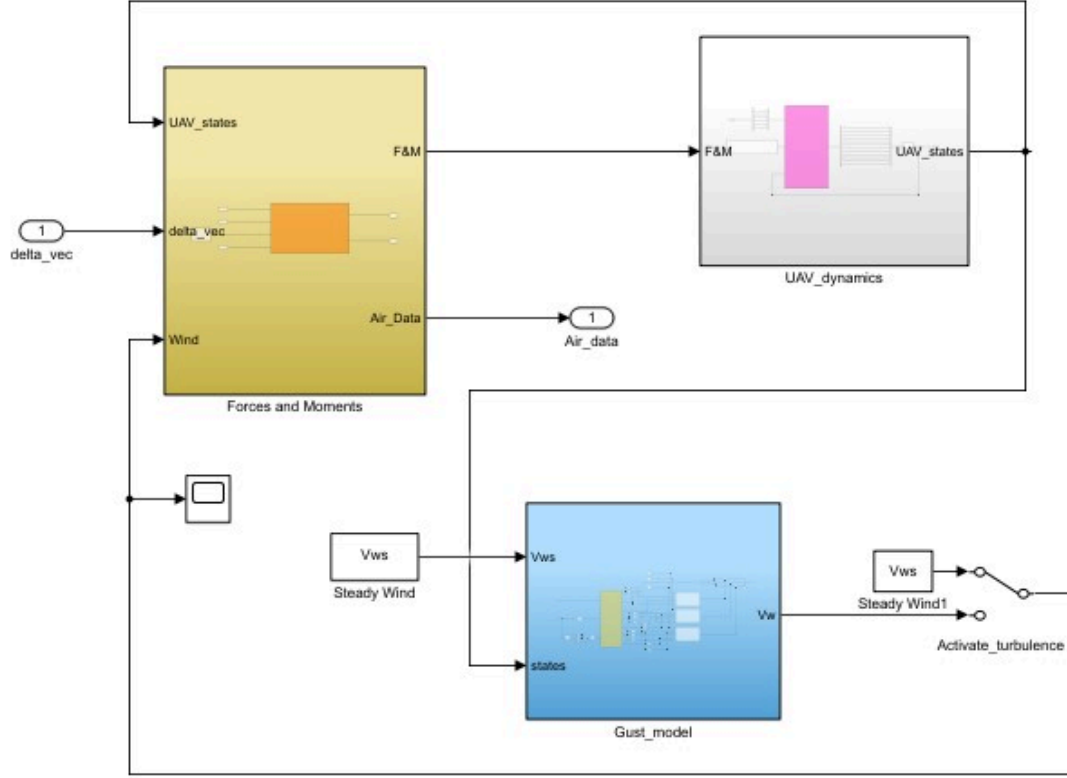


Figure 71: Simulink block structure.

## 6.2 Simulink model linearization and validation

The linearization process starts by reading the stability derivatives from a file. Once the aero-propulsive properties are set, with Matlab's function *findop* the trim condition is obtained. The trim point depends on the constraints given to the function. Finally, the Simulink model is linearized for a particular trim condition using the function *linearize*.

*XFLR5* model does not include propulsion, to validate the *SIMULINK* model with *XFLR5* the propulsive part is deactivated. Thus, constraints must be relaxed because without propulsion it is not possible to hold a constant airspeed while holding altitude.

The trim condition is presented in tables 6.2, 6.2 and 24

States	Constraints	States	Constraints
$p_n$	Unsteady	u	Unsteady
$p_e$	Unsteady	v	Known: 0
$p_d$	Steady	w	Steady
$\phi$	Known: 0	p	Known: 0
$\theta$	Steady	q	Known: 0
$\psi$	Known: 0	r	Known: 0

Table 22: Constraints to states

The trim point is similar to *XFLR5* but airspeed is slightly higher than in *XFLR5*.

Input	Constraints
$\delta_e$	Know: 0
$\delta_a$	Know: 0
$\delta_r$	Know: 0
$\delta_t$	Know: 0

Table 23: Constraints to inputs

Output	XFRL5	SIMULINK
$\alpha$	5.00 <sup>o</sup>	5.00 <sup>o</sup>
$V_a$	9.3	9.99

Table 24: Trim condition

		Mode 1 (Phugoid)	Mode 2 (Short Period)
Eigenvalues	SIMULINK	$\lambda_{1,2}(s^{-1}) = -0.0425 \pm 1.2604i$	$\lambda_{3,4}(s^{-1}) = -17.66 \pm 24.41i$
	<i>XFRL5</i>	$\lambda_{1,2}(s^{-1}) = -0.0318 \pm 1.3375i$	$\lambda_{3,4}(s^{-1}) = -17.32 \pm 22.51i$

Table 25: Comparison of Longitudinal Modes

		Mode 1 (Dutch Roll)	Mode 2 (Spiral)
Eigenvalues	SIMULINK	$\lambda_{1,2}(s^{-1}) = -0.708 \pm 6.10i$	$\lambda_{3,4}(s^{-1}) = 0.153 \pm 0i$
	<i>XFRL5</i>	$\lambda_{1,2}(s^{-1}) = -0.445 \pm 5.73i$	$\lambda_{3,4}(s^{-1}) = 0.0843 \pm 0i$

Table 26: Comparison of Lateral Modes

As can be seen in tables 25 and 26, the eigenvalues obtained by linearizing the *SIMULINK* non-linear model differ from *XFRL5*. The reason is that the aerodynamic model is different. on one hand, *XFRL5* calculates aerodynamics with a potential method (see [14]), and then linearizes the model to get the stability derivatives and modal response. On the other hand, the aerodynamic model built in *SIMULINK* is based on the stability derivatives computed by *XFRL5*, then, a non-linear model is created and finally linearized numerically.

Nevertheless, the difference is small and the *SIMULINK* model is deemed valid to perform the controller design.

## 7 Flight control

In this chapter, a control system is implemented in the Simulink model. The control system is divided into two controllers. The first one is the lateral controller which guides the UAV to a desired course angle. The second one is the longitudinal controller which controls the longitudinal movement, that is to say: altitude and velocity. The controllers designed in the book [16] are used as examples.

The purpose of these two controllers is to change the flight variables to the desired value. However, their task is not to follow a particular path because that is the work of a flight director. The controllers are based on a closed-loop PID hierarchical architecture. Linear design tools are used to design the PID gains. The inner loops are designed using the transfer functions of the linearized system while the outer loops are designed using the outputs of the *SIMULINK* model. The idea is to achieve a fast and slightly under-damped response inner loops and a slower response in outer loops.

The design criteria are based on the linearization of the dynamics, decoupled movements, linear control, etc., but the implemented *SIMULINK* model is non-linear, therefore, these criteria do not apply. For this reason, the whole model must be tested in order to assess the controller's performance.

### 7.1 Lateral autopilot

The architecture of this control loop is based on an inner and outer loops. The inner loop actuates on UAV dynamics, commanding ailerons to achieve the desired bank angle. The outer loop actuates on kinematics guiding the UAV to a determined course commanding the inner loop. As can be seen in figure 72, the implemented control is based on a hierarchical configuration.

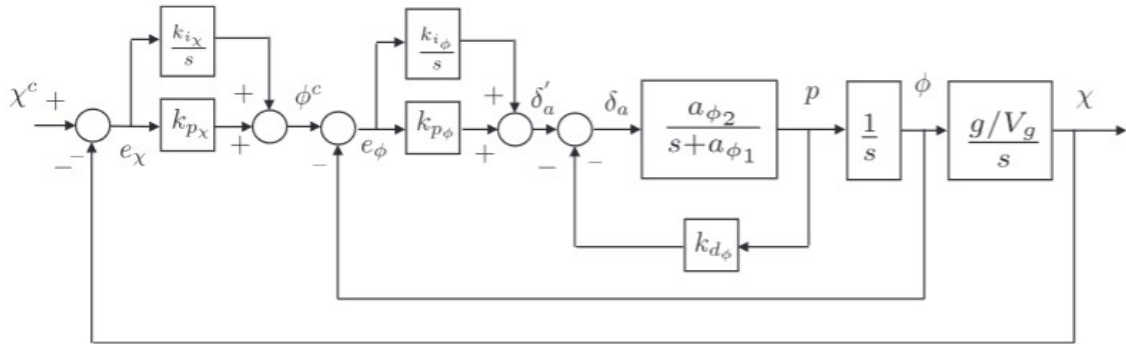


Figure 72: Lateral controller architecture. Source:[16].

The successive loop closure is a design method that simplifies the design of controllers when there is a hierarchical structure. Firstly, the inner loop is designed separately, and



secondly, the outer loop gains are selected. To select the gains of the outer loop, the inner loop transfer function is modeled as a gain of 1. This assumption can be done if the inner loop dynamics are fast enough compared to the outer loop dynamics. Therefore, in the design of the outer loop, this constraint must be taken into account.

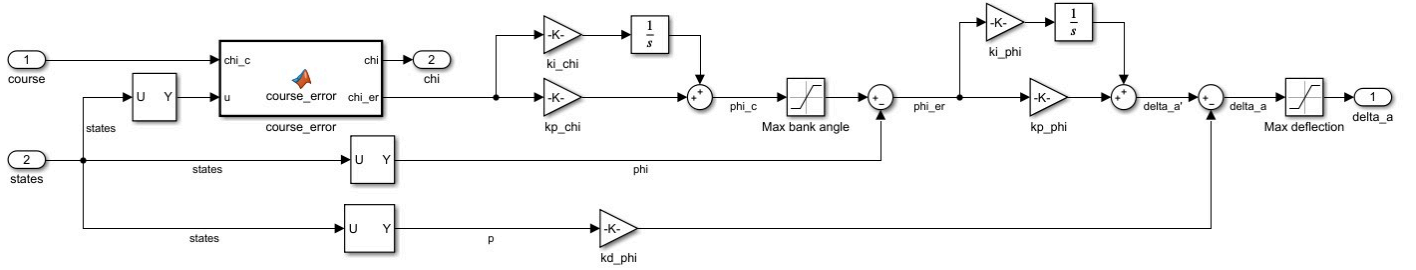


Figure 73: Simulink implementation.

In Figure 73 the lateral controller implementation is presented. Unlike Figure 72, the plant or UAV system does not appear. The UAV dynamics are placed between the output  $\delta_a$  and the input *states*. In Figure 74 the whole architecture can be seen.

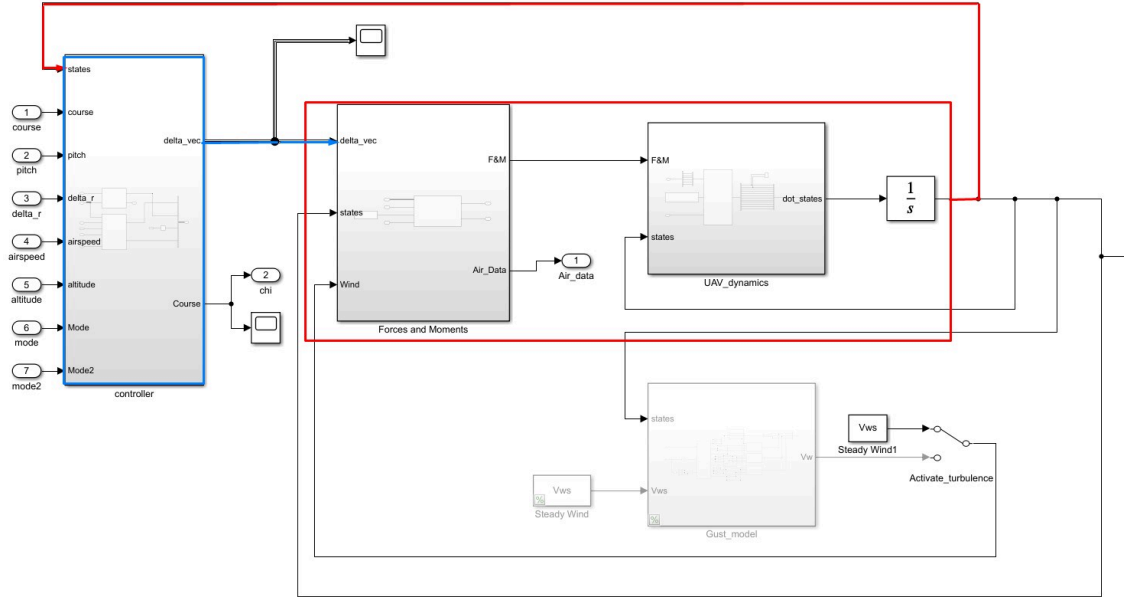


Figure 74: Simulink structure.

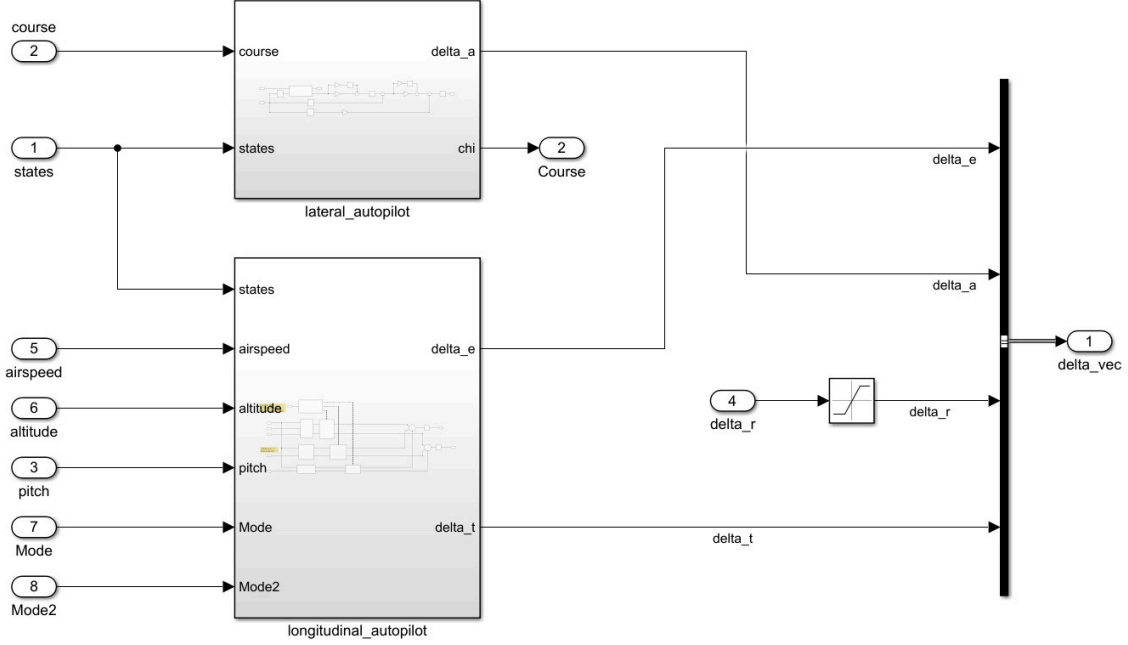


Figure 75: Controller block.

Figure 75 shows the division in two separated controllers that work independently but simultaneously.

### 7.1.1 Inner loop design

Firstly, the *SIMULINK* model is linearized in the operation point. After the lateral dynamics are decoupled from longitudinal ones, the ailerons to bank angle transfer function is obtained.

$$H_{\delta_a-\phi} = \frac{455.3s^2 + 155.6s + 7191}{s^4 + 26.3s^3 + 69.1s^2 + 933.3s + 144.8} \quad (36)$$

The transfer function in the equation 36 has an unstable behavior due to the spiral mode.

After that, closed-loop feedback with PID control is added to the transfer function. The design process is iterative, the three gains ( $kp$ ,  $ki$ , and  $kd$ ) are changed until the step response graph, and frequency response is the desired. The ideal situation is to obtain the fastest response, the less oscillatory one, and with the fastest convergence to zero stationary error.

The UAV's control surfaces have certain physical constraints such as the angular rate of deflection or the maximum deflection. To better simulate the control surfaces, the ac-

tuators should be included, however in this study they are not. In this case, to limit the aileron deflection, a saturation block is included 73. The maximum and minimum angle of deflection is 30 degrees.

One important aspect of the proportional gain ( $k_p$ ) design is to avoid actuator saturation. Saturation means that the maximum actuator's deflection angle is reached but the controller is demanding higher control action. This situation can lead to controller malfunctioning, overloading, and actuator issues.

Provided that the system is stable and the error converges to zero, the maximum error occurs just after the command. Just after the command, the error's derivative and integral parts are both zero, only the proportional part contributes to the error value:

$$\begin{aligned} e_{max} &= y_0 - y_c \\ \delta &= k_p e_{max} \\ (k_p)_{max} &= \frac{\delta_{max}}{e_{max}} \end{aligned} \tag{37}$$

The equation 37 shows the maximum proportional gain value, higher values can cause actuator saturation. The *CP50 – V0* prototype has a maximum aileron deflection angle of 30 degrees, in addition, the expected maximum bank angle error is 15 degrees. Therefore  $(k_p)_{max} = 2$ .

After testing different gain combinations it is observed that:

- $k_p$  increases the response speed but also increases oscillations and overshoot. Values higher than 1 do not increase response speed but considerably increase oscillation and settling time.
- $k_d$  reduces overshoot but increases secondary oscillations.
- $k_i$  removes the stationary error but increases overshoot and oscillations.

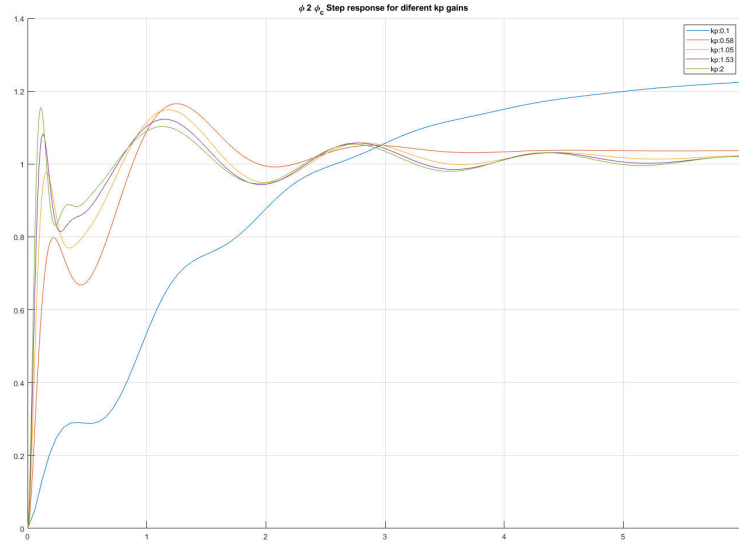


Figure 76:  $\phi$  step response for different  $k_p$  values.

In figure 76, the influence of  $k_p$  is presented. The bigger  $k_p$ , the faster response, however above  $k_p = 0.6$  the influence is smaller. The lower the  $k_p$ , the bigger the static gain of the loop (stationary error). The oscillations raise with  $k_p$ . (The example is without integral control nor derivative control).

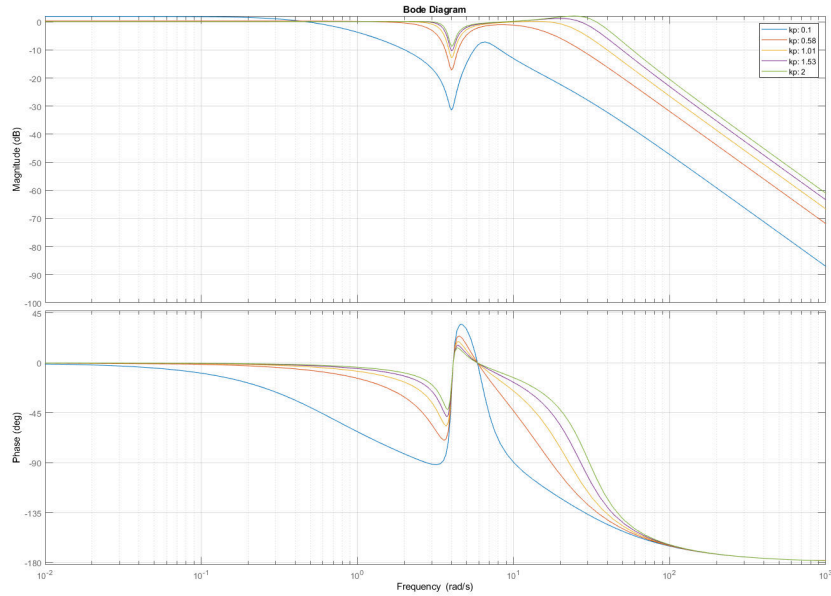


Figure 77:  $\phi$  frequency response for different  $k_p$  values.

It can be seen in the bode diagram that: the lower the  $k_p$  gain, the smaller the bandwidth. As  $k_p$  increases, the point of -10dB moves right, this point defines the bandwidth of the feedback loop. As soon as,  $k_p$  value is over 0.5, the increase in bandwidth is small. The maximum achievable bandwidth is over 4 rad/s . It is also interesting to notice that

the gain for low frequencies is not 0 dB, it is slightly above, generating a stationary error.

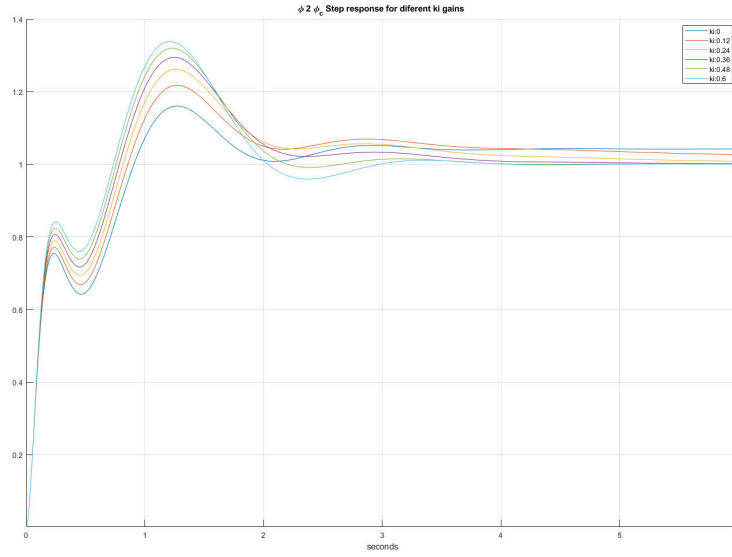


Figure 78:  $\phi$  step response for different  $k_i$  values

Looking at Figure 78, it seems that the gain  $k_i$  removes the stationary error, it also increases the overshoot and even it can turn the system unstable. The amount of  $k_i$  needed depends on how fast the stationary value must be reached and also depends on  $k_p$  gain. Nevertheless, the graph suggests that small values of  $k_i$  are enough to remove the error.

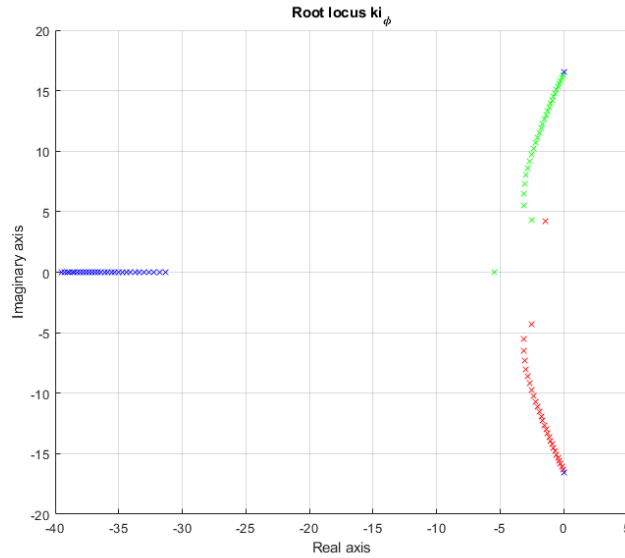


Figure 79: Root locus for various  $k_i$  values ( $k_p = 0.5, k_d = 0.03$ )

High values of the integral gain can lead to instability (see figure 79). In this case, the system roots are plotted for integral gain values from 0 up to 23 resulting in instability of the oscillatory mode.

The selected gains are presented in table 27:

$k_p$	$k_i$	$k_d$
0.5	0.35	0.03

Table 27: Selected gains  $\phi$  loop

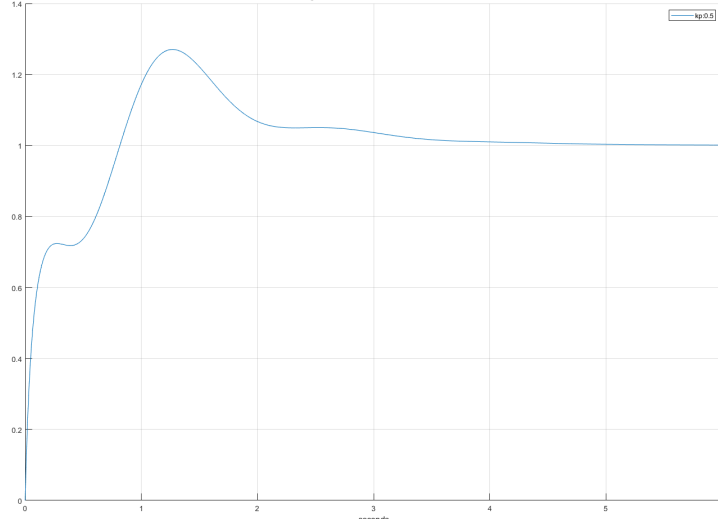


Figure 80: Step response (final gains) (*SIMULINK*)

The final step response (Figure 80), has 27% of overshoot, it has 3.35 seconds of settling time, and 3.6 rad/sec of bandwidth (-3 dB).

### 7.1.2 Outer loop design

Now moving to the design of the outer loop, the two main design requirements are: to meet the bandwidth separation and get a slow response, critically damped or, exponential.

Provided that the inner loop dynamics are fast because the bandwidth constraint is met, the lateral controller loop can be simplified (figure 81). Typically, the inner loop bandwidth should be 10 times higher.

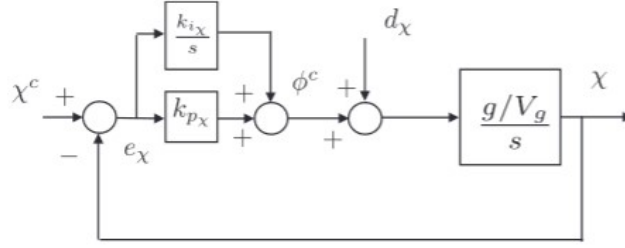


Figure 81: Outer loop simplification Source:[16].

The inner loop is modeled as a unity gain. The outer loop only needs proportional and integral control. Derivative control is not mandatory because the response is slow and robust. The design must ensure bandwidth separation and proper damping.

$$\begin{aligned}\omega_{n_\chi}^2 &= g/V_g k_{i_\chi} \\ 2\xi\omega_{n_\chi} &= g/V_g k_{p_\chi}\end{aligned}\tag{38}$$

The target frequency is as maximum  $0.36 \text{ rad/s}$ . Applying equation 38, the obtained maximum integrative gain value is 0.13. The wanted damping is close to 1 so the proportional gain value must be close to 0.6.

Now, moving to the outer loop, the *SIMULINK* model is run for different gain configurations. The step used for design is  $35^\circ$  of course angle. The selected gains are shown in table 28.

$k_p$	$k_i$
0.4	0.06

Table 28: Selected gains  $\chi$  loop.

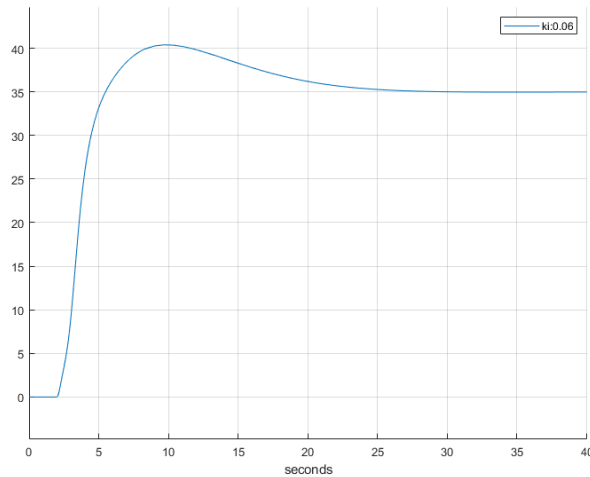


Figure 82: Step response (final gains) (*SIMULINK*).

The final response (Figure 82) has 14% of overshoot, and 22.1 seconds of settling time.

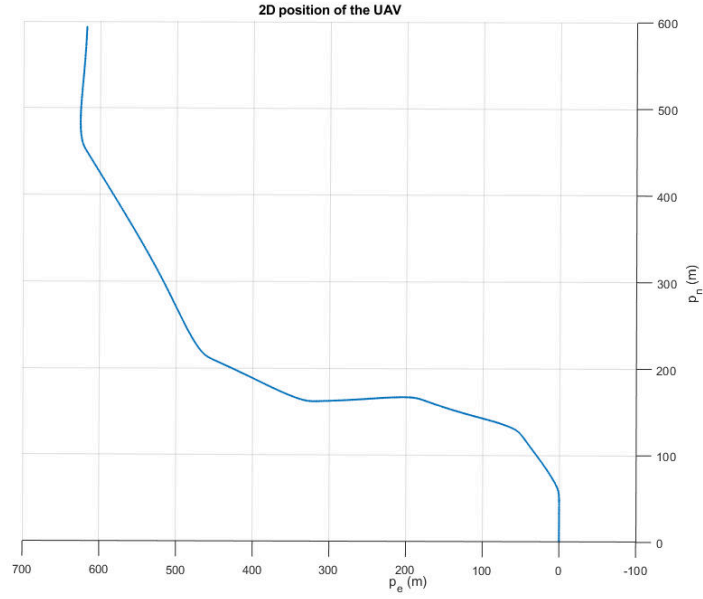


Figure 83: 2D position of the UAV during course change maneuvers.

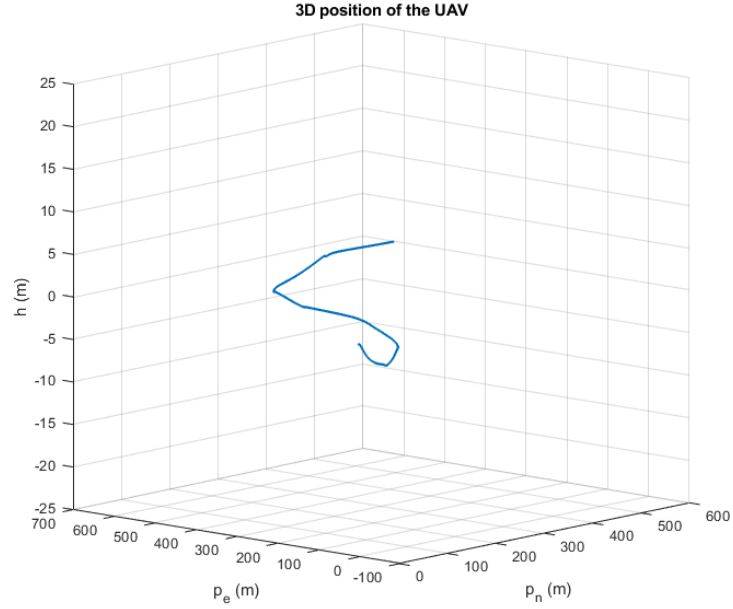


Figure 84: 3D position of the UAV during course change maneuvers.

in figure 83, successive course indications are concatenated in the same simulation, the model follows the indicated course successfully. In this test, the altitude hold autopilot works as well, trying to hold 0 altitude after each turn.



## 7.2 Longitudinal autopilot

The longitudinal autopilot has three modes (see figure 85):

1. Altitude hold: Altitude is regulated by pitch and airspeed by throttle.
2. Pitch hold: This mode is used in take-off to hold a certain pitch combined with full throttle.
3. Climb or descend mode: airspeed is hold actuating on pitch and throttle is full or zero respectively.

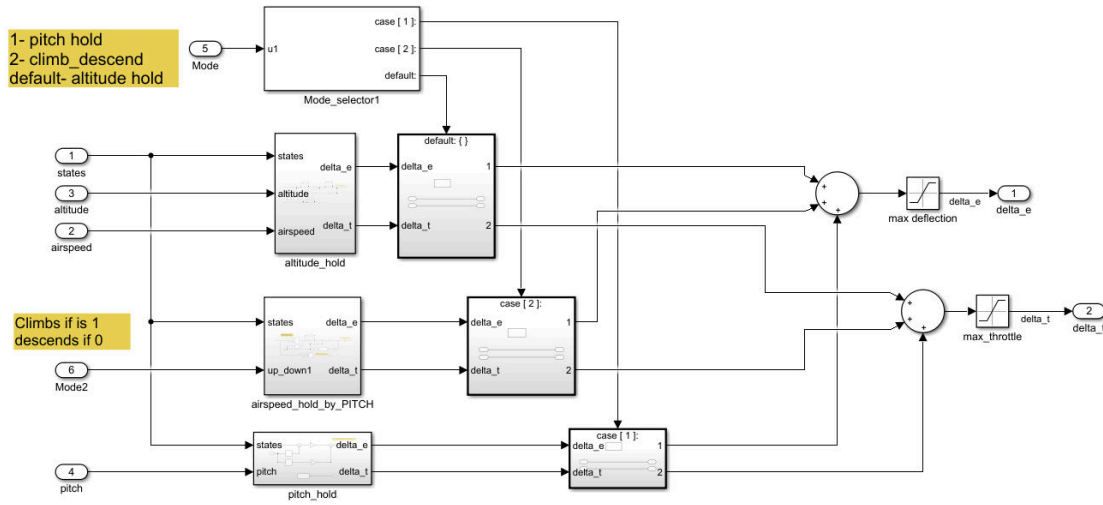


Figure 85: Longitudinal controller's modes.

Only one mode can be operating at the same time, the engaged mode is controlled by a switch and by two signals. Signal *mode* selects between case 1, case 2, and default. The signal *mode2* selects full or zero throttle depending on if the UAV has to climb or descend. Each autopilot's mode has its own closed loop structure but the inner loop that commands pitch is similar in most cases.

The inner loop for pitch control is common to all controller modes. This inner loop has a static gain lower than one, this means that the achieved  $\theta$  does not converge to the desired one. This gain is influenced by  $k_p$  as can be seen in the figure 86. To achieve a gain of 1 it is necessary to introduce integral control.

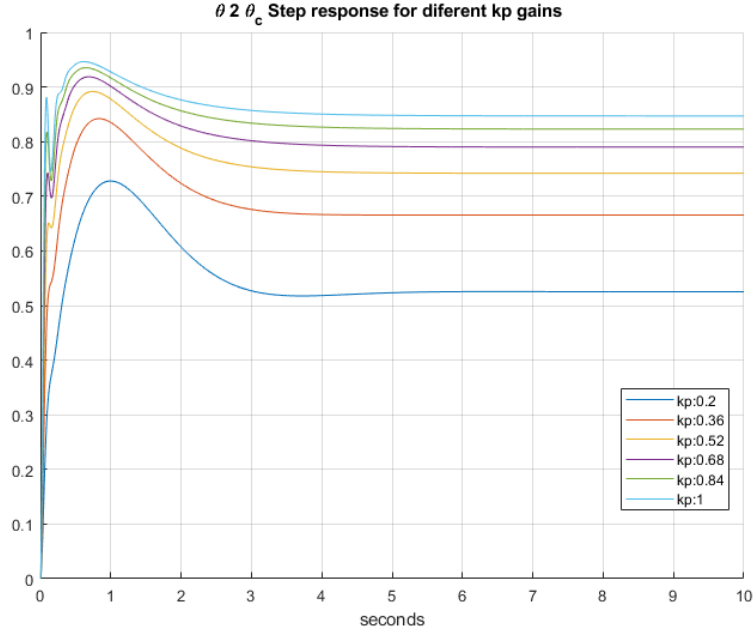


Figure 86:  $k_p$  influence on static gain

Applying equation 37 with the values in table 29:

$e_{max}$	$(\delta_e)_{max}$	$(k_p)_{max}$
$10^\circ$	$35^\circ$	3.5

Table 29: Saturation constraints.

The bode diagram 87 shows the frequency response from low proportional gains to  $(k_p)_{max}$ . The bandwidth increases as the  $k_p$  value raises, as well as the static gain, which approaches 0 dB. Proportional gains over 1 gives a bandwidth of (-3 dB) at 8 rad/s.

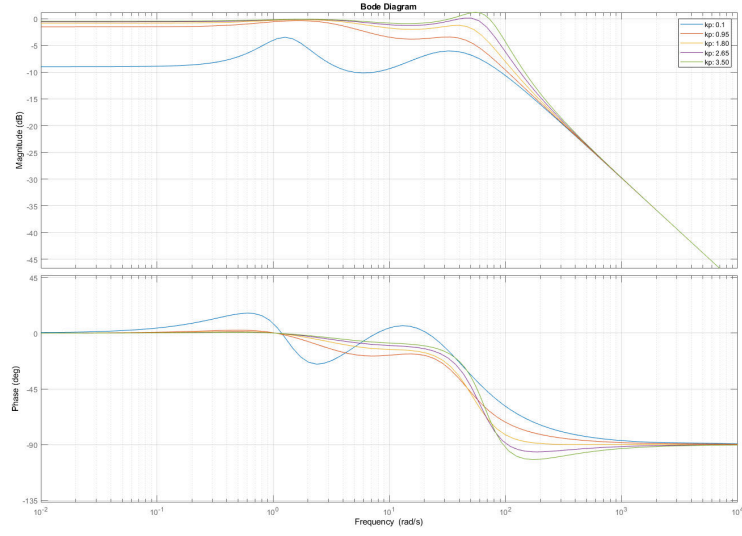


Figure 87:  $K_p$  influence on frequency response.

The influence of  $k_d$  is small, especially for small proportional gains, but mitigates the first oscillation, which might be produced by the short period mode. Figure 88 suggests that small values of derivative control gain can improve the response.

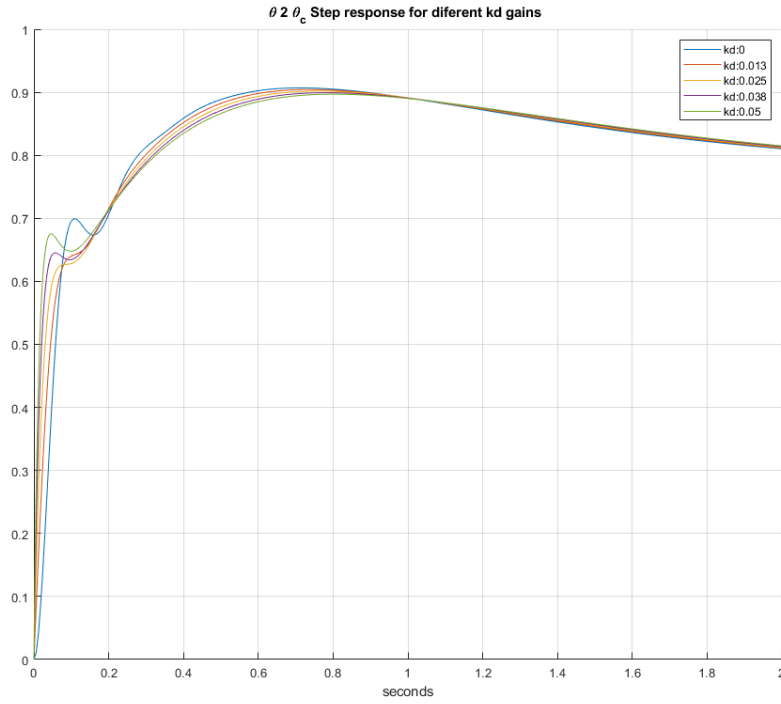


Figure 88:  $k_d$  influence.

In the case of pitch hold mode (see figure 90), is mandatory to introduce integral control to achieve the correct angle. The final design values, in this case, are shown in table 30:

$k_p$	$k_i$	$k_d$
0.8	0.6	0.03

Table 30: Selected gains  $\theta$  loop for pitch hold mode.

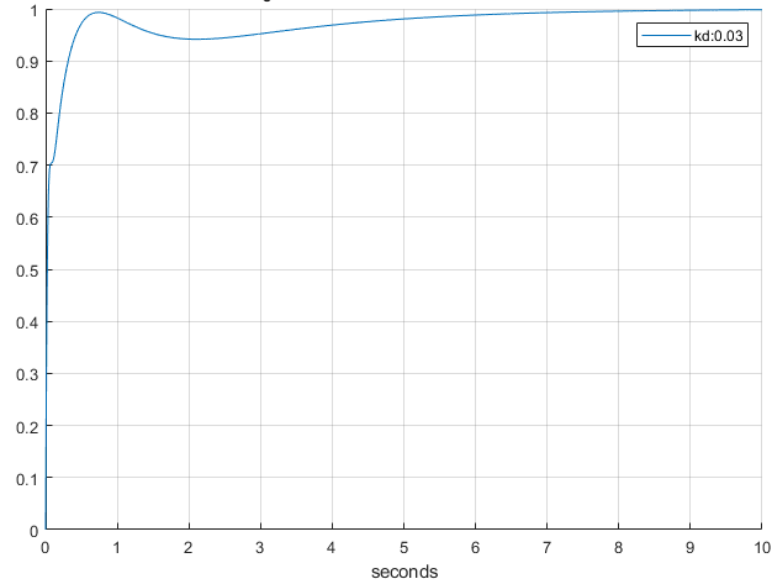


Figure 89: Pitch response with final design gains (*SIMULINK*).

In figure 89, the final response is presented. It is a fast, slightly under-damped response that tends to have stationary error.

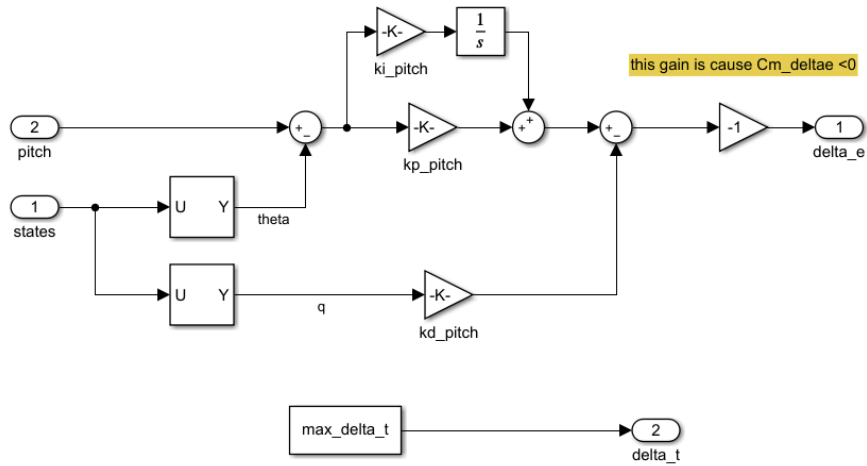


Figure 90: Pitch hold controller *SIMULINK* implementation.

### 7.2.1 Altitude hold controller

In Figure 91, the implemented altitude hold controller is depicted:

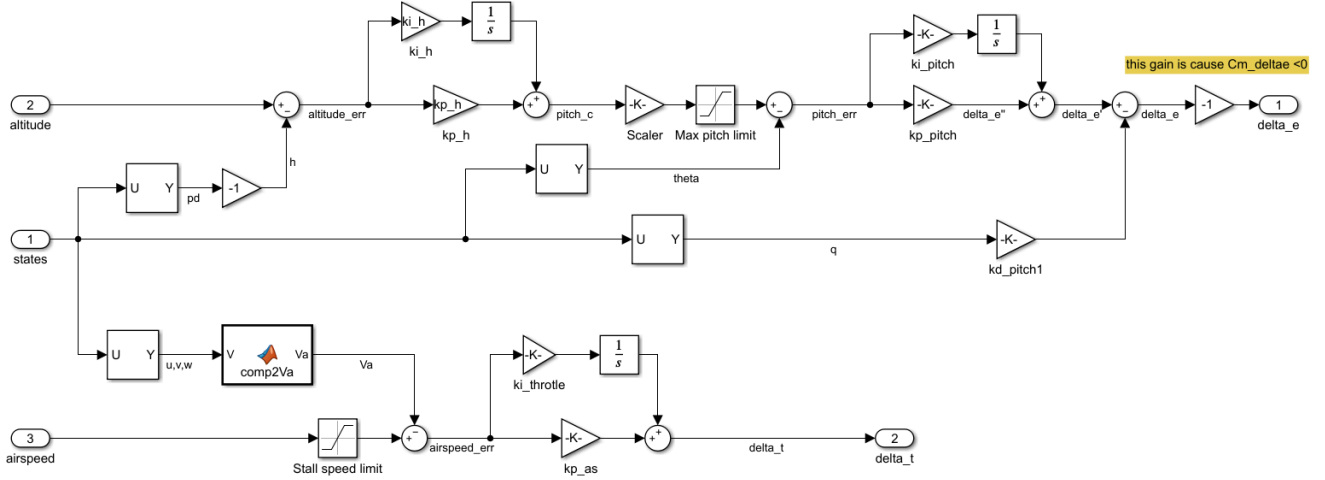


Figure 91: Altitude hold controller *SIMULINK* implementation.

In the diagram 91, the signal  $pitch - c$ , (which is the demanded pitch angle for the inner loop), is multiplied by a  $\frac{1}{10}$  scaler gain because the altitude values are high compared with the pitch angle range in radians. Thus, the values of  $k_{ph}$  and  $k_{ih}$  are in the same order of magnitude as the rest. The pitch angle request must also be in the range  $[-60^\circ, 40^\circ]$  to protect the UAV from entering in stall. It is important to notice that the sign of  $C_{m_{\delta_e}}$  is negative, this means that positive errors in pitch, (that are supposed to be corrected pitching up), will generate positive elevator actions. However, due to the sign of  $C_{m_{\delta_e}}$  these positive elevator actions will cause the UAV to pitch down. To correct this issue, a -1 gain is added at the end.

The inner loop gain design is the same as for pitch hold controller. However, the integrative control is removed so the static inner loop gain is taken into account in the design of the outer loop. Like in the design of the course loop or the altitude loop, the proportional and integrative gains must meet the bandwidth relationship with the inner loop.

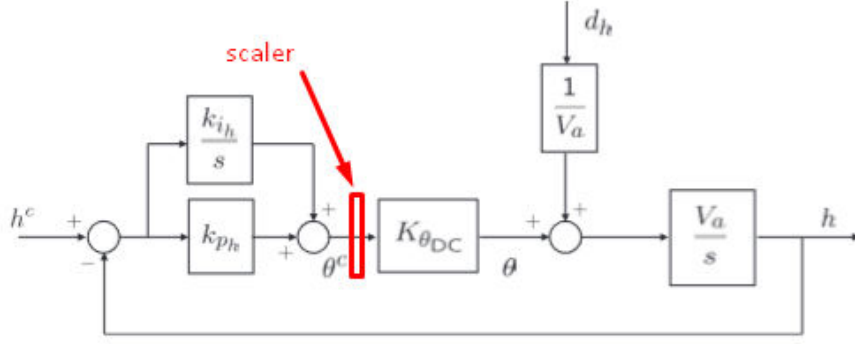


Figure 92: outer loop for altitude control (inner loop dynamics simplified) [16].

Figure 92 is taken from [16], however, in the *SIMULINK* model an extra gain, the scaler, is added so must be included in equation 39.

$$\begin{aligned}\omega_{n_h}^2 &= SK_{\theta_{DC}} V_a k_{i_h} \\ 2\xi\omega_{n_h} &= SK_{\theta_{DC}} V_a k_{p_h}\end{aligned}\tag{39}$$

The inner loop frequency is more or less 8 rad/s. In addition, the target frequency is as maximum 0.8 rad/s. According to the equation 39, the maximum integrative gain value is 0.75.

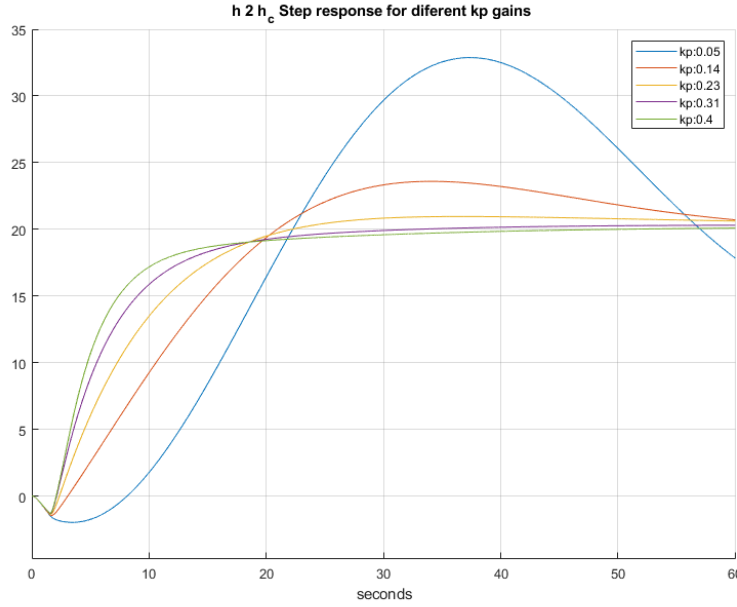


Figure 93: Step response for different  $K_p$  gains.

To select the gains a step of 20 meters of altitude is used. In the figures 93 and 94, the effects of proportional and integral gains for the outer loop are shown. The results

are extracted from simulations instead of from the direct transfer function because the linearization process only calculates the transfer functions of the states with respect to inputs. However, the outer loop's variables are not directly a state so the transfer function must be deducted. As one can observe, the response in altitude is significantly slower compared to pitch dynamics, so bandwidth constraints are widely met.

It can be seen that initially, the UAV descends. This is because the results are obtained from *SIMULINK*, testing the whole model instead of the transfer function-based method. As the UAV pitches up, the airspeed falls, reducing lift, so it takes a bit of time for the airspeed controller to actuate and recover airspeed.

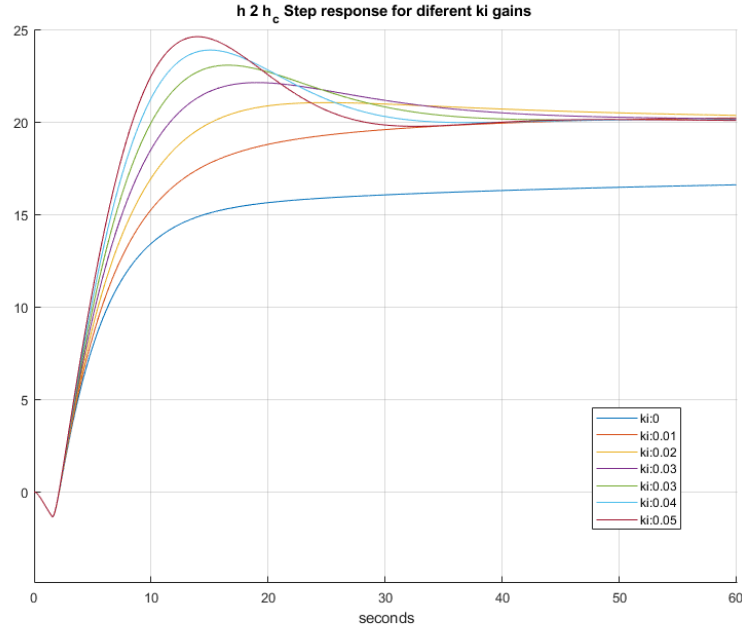


Figure 94: Step response for different  $k_i$  gains.

In the case of following altitude commands, it is preferable to design the controllers to avoid overshooting. The selected gains are presented in table 31.

$k_p$	$k_i$
0.3	0.015

Table 31: Selected gains h loop

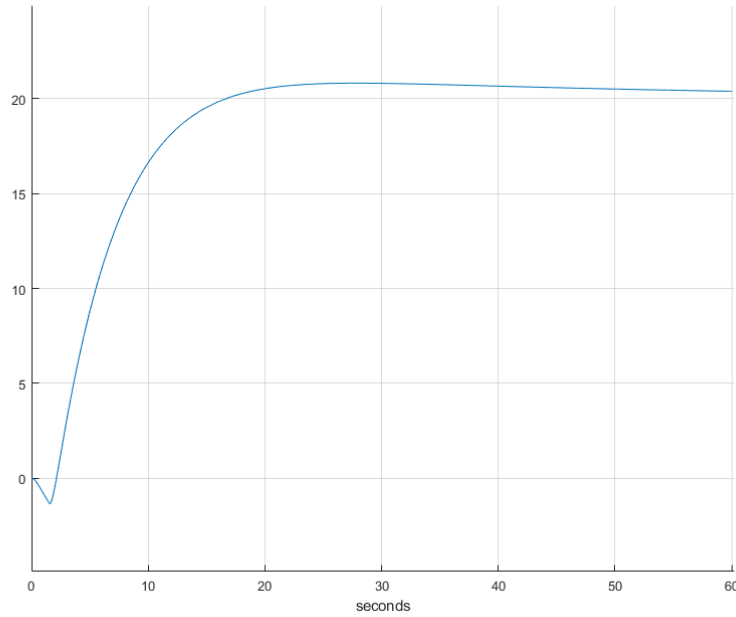


Figure 95: Final step response in altitude.

The selected integral gain value is small, higher values achieve the null stationary error faster, however, they generate a bigger overshoot. The overshoot in the final design (see figure 95) is as low as possible, 3.75%, and the settling time is 59 seconds.

### 7.2.2 Airspeed hold controller

Finally, following an identical procedure, the last longitudinal controller is implemented in *SIMULINK* (see figure 96). This controller holds airspeed by pitch control. The inner loop design is identical. The aim is to design the proportional and integral gains for the outer airspeed loop taking into account the bandwidth limitations.

This mode also combines full or zero throttle depending on whether the action is to descend or to climb. This generates a problem because the *SIMULINK* model is trimmed to particular throttle input, if it changes suddenly, (to zero or to full position), the airspeed is affected. The solution is to perform an airspeed correction but holding the trimmed throttle input, so the airspeed controller has no disturbances.



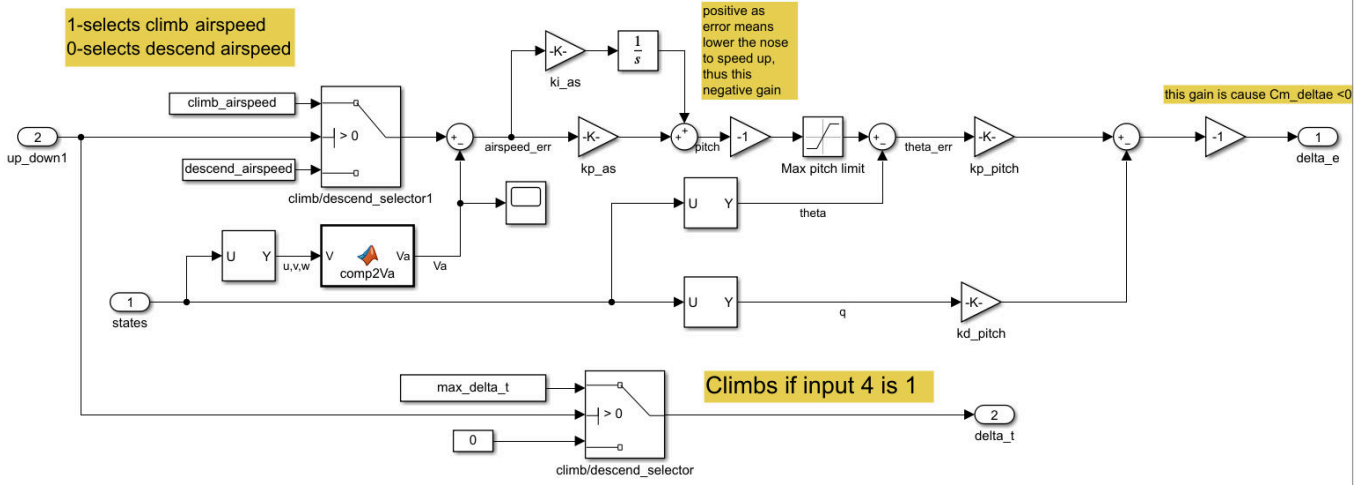


Figure 96: Airspeed hold controller *SIMULINK* implementation.

The selected gains are shown in the table 32:

$k_p$	$k_i$
0.14	0.13

Table 32: Selected gains airspeed loop.

The final response is shown in figures 97 and 98, for a climbing and descending action respectively.

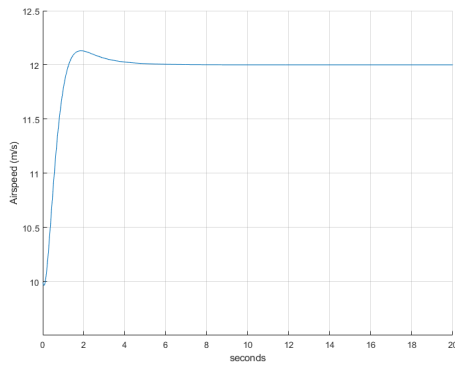


Figure 97: Final step response increasing airspeed

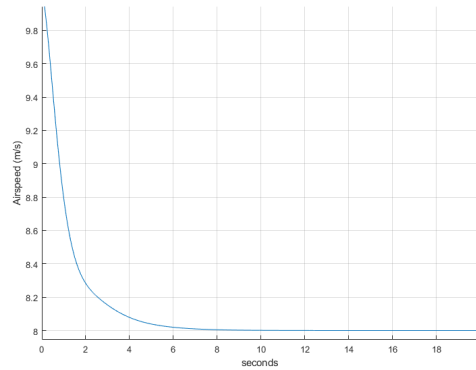


Figure 98: Final step response decreasing airspeed

## 8 Conclusions

This work proves that it is possible to build low-cost UAV prototypes using inexpensive materials. It is also feasible to determine the stability properties of small UAVs by selecting the most relevant dynamic features and designing tailor-made wind tunnel experiments.

The results in chapter 5 suggest that it is feasible to perform low-cost wind tunnel experiments to achieve approximated results. However, the experiment procedures and the wind tunnel stand need to improve, especially the dynamic experiments which are very sensitive to vibrations.

The available open-source simulation software, *XFRL5*, is a good tool to do a first design step in terms of aerodynamics, flight dynamics, and control.

The stability issues of flying wings, described in the chapter 2, can be improved by a combination of a better wing design and control design.

# Appendices

## A Wind tunnel test equipment

The load cell arrangement is a commercial product whose name is *Tyto Robotics Series 1580 Test stand*. The technical details can be found in this link.

*CBenchmark* is an open-source software provided together with the test stand. This app is used for data recording during wind tunnel experiments. The test stand and the data recording application are depicted in figures 99 and 100.



Figure 99: Tyto Robotics Series 1580 Test stand, Source: Tyto Robotics.

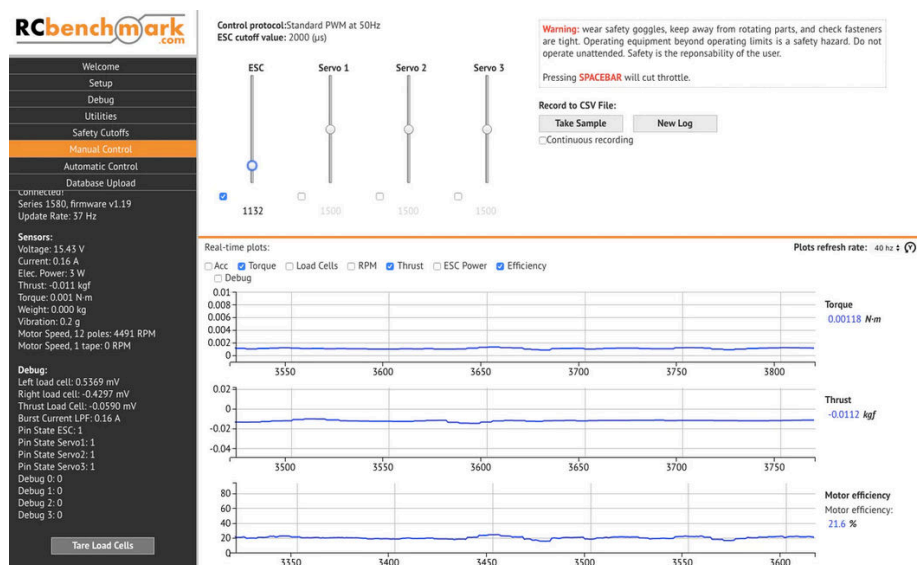


Figure 100: RCbenchmark software Source:Tyto Robotics.

The IMU sensor depicted in figures 101 and 102 is used to collect the inertial data is the 10 DOF IMU by WaveShare. Its main features are:

- MPU9255 chip: 3-axis gyroscope, 3-axis accelerometer, and 3-axis compass/magnetometer
- BMP180: barometric pressure sensor
- Embedded temperature sensor for temperature compensation

To search for further technical information see [link](#).



Figure 101: IMU back face Source:[link](#).

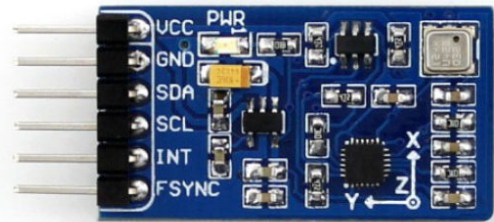


Figure 102: IMU front face Source:[link](#).

With the purpose of processing the raw data from the IMU a *RaspberryPi* device is used. The *RaspberryPi* is connected to the IMU via IC2 port, a detail of the connection is presented in figures 103 and 104.

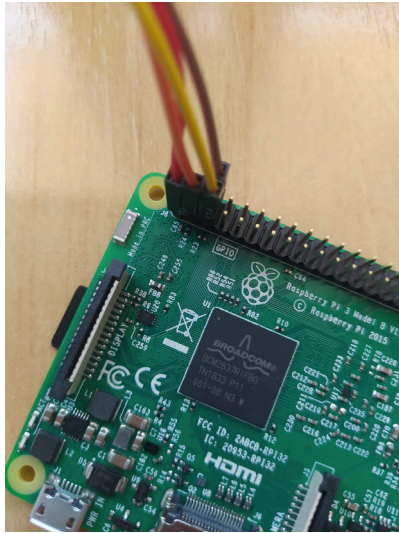


Figure 103: *RaspberryPi* connections IC2 port.

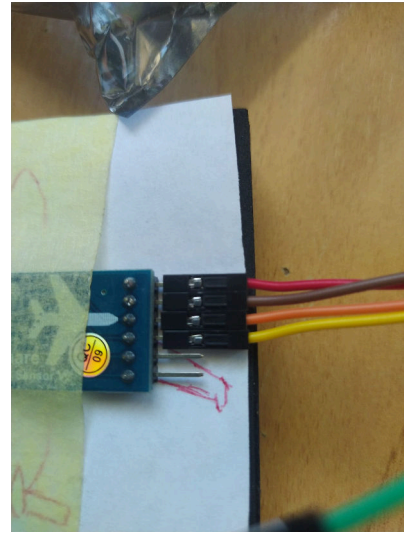


Figure 104: IMU connections.

Multiple *Python* scripts are used to establish communications with the IMU. Besides, other scripts process the raw data from accelerometers and gyroscopes to compute the Euler angles. An Extended Kalman filter is implemented in these scripts to better estimate these variables. The repository with all the files can be found here [link](#).

## B Model parameters

In the first table 33, all the parameters except the stability derivatives are shown. In the second one 34, values regarding the trim condition are detailed. Finally, the stability derivatives are quantified in table 35.

Parameter	Value	Units
$m$	0.388	kg
$\rho$	1.204	kg/m <sup>3</sup>
$g$	9.8	m/s <sup>2</sup>
$\bar{c}$	0.219	m
$b$	0.950	m
$S$	0.202	m <sup>2</sup>
$S_{prop}$	0.0182	m <sup>2</sup>
$C_{prop}$	1	-
$k_{motor}$	20	m/s
$k_{Tp}$	0	Nm/rpm <sup>2</sup>
$k_{\omega}$	0	rpm
$\sigma_u$	1.06	m/s
$\sigma_v$	1.06	m/s
$\sigma_w$	0.7	m/s
$L_u$	200	m
$L_v$	200	m
$L_w$	50	m

Table 33: Model parameter

Due to the lack of time to test the engine, the parameters are taken from [16]. The engine size is similar to the selected one. Nevertheless, the engine properties are not really important in this study because the focus is not to study the endurance or the power consumption. However, the engine affects the stability properties. The values for the Dryden's transfer functions (bottom of table 33) are taken from [16].

Variable	Value	Units
$\theta$	0.0873	rad
$V_a$	9.99	m/s
$\alpha$	0.0873	rad
$\delta_t$	0.559	-

Table 34: *SIMULINK* model trim point

Stability derivative	Value
$C_{L0}$	-0.046
$C_{L\alpha}$	4.099
$C_{D\alpha}$	(see figure 105)
$C_{L\hat{q}}$	5.504
$C_{D\hat{q}}$	0.304
$C_{X\delta_e}$	-0.064
$C_{Y0}$	0
$C_{Y\beta}$	-0.143
$C_{Y\hat{p}}$	-0.074
$C_{Y\hat{r}}$	0.096
$C_{Y\delta_a}$	0.060
$C_{Y\delta_r}$	0
$C_{Z\delta_e}$	-1.939
$C_{l0}$	0
$C_{l\beta}$	-0.114
$C_{l\hat{p}}$	-0.414
$C_{l\hat{r}}$	0.108
$C_{l\delta_a}$	0.349
$C_{l\delta_r}$	0
$C_{m0}$	0.053
$C_{m\alpha}$	-0.609
$C_{m\hat{q}}$	-1.725
$C_{m\delta_e}$	-0.869
$C_{n0}$	0
$C_{n\beta}$	0.023
$C_{n\hat{p}}$	-0.025
$C_{n\hat{r}}$	-0.011
$C_{n\delta_r}$	0
$C_{n\delta_a}$	-0.024

Table 35: Stability derivative values

Figure 105 shows the drag polar obtained in *XFRL5* and the polynomial fitting that is embedded in the *SIMULINK* model to evaluate drag for each AoA.

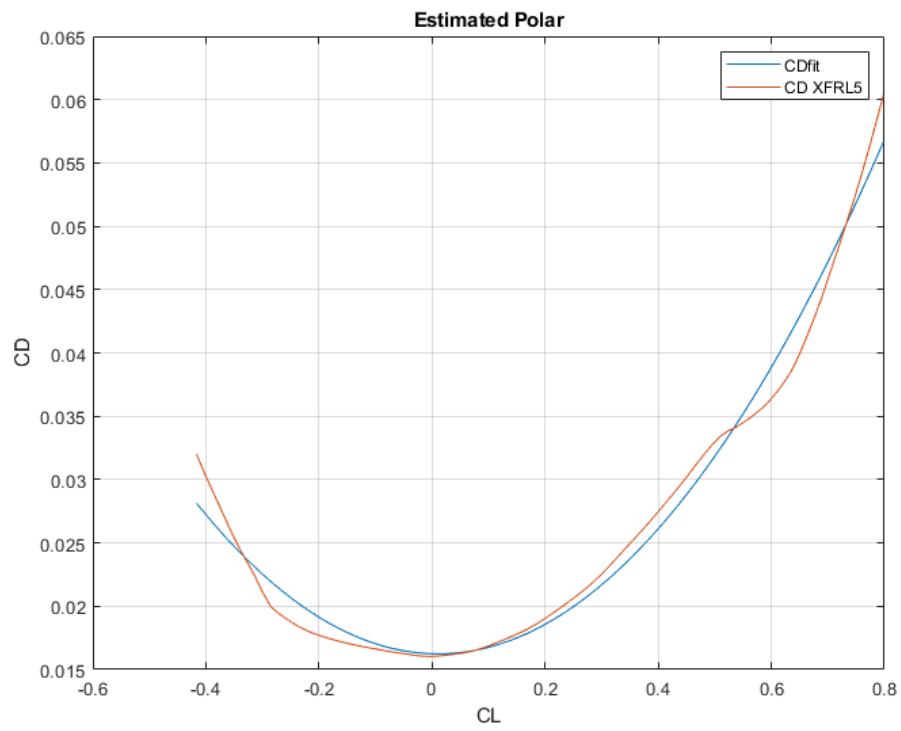


Figure 105: Prototype drag polar

## References

- [1] Alejandro Álvarez Monteagudo. *Design and performance assessment of an adaptable small scale UAV*. Sept. 2022.
- [2] Ralph L Schwader. “The Development of the Flying Wing”. In: *Journal of Aviation/Aerospace Education & Research* 8.1 (1997), p. 4.
- [3] Faliang Wang. *The comparison of aerodynamics and stability characteristics between conventional and blended wing body aircrafts*. 2011/2012.
- [4] Petterson Emil. *Design of a drone system for maritime search and rescue missions*. 2020.
- [5] Martin Hepperle. *Airfoils for Tailless Airplanes: Design and Selection*. [https://www.mh-aerotools.de/airfoils/nf\\_2.htm](https://www.mh-aerotools.de/airfoils/nf_2.htm), (last visit on 06/10/2022). 2018.
- [6] Roberto Merino Martínez. *Design and Analysis of the Control and Stability of a Blended Wing Body Aircraft*. Tech. rep. KTH, 2014.
- [7] Wikipedia. *Flying wing*. [https://en.wikipedia.org/wiki/Flying\\_wing#Directional\\_stability](https://en.wikipedia.org/wiki/Flying_wing#Directional_stability), (last visit on 06/10/2022).
- [8] Rita Cunha/J.R.Azinheira. *Lectures UAVs MEAer*. 2021/2022.
- [9] Andrew Newton. *hot wire cut foam airfoil*. URL: <https://www.youtube.com/watch?v=JIRzQ04F8ck&t=180s>.
- [10] Eduardo Núñez. *ZYKLON 400 : Flying wing prototype*. URL: <http://www.alasvolantes.es/planos/8-alas-con-flecha/18-zyklon-400.html>.
- [11] Oleh Tkachuk. *Detailed design of a forest surveillance UAV*. Tech. rep. Tecnico Lisboa, 2018.
- [12] João Luís Câmara Ornelas. *Scaled UAV Prototyping and Control*. July 2021.
- [13] Der-Ming Ma Pei-Hsiang Chung and Jaw-Kuen Shiau. “Design, Manufacturing, and Flight Testing of an Experimental FlyingWing UAV”. In: *MDPI* (2019), p. 22.
- [14] *XFRL5 documentation*. URL: <http://www.xflr5.tech/xflr5.html>.
- [15] Wikipedia. *Potential flow*. [https://en.wikipedia.org/wiki/Aerodynamic\\_potential\\_flow\\_code](https://en.wikipedia.org/wiki/Aerodynamic_potential_flow_code), (last visit on 06/10/2022).
- [16] Randal W Beard and Timothy W McLain. *Small unmanned aircraft: Theory and practice*. Princeton university press, 2012.
- [17] Miguel Ángel Gómez Tierno, Manuel Pérez Cortés, and César Puentes Márquez. *Mecánica del vuelo*. Ibergaceta, 2012.



- [18] Wikipedia. *Prandtl Lifting-Line Theory*. [https://en.wikipedia.org/wiki/Lifting-line\\_theory](https://en.wikipedia.org/wiki/Lifting-line_theory), (last visit on 06/10/2022).